Tracking dynamics of metallophilic interactions in the excited state using ultrafast structural probes

Dissertation
at the Faculty of Mathematics, Informatics and Natural Sciences
Department of Chemistry
University of Hamburg

Sharmistha Paul Dutta

Hamburg, December 2025

Dissertation

Title:	Tracking dynamics of metallophilic interactions in the excited state using ultrafast structural probes
Eingereicht von:	Sharmistha Paul Dutta
Matrikelnummer:	7573395
E-Mail Adresse:	sharmisthapauldutta@gmail.com
Arbeitsgruppe:	Prof. Dr. Dorota Koziej
Institut:	Institut für Nanostruktur- und Festkörperphysik
Universität:	Universität Hamburg
Datum der Einreichung:	19.12.2025
Erstgutachter:	Prof. Dr. Dorota Koziej
Zweitgutachter:	Prof. Dr. Arwen Pearson
Datum der Disputation:	20.02.2026
Prüfungskommission:	Prof. Dr. Dorota Koziej
	Prof. Dr. Tobias Beck
	Prof. Dr. Arwen Pearson
	Dr. Christopher Milne
	Dr. Benjamin E. Van Kuiken

The present work was carried out in the period from August 2021 to July 2025 at the European XFEL GmbH under the supervision of Dr. Christopher Milne, Dr. Dmitry Khakhulin and Prof. Dr. Dorota Koziej from the Institute for Nanostructure and Solid State Physics at the University of Hamburg.

Date of oral defense: 20.02.2026

Date of print approval: 05.02.2026

Date of submission: 19.12.2025

DEDICATION

This dissertation is dedicated to my loving parents and family.

Contents

List of Tables

List of Figures

Zusammenfassung

Metallophile Wechselwirkungen in abgeschlossenen d^{10}-Metallzentren spielen eine bedeutende Rolle bei der Steuerung der photophysikalischen und photochemischen Eigenschaften ihrer Komplexe. Diese Komplexe haben ein breites Anwendungsspektrum, das von lumineszenten Materialien für energieeffiziente Optoelektronik und Photokatalysatoren für die solare Energiekonversion bis hin zu Sensoren für Umweltüberwachung und Bioimaging reicht. Ein detailliertes Verständnis ihrer photoinduzierten Strukturdynamik ist daher entscheidend für die Weiterentwicklung nachhaltiger Materialgestaltung und die funktionale Optimierung.

Diese Dissertation konzentriert sich auf die Untersuchung metallophiler dinuklearer Komplexe. Dies umfasst die detaillierte Synthese und Charakterisierung von fünf verschiedenen bimetallischen Komplexen. Unter diesen wurden zwei Gold(I)-Dimerkomplexe, $[Au_2(dcpm)_2](PF_6)_2$ und $[Au_2(pnnp)_2]Cl_2$, im Detail untersucht, wobei eine Kombination aus stationärer Extended X-ray Absorption Fine Structure (EXAFS), transienter optischer Absorptionsspektroskopie (TAS) und zeitaufgelöster Weitwinkel-Röntgenstreuung (WAXS) mit optischer Anregung bei 266 nm zum Einsatz kam, um eine direkte Korrelation zwischen elektronischer Anregung, struktureller Reorganisation und Au–Au-Bindungslängenänderungen über Zeitbereiche von Femtosekunden bis Pikosekunden zu ermöglichen. Die Experimente wurden an großskaligen Synchrotron- und XFEL-Einrichtungen durchgeführt, darunter PETRA III (P64), ESRF (ID09) und European XFEL (FXE), unter Nutzung hochbrillanter Röntgenquellen. Die Dissertation beinhaltet den jeweiligen theoretischen Hintergrund sowie den experimentellen Aufbau dieser Methoden. Diese Studien decken das fundamentale Zusammenspiel zwischen metallophilen Wechselwirkungen, Ligandenumgebung und Lösungsmittelreorganisation auf, das die strukturelle Entwicklung im angeregten Zustand bestimmt.

Die ultraschnelle Strukturdynamik des Komplexes $[Au_2(dcpm)_2](PF_6)_2$ zeigt eine Au–Au-Kontraktion von etwa –0,11 Å, wohingegen der Komplex $[Au_2(pnnp)_2]Cl_2$ bei derselben Verzögerungszeit von 100 fs eine größere Kontraktion von etwa –0,52 Å erfährt. Die Analyse der Streudaten in Lösung berücksichtigte sowohl Solut- als auch Lösungsmittelbeiträge, während erste Molekulardynamik-(MD)-Simulationen des Käfigterms eingesetzt wurden, um die experimentellen Ergebnisse zu untermauern.

Abstract

Metallophilic interactions in closed-shell d^{10} metal centers play a significant role in governing the photophysical and photochemical properties of their complexes. These complexes have formed a wide range of applications, ranging from luminescent materials for energy-efficient optoelectronics and photocatalysts for solar energy conversion to sensors for environmental monitoring, and fluorescent markers for microscopy imaging. The relevant photophysical properties are defined by initial processes right after photoexcitation on the way to formation of the long-lived luminescent excited state. Thus, a detailed understanding of their photoinduced structural dynamics is crucial, as these early processes define the relaxation pathways leading to the formation of long-lived emissive or reactive excited states. Elucidating these dynamics provides fundamental insights necessary for the rational design and optimization of metallophilic systems with tailored photophysical performance and enhanced functional stability.

This thesis focuses on the investigation of metallophilic dinuclear complexes. It includes the detailed description of synthesis and characterization of five different bimetallic complexes. Among them, two gold(I) dimer complexes, $[Au_2(dcpm)_2](PF_6)_2$, and $[Au_2(pnnp)_2]Cl_2$, were investigated in detail with the combination of steady-state extended X-ray absorption fine structure (EXAFS), and time-resolved wide-angle X-ray scattering (WAXS) measurements with optical excitation at 266 and 320 nm to enable the structural reorganization and Au-Au bond distance change over time ranges spanning from femtoseconds to picoseconds. Three other metal dimer complexes, $[Au_2(pnnp)Cl_2]$, $[Ag_2(dcpm)_2](PF_6)_2$ and $[Cu_2(dcpm)_2](PF_6)_2$ were studied, but only the preliminary results are included in this thesis.

The experiments were conducted at large-scale synchrotron and XFEL facilities, including PETRA III (P64), ESRF (ID09), and European XFEL (FXE), exploiting high-brilliance X-ray sources. The thesis includes the respective theoretical background and experimental setup for these techniques. These studies address the fundamental interplay between metallophilic interactions, ligand environment, and solvent reorganization driving the excited-state structural evolution.

This thesis will present the experimental results and analysis of the gold(I) dimer complexes in the excited state, having Au-Au bond contraction. The ultrafast structural dynamics of $[Au_2(dcpm)_2](PF_6)_2$ complex exhibits an Au–Au contraction of approximately -0.11 Å whereas $[Au_2(pnnp)_2]Cl_2$ complex undergoes a larger contraction of about -0.52 Å at the same 100 fs delay. Analysis of the solution-phase scattering data incorporated both solute and solvent contributions, while initial classical molecular dynamics (MD) simulations of the solvation shell structure were employed to support the experimental findings.

List of Publications

1. K. Barlow, R. Phelps, J. Eng, R. A Ingle, D. Khakhulin, M. Biednov, **S. Paul Dutta**, Y. Jiang, F. A Lima, V. Tiwari, C. Milne, T. Katayama, M. Coletta, E. K Brechin, T. J Penfold, and J O. Johansson, "Capturing Ultrafast Spin Dynamics in Single-Molecule Magnets Using Femtosecond X-ray Emission Spectroscopy", *The Journal of Physical Chemistry Letters* **16**(17), 4148–4154 (2025).

2. P. Su, J. Zhang, H. Wang, Y. Jiang, **S. Paul Dutta**, M. Li, H. Yousef, P. Zalden, K. Zhang, R. Zhu, X. Liu, Y. Wang, S. E. Canton, D. Jakobsen, D. Vinci, W. Zhang, J. Lan, X. Zhang, T. Weng, W. Yang, M. Wulff, C. Milne, D. Khakhulin, and Q. Kong, "Ultrafast solvent-modulated roaming mechanism in bromoform revealed by femtosecond X-ray solution scattering", *Nature Communications*, Published (09 February 2026).

Chapter 1

Introduction

The scientific progress has consistently been motivated by intrinsic curiosity to discover the principles governing the natural world. A comprehensive understanding of physical, chemical, and biological processes requires precise knowledge of molecular and atomic structures, as well as insight into their temporal evolution over time, which illustrates the structure-function relation principle - namely, that the properties, reactivity, and behavior of molecular systems are inherently determined by their geometric and electronic structure. Even subtle structural variations can lead to significant changes in chemical function, making structural characterization central to modern science. The discovery of X-rays by Wilhelm Conrad Röntgen in 1895 revolutionized structural science by enabling the determination of atomic structures through X-ray diffraction techniques using laboratory-based sources [1]. Over the past few decades, continuous advancement in X-ray sources has significantly expanded from early sealed tubes to high-brilliance third- and fourth-generation synchrotron light sources, allowing the structural investigations in atomic level and resulting to date in no less than 28 Nobel prizes. Even further pushing the frontiers of temporal resolution, X-ray free-electron lasers (XFELs) represent the most advanced X-ray sources.

In the 1970s, the observation of notable attractive interactions between two metal centers in low oxidation states captured significant attention and led to the introduction of metallophilic interactions, which has since become a distinct and widely studied phenomenon in coordination chemistry [2, 3]. These interactions can be seen in the bimetallic complexes involving closed-shell d^8-d^8 or d^{10}-d^{10} metal centers such as Au(I), Ag(I), Cu(I), Pt(II), or Pd(II) (see details in Section 1.2). Among these, the metallophilic interactions in Au(I), Ag(I), and Cu(I) complexes have been widely studied for their significant contributions to catalysis, sensing, photophysical properties, molecular recognition, and materials chemistry [4, 5]. Additionally, these bimetallic complexes are used in optoelectronic devices and photonic materials and have shown remarkable responsiveness to external stimuli such as light, heat, or solvent polarity. Such stimuli-responsive bimetallic complexes serve as efficient probes to study the dynamic nature of metal–metal interactions upon excitation and provide insights into excited-state structural dynamics. Understanding these ultrafast transformations is essential to design the functional molecular systems with tailored excited-state behavior.

In this context, synchrotron radiation facilities offer high flux and tunability across a wide photon energy window (0.1–100 keV), while XFELs additionally generate extremely intense and coherent femtosecond X-ray pulses (10–100 fs) via the self-amplified spontaneous emission (SASE) mechanism. Techniques such as laser slicing at synchrotrons despite the limited flux, further extend their utility to sub-picosecond time regimes, bridging the gap between conventional laser-based spectroscopy and ultrafast X-ray methodologies [6]. In 1999, Ahmed H. Zewail was awarded the Nobel Prize in Chemistry for his groundbreaking contributions to the field of chemical reaction dynamics using femtosecond time-resolved spectroscopy, which opened a new field called Femtochemistry [7]. The combination of laser excitation with ultrafast X-ray probe introduced new possibilities, making these ideal for time-resolved studies of electronically excited states, enabling direct observation of elementary chemical processes, such as bond breaking and formation, ultrafast electron transfer, and photoinduced isomerization on their intrinsic time scales in solution. Figure 1.1 illustrates the landscape of various X-ray and optical sources across the electromagnetic spectrum.

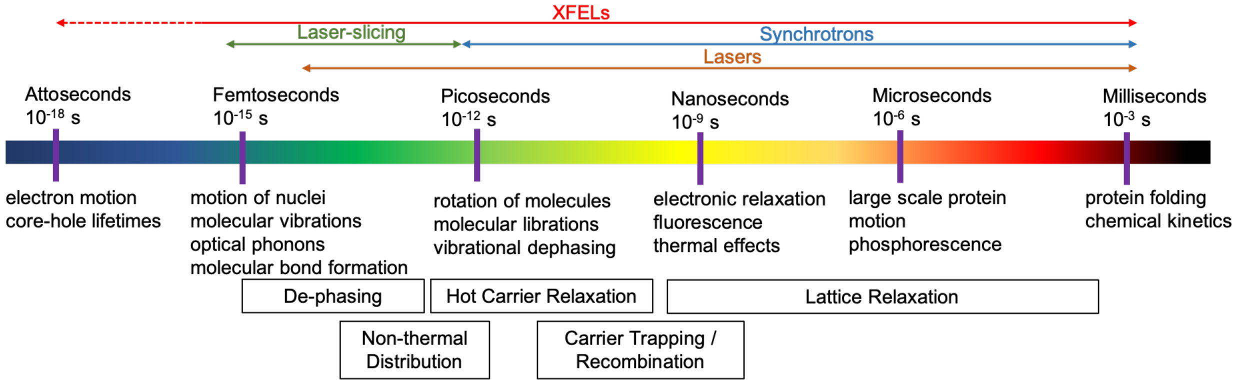

Figure 1.1: Time scales of various electronic and structural dynamics which occur during a chemical reaction and the available X-ray sources that can be used to access the different time scales.

The scope of this thesis is to investigate the evolution of the structural degrees of freedom in metal dimer systems after photoexcitation, and the structural dynamics by means of ultrafast X-ray techniques. In order to observe the ultrafast molecular dynamics of the metallophilic complexes, the experimental investigation has been carried out using X-ray absorption and time-resolved X-ray scattering techniques. The experimental results of these techniques are included and explained in this thesis. In the following sections, the conceptual background of the metallophilic interactions, objective of the thesis and the thesis outline are provided.

1.1 Photochemistry of stimuli-responsive bimetallic complexes

Stimuli-responsive bimetallic complexes have emerged as a versatile class of compounds, making them highly attractive for broad applications across catalysis, materials science, photochemistry, and biological systems. In this context, "stimuli-responsive" denotes complexes whose structural or electronic properties undergo well-defined changes upon application of external stimuli such as light irradiation, thermal perturbation, redox activation, or solvent polarity variations. These controlled responses provide an effective handle to tune their reactivity, excited-state dynamics, and functional output. In catalysis, bimetallic systems often exhibit synergistic effects between the two metal centers, leading to enhanced reactivity and selectivity [8]. Similarly, in materials chemistry, such complexes are being exploited in the design of optoelectronic devices, photoswitchable materials, and molecular machines [9,10]. From a biological perspective, photoresponsive metal complexes serve as models for metalloenzymes and are under active investigation for light-activated therapeutic agents and imaging probes [11,12]. The intrinsic photophysical and photochemical activities of these complexes are governed by metallophilic interactions, particularly for the formation of a new metal-metal bond or formation of the relevant excited state, delocalization of electron density and redistribution of vibrational energy.

The stimuli-responsive bimetallic complexes consist of two central metal ions, each bonded with one or more ligands or anions. The molecular orbital (MO) diagram provides a fundamental framework for understanding the electronic excited states of metal complexes and relevant electronic transitions after the photoexcitation [13,14]. Figure 1.2 illustrates the MO diagram with relevant electronic transitions for a bimetallic complex. After the absorption of visible light, an electron may be promoted from/to orbitals localized on the metal or the ligands. These electronic transitions in the regime of visible light can be defined as the following pathways:

- MC: Metal Centered transitions where the electronic transitions occur between orbitals located mainly on the metal center in both the ground and excited states (e.g. transitions between the e_g and t_{2g} orbitals).
- LC: Ligand Centered transitions where the electronic transitions happen between orbitals located mainly on the ligand parts. There is no significant net movement of electron density from one part of the ligand to another. (e.g. transitions between the π and π^* orbitals, or between n and π^* orbitals).
- MLCT: Metal-to-Ligand-Charge-Transfer transitions where the electronic transitions occur from orbitals located mainly on the metal center to orbitals located

mainly on the ligand part (e.g. transitions between the t_{2g} and π^* orbitals).

- LMCT: Ligand-to-Metal-Charge-Transfer transitions where the electronic transitions take place from orbitals located mainly on the ligand part to orbitals located mainly on the metal center (e.g. transitions between the π and t_{2g} or between the π and e_g orbitals).

- ILCT: Intraligand Charge Transfer transitions refer to a photoinduced electron transfer within the same ligand, from a donor moiety (an electron-rich group like amine or thiolate) to an acceptor moiety (electron-deficient groups like pyridinium, nitro, or carbonyl); usually from a π (donor) to π^* (acceptor) orbital. This results in partial charge separation within the ligand itself. Such transitions are sensitive to ligand structure and solvent polarity.

- LMMCT: Ligand-to-Metal–Metal Charge Transfer transitions occur when a photoinduced electron transfers from a ligand orbital (a non-bonding or π orbital) to a metal–metal bonding orbital in a bimetallic or polymetallic complex. This transition can influence metal–metal bond strength, potentially leading to bond contraction or formation in the excited state.

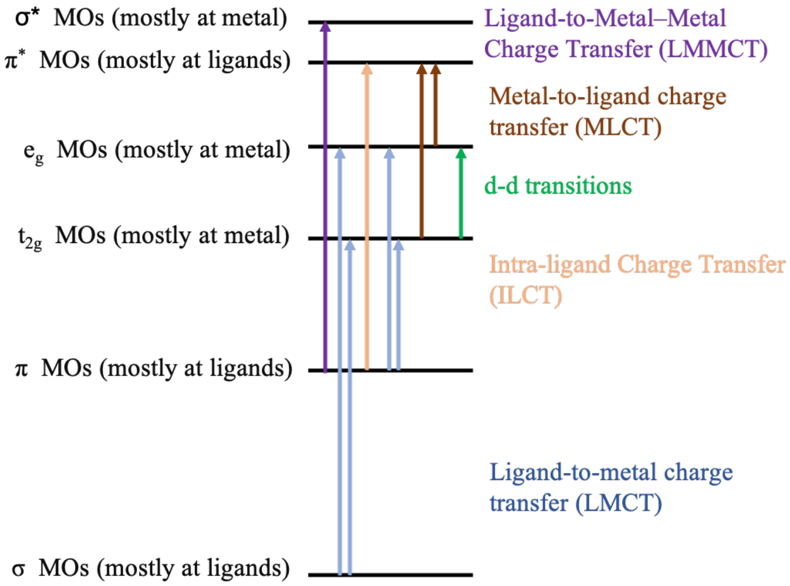

Figure 1.2: Different electronic transition within the metal complexes. The energy levels are denoted, based on the main orbital contributor and the assignment of the names are based on charge transfer character. The color coordinated arrows represent the particular transitions in the respective color.

The first four transitions are governed by the nature and energy alignment of the metal d-orbitals and ligand π or π^* orbitals. In bimetallic complexes, the presence of a metal–metal bonding or antibonding orbital further complicates the excited-state landscape, allowing for unique pathways (last two type transitions) involving transient bond strengthening or contraction, which are often observable via time-resolved X-ray spectroscopic or scattering techniques. This motivates the purpose of the thesis and influence the experimental characterization and analysis of the complexes under investigation.

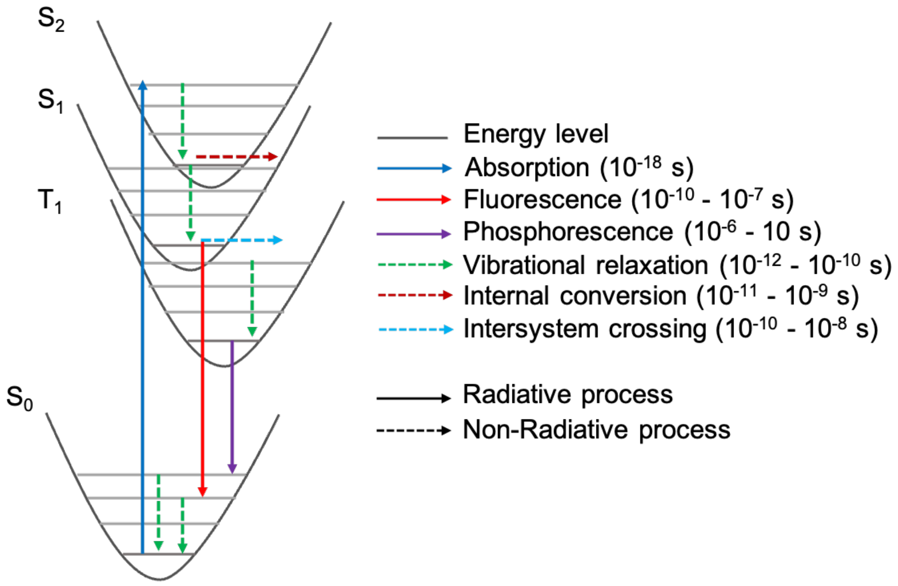

Figure 1.3: Jablonski diagram showing relaxation of an exited state through fluorescence, phosphorescence and vibrational relaxation.

The electronic transition of these bimetallic complexes are triggered upon photoexcitation and undergo vertical excitation to a higher electronic state according to the Franck–Condon principle [15]. This Franck–Condon excited state often does not represent the relaxed minimum-energy configuration on the excited-state potential energy surface [16]. If the transition to the Franck-Condon region results in a high vibrational energy level of the excited state, then it relaxes to the lowest vibrational state of that particular excited state through non-radiative deactivation. These transitions and relaxation pathways can be presented by the Jablonski diagram as illustrated in Figure 1.3. The electronic transitions in the system can happen from the ground state to many vibrational levels of an excited electronic state which result in broad bands in the ultraviolet-visible (UV-vis) spectrum.

The excited state of the system can return to the ground state via two principal pathways: (i) non-radiative decay or (ii) radiative decay (luminescence). In case of non-radiative decay, the electronic energy is dissipated as heat through internal conversion (IC) and vibrational relaxation to the surrounding environment. As both of the processes occur concurrently, the radiative decay must compete with non-radiative decay, and the efficiency of light emission is highly dependent on the relative rates of these processes. Luminescence is broadly categorized into fluorescence and phosphorescence, distinguished by their spin multiplicities and decay timescales. Fluorescence arises from radiative decay between excited and ground states of the same spin multiplicity (singlet–singlet transitions) [17]. It is a spin-allowed process and therefore occurs rapidly, with lifetimes in the range of nanoseconds. In contrast, phosphorescence involves radiative decay from an excited state with a different spin multiplicity than the ground state (triplet to singlet), making it a spin-forbidden process. The mechanism of phosphorescence typically involves an initial intersystem crossing (ISC), where the molecule undergoes a non-radiative transition from the initially excited singlet state to a lower-energy triplet state. This triplet state then acts as a metastable reservoir, from which radiative decay to the ground state can occur. Though spin-forbidden, phosphorescence becomes partially allowed in the presence of spin–orbit coupling, especially in heavy-metal complexes, which enhances both intersystem crossing and radiative triplet-to-singlet decay by relaxing spin-selection rules. As a result, phosphorescence is a common relaxation process in heavy-metal complexes, although it is still significantly slower than fluorescence and can persist from microseconds to milliseconds or longer, depending on the system and environment. Together, these pathways govern the electronic and structural evolution of the complex and determine the nature and lifetime of the photoexcited state thus strongly affecting the photophysical properties.

In this present work, we employ these principles to study metal complexes in solution and particularly focus on the ultrafast processes occurring on the fs-ps timescales. We use laser pump and X-ray probe methods to specifically address the relevant electronic and structural dynamics. In the following sections, detailed description of the metallophilic interactions are introduced followed by the objectives of this thesis.

1.2 Metallophilicity

The metallophilicity denotes the non-covalent attractive interactions between closed-shell metal centers, predominantly observed in complexes containing d^8–d^{10} transition metals or f^{14} lanthanides metal complexes [18]. These attractive interactions occur despite being closed-shell configuration, which theoretically should lead to repulsion according to the Pauli exclusion principle and electrostatic interaction. However, as commonly recognized this metallophilic attraction originates from a combination of relativistic effects, dispersion forces, and weak covalent or electrostatic interactions between the metal centers [19]. The strength of these resultant metal$\cdots$metal interactions is characterized by interaction energies typically ranging from 5 - 20 kJ/mol, which is comparable to the hydrogen bonding [20].

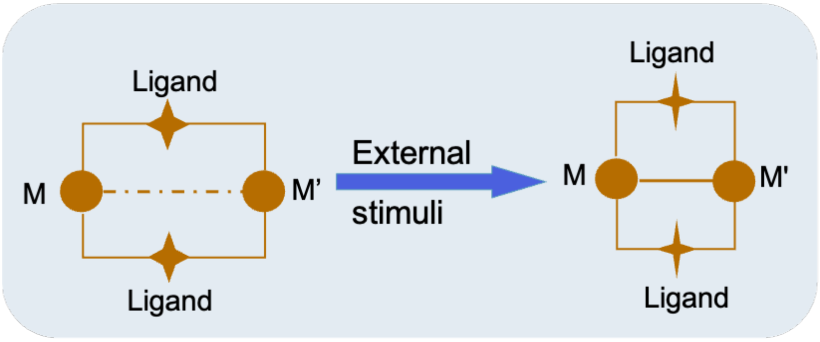

Figure 1.4: Representation of metallophilic interaction in ligand-supported bi-metallic complexes.

The term "metallophilicity" was first introduced in 1994, receiving wide recognition within the coordination chemistry community and rapidly becoming the focus of dedicated research efforts [21]. Thereafter, the concept has been significantly expanded and explored to the studies of the nature, origin, and implications of metallophilic interactions in various molecular systems and materials. Most of the in-depth investigations address various manifestations of metallophilicity, including both intra- and intermolecular interactions. However, the area of metallophilic interactions has evolved to include both homometallophilic (e.g., Au(I)···Au(I), Ag(I)···Ag(I) - see Section 1.3) and heterometallophilic (e.g., Au(I)···Pt(II), Au(I)···Ag(I) - see Section 1.4) interactions, broadening the conceptual framework and opening up a wide range of chemical systems to explore the interaction [22]. Further description of metallophilic interaction are included in the following sections.

Metallophilicity is widely recognized as a key driving force for the self-assembly of transition metal centers, which facilitate the formation of well-defined supramolecular architectures with d^{10}–d^{10} or d^8–d^8 electronic configuration. Such supramolecular architectures include aggregates and host-guest systems, formation of nanoparticles and clusters [23]. These self-assembled metallosupramolecular systems have found diverse applications which can be introduced by the modified chemical and physical properties that arise from the metallophilic interactions.

Owing to the remarkable photophysical and photochemical characteristics, metallophilic complexes are increasingly in demand for advanced functional materials. Their tunable electronic, and structural properties make them highly attractive for applications in advanced functional materials and highly photoluminescent systems, including organic semiconductors, biosensors, organic light-emitting diodes (OLEDs) [24, 25], and homogeneous photocatalytic systems [26]. The diverse applications of these complexes have sparked significant interest in further investigating the fundamental origin of metallophilic interactions, including detailed insights into electronic redistribution processes in the higher excited states upon photoexcitation.

The origin of metallophilicity has been the subject of ongoing discussion, regarding the relative importance of different contributing factors, particularly the contributions to the hybridization of spd atomic orbitals of the metal ions into the molecular orbitals of a metallophilic complex and the extent of relativistic effects. The metallophilic interactions have been extensively studied and fully supported by structural evidence obtained through the single-crystal X-ray crystallography [27, 28], complemented by various spectroscopic techniques including NMR, UV-Vis absorption [29], emission and Raman spectroscopy [30, 31], along with computational studies [32–35]. However, a comprehensive understanding of their nature is still evolving. The structural studies using the single-crystal X-ray diffraction indicate the short metal–metal ($M\cdots M'$, where $M' =$ M or M') distances that fall below the sum of the van der Waals radii, suggesting attractive interactions between the metal centers, illustrated in Figure 1.4. In contrast, several theoretical investigations, including density functional theory (DFT) and high-level coupled-cluster singles and doubles with perturbative triples [CCSD(T)] computations, indicate that at such short separations, closed-shell $M\cdots M'$ interactions are inherently repulsive, due to the strong Pauli repulsion between the filled metal orbitals [26].

Relativistic effects become increasingly significant for heavier elements and facilitate the (n + 1)s–nd and (n + 1)p–nd orbital hybridization in the metal centers. These interactions influence the overall balance of repulsive and attractive forces in metallophilic systems. Specifically, (n + 1)s–nd hybridization enhances $M\cdots M'$ Pauli repulsion and repulsive $M\cdots M'$ orbital interaction, leading to destabilization of the orbital overlap. In contrast, (n + 1)p–nd hybridization weakens the Pauli repulsion, favoring the shorter $M\cdots M'$ distances. This hybridization model has been used to rationalize the contradictory experimental observation that the intermolecular or intramolecular $Ag\cdots Ag$ distances are often shorter than the $Au\cdots Au$ distances, due to the intrinsically weaker Pauli repulsion in the $Ag\cdots Ag$ systems. Additionally, the role of connecting ligands is critical in modulating the $M\cdots M'$ interactions [26]. Despite the presence of ligand–ligand ($L\cdots L'$) Pauli repulsion, the linear coordination geometry of d^{10} metal complexes are effectively stabilized and promotes attractive dispersion forces between ligands, while maintaining overall structural stabilization. This cooperative interactions lead to a shorter $M\cdots M'$ distances than the sum of the van der Waals radius (r_{vdw}) of the metal centers, despite the absence of direct covalent bonding.

This thesis investigates the fundamental origin and nature of metallophilic interactions, with a particular focus on providing experimental evidence for their existence in the solution phase of various closed-shell metal complexes. Unlike in the solid state, where crystal packing forces and π-π stacking can significantly obscure or artificially enhance metal–metal contacts, the solution or gas phase offers a more intrinsic view of metallophilicity, free from such structural artifacts. In addition to establishing the presence of these interactions under solvated conditions, this work aims to elucidate how organic ligand frameworks, covalently coordinated to the metal centers, influence the strength and geometry of metallophilic interactions.

1.3 Homo-metallophilicity

The non-covalent attractive metal–metal interactions between the closed-shell same metal centers are known as homo-metallophilicity, illustrated in Figure 1.5 [18]. These interactions are observed extensively in closed-shell d^{10}–d^{10} (such as Au(I)–Au(I), Ag(I)–Ag(I), Cu(I)–Cu(I), Pd(0)–Pd(0) and d^8–d^8 (Rh(I)–Rh(I), Ir(I)–Ir(I), Pt(II)–Pt(II), and Pd(II)–Pd(II)) electronically configured transition metal complexes [36,37]. Structural evidence for homo-metallophilicity is predominantly obtained from single-crystal X-ray diffraction and solution phase EXAFS studies, where close metal–metal distances are consistently observed [38].

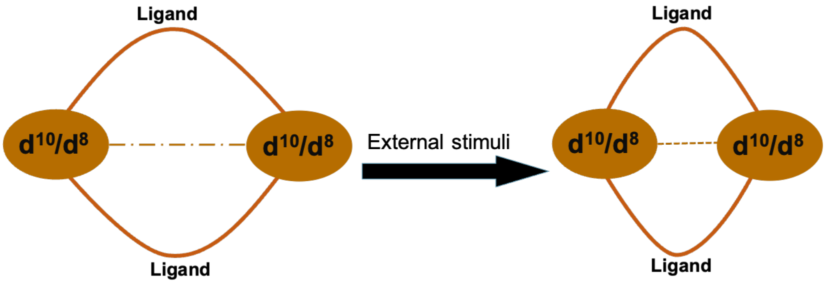

Figure 1.5: Formation of homo-metallophilic interaction in bi-metallic complexes with closed-shell d^{10}–d^{10} or d^8–d^8 electronic configuration

These specific metal–metal interactions influence the conformation, configuration, the stoichiometry of molecular species, and unusual aggregation modes in the condensed phase. Thus these inter- and intra-molecular interactions can co-determine the molecular and crystal structures of both neutral and ionic species, ultimately impacting the physical and chemical properties of the overall system. The optical, electronic, and mechanical properties of the bi-metallic complexes are influenced by these interactions which indicates their critical role in the design of luminescent complexes, metallosupramolecular assemblies, and coordination polymers [20,36]. The tunability of these properties by ligand environment, temperature, and solvent polarity makes homometallophilic systems highly attractive for applications in OLEDs, photocatalysis, and biosensing [39].

A striking example of ultrafast excited-state bond dynamics is the photoinduced Pt–Pt bond contraction observed in tetrakis-μ-pyrophosphitodiplatinate(II) ($(Pt_2(P_2O_5H_2)_4{}^{4-}$, PtPOP) in solution. Time-resolved X-ray scattering measurements in 100 ps to 1 μs timescale on such systems have revealed a significant shortening (approximately 0.24 Å) of the Pt-Pt distance upon optical excitation in solution, indicative of the formation of a metal-metal bond in the excited state [40,41]. Complementary femtosecond WAXS experiments have further demonstrated that this Pt–Pt bond formation begins within a few hundred femtoseconds, capturing the earliest structural rearrangements and underscoring the promptness of metallophilic bonding in the excited state [41]. Additionally, the investigation of ground- and excited-state structures of the bimetallic, ligand-bridged $[Ir_2(dimen)_4]^{2+}$ complex in acetonitrile reveal a bond shortening of approximately 1.4 Å in both singlet and triplet excited states. These structural contractions serve as direct evidence of the formation of metal–metal bonds in excited states and challenge traditional views that such dimers are weakly bound in solution [42].

The current thesis work mostly focused on the homometallophilic interactions in closed shell d^{10}–d^{10} Au(I)–Au(I), Ag(I)–Ag(I), and Cu(I)–Cu(I) complexes. Further specific details of these interactions are described in the respective sections.

1.3.1 Aurophilicity

In early 1970, strong evidence for significant attractive interactions between two linearly coordinated gold atoms were accumulated in the structural chemistry of molecular gold compounds [20]. Alongside the well-known lustre and "noble character", related to the extreme electrochemical potential, gold (Au) emerge in specific metal–metal interactions with its most common cationic (+1) oxidation state and closed-shell electronic configuration ($5d^{10}$) [18]. Such interaction was first named as 'aurophilicity', 'aurophilic interaction' or 'aurophilic bonding' in 1988 [43,44]. These terms came from the combination of 'aurum' (Latin for gold, used as symbol of element) and 'philein' (Greek for 'distinct preference' or 'affinity' or love).

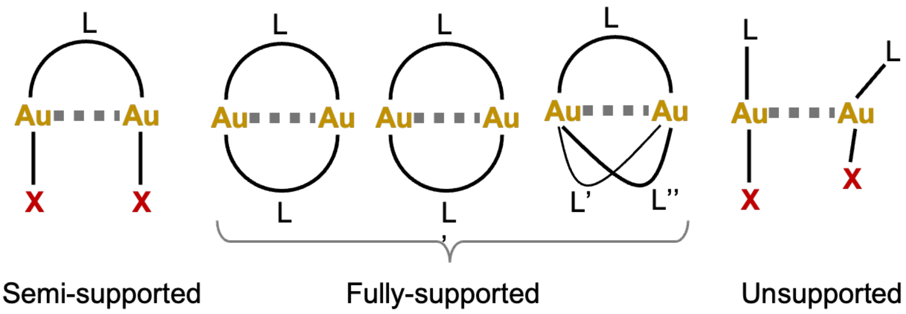

Figure 1.6: Schematic representation with variation of ligand supported and unsupported intramolecular aurophilic interactions.

To favor the aurophilic interaction, low coordination number is an important prerequisite, which minimizes the steric repulsions between ligands associated with the

Au atoms. Consequently, such attractive interactions are rarely observed in complexes with a coordination number more than two, although there are exceptions [45]. In our current investigation of aurophilic interaction is with coordination number of two.

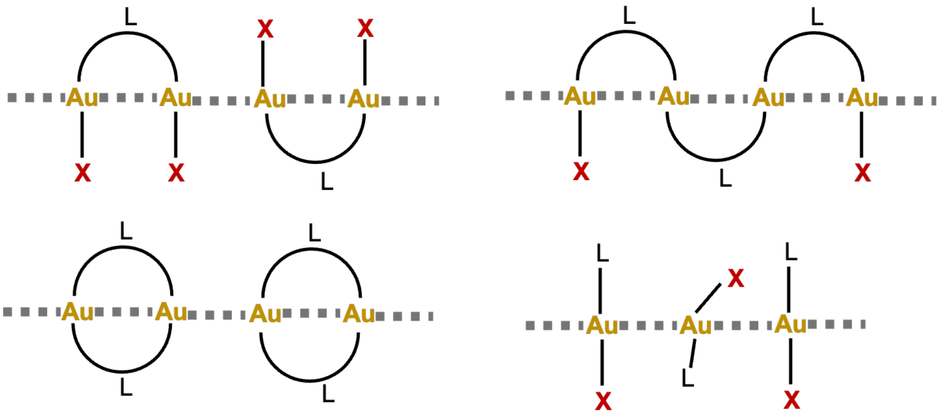

Figure 1.7: Schematic representation with variation of extended ligand supported and unsupported intermolecular aurophilic interactions.

Additionally, these aurophilic interactions generally occur at Au···Au distances shorter than the sum of van der Waals radii (~ 3.32 Å). This can be broadly categorized based on the degree of structural support offered by the ligands. The ligand-supported aurophilic interactions arise when the two Au(I) centers stay in close proximity by one or more bridging ligands, which contribute entropically to the stabilization of the Au···Au contact, as the pre-organization imposed by the bridging ligand reduces the conformational degrees of freedom. Figures 1.6 and 1.7 illustrate the organization of Au atoms by one (semi-supported) or two (fully supported) bridging ligands, adapted from [2]. In semi-supported systems a single difunctional ligand connects the two Au atoms and leaves one coordination site on each Au, occupied by a spectator donor. In case of fully-supported systems, both donors belong to the same bidentate or macrocyclic fragment, further shortening the contact and leading to helically twisted or macrocyclic architectures. Such interactions are generally intramolecular in nature. In rarer geometries with higher coordination numbers (3), three ligands may cooperatively enhance these interactions.

In contrast, unsupported aurophilic interactions are typically observed in supramolecular assemblies or solid-state structures without any direct bridging ligand between the interacting Au(I) centers. These interactions arise solely due to favorable relativistic dispersion forces and crystal packing effects. Such interactions are often intermolecular and more sensitive to solvent, temperature, or counter-ions. Consequently in these systems, the Au···Au distance is usually slightly longer. Irrespective of supported or unsupported by the ligands, the aurophilicity remains a defining structural interaction in the coordination chemistry of gold(I) complexes [2].

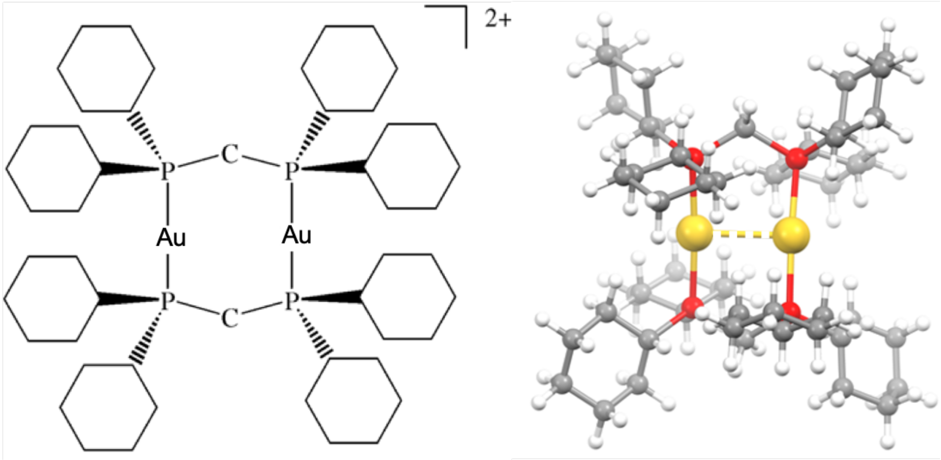

Figure 1.8: Molecular structures of the $[Au_2(dcpm)_2](PF_6)_2$ complex. Left: Schematic representation of $[Au_2(dcpm)_2]^{2+}$. Right: Molecular view of $[Au_2(dcpm)_2]^{2+}$ with color coordination of different elements.

For instance, the $[Au_2(dcpm)_2](PF_6)_2$ (dcpm = bis(dicyclohexylphosphino)methane) complex with two fully-supported chelating bisphosphine ligands exhibit strong intramolecular aurophilic interactions. Figure 1.8 represents the bimetallic $[Au_2(dcpm)_2]^{2+}$, which maintain the constrained Au···Au distance of ca. 2.9 Å favoring the aurophilic attraction. Each Au(I) center adopts a linear coordination geometry with the adjacent P centers (P–Au–P), stabilized by those bidentate dcpm ligands, which serve both as sterically bulky and electronically tunable phosphine donors. Due to the rigid nature of the dcpm ligand, two Au(I) centers stay with a constrained Au···Au distance, shorter than the sum of van der Waals radii (∼ 3.32 Å), indicating the closed-shell aurophilic interaction.

The aurophilic interaction of $[Au_2(dcpm)_2](PF_6)_2$ was first introduced in the 1980s by Schmidbaur and co-workers during their systematic investigation of phosphine-stabilized gold complexes [46]. After that, the intramolecular Au···Au interactions in $[Au_2(dcpm)_2](PF_6)_2$ complex attracted great scientific interest and was investigated further in various aspects including high-resolution crystallography and low-temperature photoluminescence in the 1990s and early 2000s. The crystallographic analysis revealed an Au···Au distance of ∼ 2.92 Å in the solid state, significantly below the van der Waals threshold [47, 48]. Supplementary investigation in combination with computational studies and relativistic effects, lead to the formulation of aurophilicity as a non-covalent force, driven by dispersion and relativistic orbital contraction in Au(I) centers [20].

The photophysical properties of these complexes have been extensively investigated, where *ab initio* study of the analogous binuclear complex, $[Au_2(dpm)_2]^{2+}$, revealed significant red-shifted phosphorescence [49]. The calculated triplet-state emission, $^3[Au(d\sigma^*) \rightarrow Au(p\sigma)]$, occurs at approximately ∼ 557 nm in acetonitrile, closely matching the experimental emission at $\sim 575\,\mathrm{nm}$ observed in the analogous $[Au_2(dppm)_2]^{2+}$ complex. This study also predicts the influence of acetonitrile solvent molecules on the excited state of the complex. These findings indicate that enhanced aurophilicity in the excited state is the key driver of both strong luminescence and spectral tuning in such binuclear Au(I) systems.

Recent time-resolved transient absorption (TRTA) and time-resolved emission (TRE) spectroscopic studies, have shown the formation of the intrinsic excimer within 0.15 ps in the triplet state ($^3[5d\sigma^*6p\sigma]$) of $[Au_2(dcpm)_2](ClO_4)_2$ complex without any solvent or phase intervention [50]. The excited triplet state decays to the ground state with a lifetime of $\sim 4.3\ \mu$s. In acetonitrile solution of $[Au_2(dcpm)_2](ClO_4)_2$ complex, rapid formation of an exciplex occurs with a time constant of ~ 4.5 ps, via coordination of solvent molecules which increases the coordination number (more than 2) of the activated Au(I). In contrast, the solution of $[Au_2(dcpm)_2](ClO_4)_2$ complex in dichloromethane, the relaxation pathway changes significantly. Here the initial triplet excited state undergoes a transformation into a phosphorescent triplet intermediate state within $\sim$ 510 ps, likely via C–X bond cleavage [50].

Regardless of the indication of the reduction of the Au···Au distance in the excited state, the timescales and structural dynamics through exciplex formation are still absent from current literature [51]. Additionally this study shows that the $^3[5d\sigma^*6p\sigma]$ state is viable and highly reactive, which proves this complex as a powerful reagent for photochemical reactions, making a representative example for further systematic studies on the structural dynamics of di-nuclear Au(I) complexes.

A further recent investigation using mass spectroscopy, supported by UV photodissociation spectroscopy, resulted an intriguing order of electronic transitions in gas phase for $[MM'(dcpm)_2](PF_6)_2$ complexes, where M, M' = Au(I), Ag(I), Cu(I), refer to the heterometallophilic interaction in Section 1.4. According to this study, the trend of lowest bright electronic transition follows the order: $Cu_2 < CuAu < CuAg < Au_2 < AgAu < Ag_2$, correlating with the strength of metallophilic interactions [52]. Additional quantum chemical GW-BSE (GW-Bethe–Salpeter-equation) calculations confirm the strengthening of the metal–metal bond in the excited state, predominantly influenced by metal-centered $^1MC(d\sigma^*–p\sigma)$ excitations. Furthermore, the variation of metal–metal bond distances in these complexes reveals that the increasing role of relativistic (n+1)s orbitals in Au, influences the degree of nd–(n+1)s/p orbital hybridization. This effect can play a central role in tuning metallophilicity and its photophysical properties. These comparative studies reveal that Au···Au interactions are significantly stronger and more luminescent than the Ag···Ag and Cu···Cu analogs which display weaker or even repulsive behavior in some coordination environments due to reduced relativistic contributions. Hence, this increases the interest to understand more of the structural restraint (via ligands) and electronic structure for tuning and designing strong aurophilic interactions.

In this thesis work, the $[Au_2(dcpm)_2](PF_6)_2$ complex (in Figure 1.8) was selected not only for its rigid, ligand-enforced bimetallic framework that maintains close Au···Au proximity, but more importantly, for its capacity to exhibit pronounced Au–Au interaction enhancement upon photoexcitation. To compliment the recent studies, it is crucial to include the time-resolved scattering data for this complex in solution phase, which will provide direct structural sensitivity to transient molecular rearrangement in the excited states.

However with increased number of ligand connecting the two gold ions, the molecular structure becomes more flexible thus the possibility of forming Au-Au interaction increases and the chances of forming steric hindrance decreases. In spite of the presence of the large phenyl ring R at the central nitrogen atoms, the mode of aurophilic bonding is strongly modified with significant changes. In addition to the hydrogen bonding between carboxylic and phenolic groups bonded with the aryl group R in the diphosphine ligand supported dinuclear gold(I) complexes $(AuCl)_2\{P,PC_6H_4N(CH_2PPh_2)_2(CO_2H)(OH)\}$, the aurophilic interaction is remarkably demonstrated in all the six isomers [53]. The Au$\cdots$Au separation in the ground state decreases from 6.179 Å to 3.0722 Å in these linear gold(I) complexes indicating the increase of the aurophilicity within this series. Another study shows that the interaction energy decreases by 27% for the perpendicular phosphine molecule, $[(XML)_2]$, by omitting the relativistic effects at fixed geometry, while varying the halogen (X = F, H, Cl, Me, Br, –C≡CH, I), phosphine (L = PH_3, PMe_3, –N≡CH), and metal (M = Cu, Ag, Au) centers. The extent of the interaction potential increases with the softness of the halogen group at the gold center and can be seen strongest in the $[(ClAuPH_3)_2]$ configuration [32].

As the previously chosen $[Au_2(dcpm)_2](PF_6)_2$ complex has conformational rigidity for the strong chelating bidentate dcpm ligand, the Au(I) centers stay effectively in close proximity and facilitate the aurophilic interactions. However, to gain deeper insights into the structural and electronic factors governing aurophilicity, particularly the influence of ligand flexibility and electron density redistribution, it is essential to alter the ligand environment surrounding the Au(I) centers. In this context, the pnnp - ligand based complexes $[Au_2(pnnp)_2]Cl_2$ and its mono-bridged analogue $[Au_2(pnnp)Cl_2]$, were investigated in this thesis as structurally distinct systems for comparative analysis of aurophilic behavior. These stimuli-responsive complexes can show photoluminescence in both solid and solution phases due to their modulation of aurophilic interactions [54].

In $[Au_2(pnnp)_2]Cl_2$ complex, the Au(I) centers coordinate with the cyclic bidentate ligand 1,5-bis(p-tolyl)-3,7- bis(pyridine-2-yl)-1,5-diaza-3,7-diphosphacyclooctane (pnnp). This ligand significantly alters the electronic environment with the presence of nitrogen and phosphorus atoms within a cyclic ring and involving the electron rich aromatic rings within the framework. These factors modify the electron densities around the Au(I) centers and provide unique ligand flexibility that significantly influences metal–metal interactions and allow for much larger changes of the Au-Au distance upon transition to the excited states as compare to the $[Au_2(dcpm)_2](PF_6)_2$ complex described above.

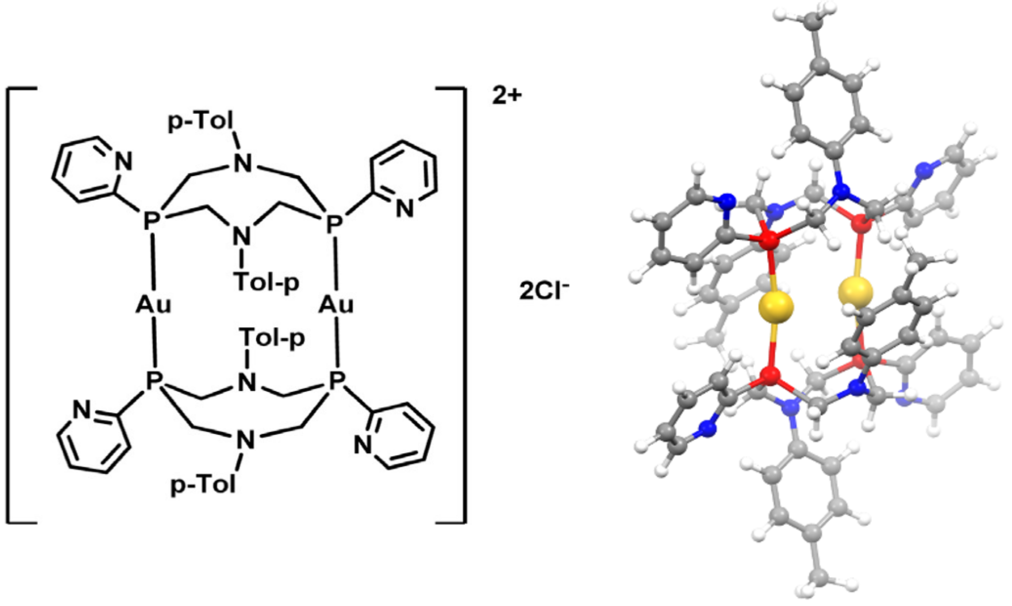

Figure 1.9: Molecular structures of the $[Au_2(pnnp)_2]Cl_2$ complex. Left: Schematic representation of $[Au_2(pnnp)_2]Cl_2$. Right: Molecular view of $[Au_2(pnnp)_2]^{2+}$ with color coordination of different elements.

The $[Au_2(pnnp)_2]Cl_2$ complex was initially synthesized and structurally characterized in 2014, highlighting the water solubility and modular coordination framework as a basis for supramolecular design [55]. The molecular structure of the complex is illustrated in Figure 1.9. The X-ray crystallography revealed a relatively short Au···Au distance, indicating an intramolecular aurophilic interaction stabilized by the spatial arrangement imposed by the macrocyclic pnnp ligand.

The follow-up studies by the same group in 2016 explored the photophysical properties of $[Au_2(pnnp)_2]Cl_2$ complex in greater details [56]. This study exhibit solvent-responsive luminescence, where the emission properties could be modified by non-covalent interactions with small organic molecules. The results indicate that the pnnp ligand offers geometric support for enhanced aurophilicity and permits dynamic structural adaptability, which identify this complex as a potential luminescent source. This confirms the critical role of the Au···Au interactions in excited-state and further underscored the relevance of aurophilicity in molecular recognition and sensing applications.

In structurally simpler $[Au_2(pnnp)Cl_2]$ complex, the Au(I) centers coordinate with the cyclic pnnp ligand from one side and the other site was fulfilled by ionic bonding with the chloride (Cl^-) ion. The molecular structure of the complex is illustrated in

Figure 1.10, adapted from [57]. The study of this complex offered valuable information regarding ligand and solvent-induced symmetry forming, coordination flexibility, and the resulting impact on Au···Au proximity [57]. This also includes the isolation of geometric and electronic contributions to aurophilic behavior by systematically reducing the degree of ligand support.

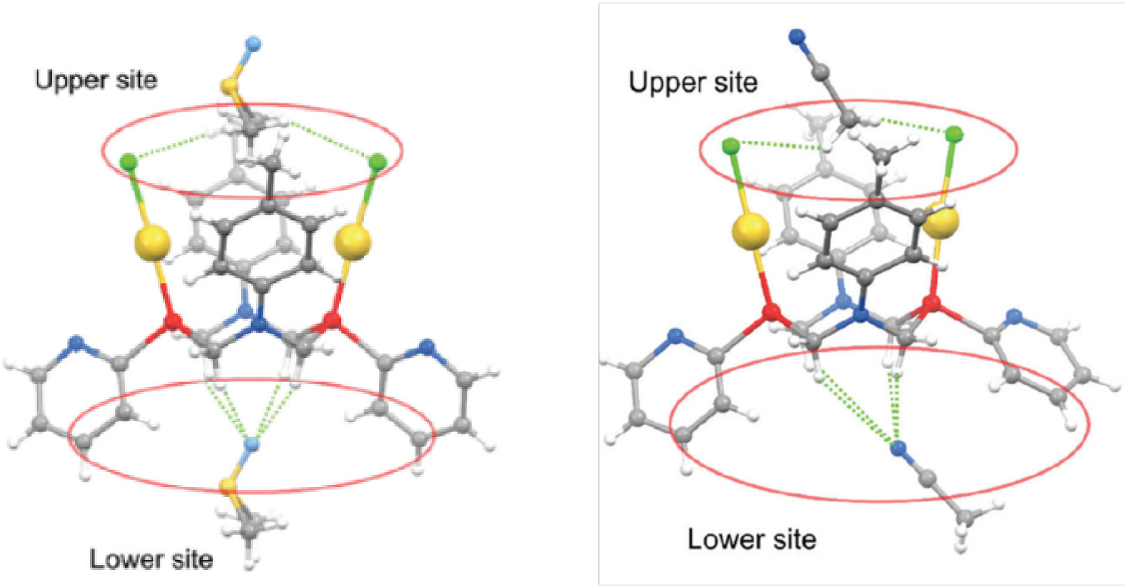

3. [Au$_2$(pnnp)Cl$_2$] in DMSO

4. [Au$_2$(pnnp)Cl$_2$] in acetonitrile

Figure 1.10: Single crystal molecular structures of the gold dimer in DMSO and acetonitrile.

In the solution phase, the [Au$_2$(pnnp)Cl$_2$] complex exhibits dynamic “host–guest” interactions with solvent molecules. Depending on the solvent polarity and the presence of hydrogen-bond acceptor atoms, the solvent molecules can bind either from the "upper" side near the AuCl moieties or from the "lower" face, or from both sides (refer to the Figure 1.10). Such coordination variability has been shown to significantly influence the photophysical properties of the complex. The striking differences in the luminescence efficiency and spectral shapes were also reported for acetonitrile, dimethyl sulfoxide (DMSO), and dichloromethane (DCM) solvent. These solvent-dependent variations directly modulate the degree of aurophilic interaction in the triplet excited state.

In acetonitrile and DCM solvent, the complex exhibits more asymmetric and loosely binding to the “lower” side, which allows the nitrogen lone pairs of the pyridyl moieties to adopt *anti*,*anti*-conformations and oriented away from the Au centers. As a result, the Au···Au distance remains nearly unchanged upon photoexcitation, and the formation of a stabilized aurophilic interaction in the excited state is effectively suppressed. In contrast, for DMSO solvent, the pyridyl moieties of the complex are forced to syn,syn–conformation in the ground state and upon excitation to the triplet state induces significant structural reorganization. This includes the emergence of a strong aurophilic interaction, evidenced by a contraction of the Au···Au distance from approximately 3.6 Å in the ground state to 2.9 Å in the triplet state, accompanied by ∼90° rotation of the pyridyl units around the P–C bonds.

This proposed structure–function relationship mediated by "host–guest" interactions remains conceptually well supported, but direct experimental evidence linking solvent-induced structural changes to excited-state aurophilicity is still lacking [58]. For this reason, a comparative experimental evaluation of these complexes could suggest the effect of number and orientation of bridging ligands on the aurophilic interaction.

In the context of this thesis work, both $[Au_2(pnnp)_2]Cl_2$ and $[Au_2(pnnp)Cl_2]$ complexes fit as model systems to understand how ligand topology and flexibility govern aurophilic interaction in solution.

1.3.2 Argentophilicity

In 1984, half a dozen structures with close Ag···Ag contacts had been observed, proposing 'some metal–metal interaction' or 'non-bonding contacts' in 'Structural Inorganic Chemistry' book [59]. Later this interaction was named as 'argentophilicity', 'argentophilic interactions', or 'argentophilic bonding', using the Latin word 'argentum' [60]. This refers to of weak, attractive interactions between closed-shell d^{10} Ag(I) centers, which are typically observed in d^{10}–d^{10} binuclear or polynuclear silver complexes.

The argentophilic interaction is largely attributed to relativistic effects and dispersion-type electron correlation, which allow for the overlap of diffuse 5s/5p orbitals and enable attractive interactions at distances shorter than the sum of van der Waals radii of silver atoms (∼3.44 Å). Similar to aurophilicity, the argentophilic interactions can be intermolecular, observed with single and multiple unsupported ligands, bonded between independent mono- or polynuclear units. The intramolecular argentophilic interactions are found with supported ligands in di- or polynuclear units [60]. Despite the weak nature of these interactions, it has been shown to significantly impact the geometry, electronic structure, and photophysical properties of silver complexes.

A variety of structurally characterized binuclear Ag(I) complexes demonstrate argentophilic interactions. For instance, the investigation of aliphatic phosphine ligands - supported binuclear silver(I) complexes were conducted and the analysis supported the theoretical calculations, indicating significant d^{10}–d^{10} overlap. The series of binuclear silver(I) complexes reveal argentophilic contacts with Ag···Ag distances of ∼ 2.8892 – 3.095 Å [30]. The UV-vis absorption spectra of these complexes indicate the $4d\sigma^* \rightarrow 5p\sigma$ transitions from Ag(I)···Ag(I) interactions. Moreover, time-resolved studies have provided evidence for structural changes upon photoexcitation that involve the transient strengthening or weakening of argentophilic interactions with high photoluminescence property, further illustrating the dynamic nature of these interactions in excited states [61].

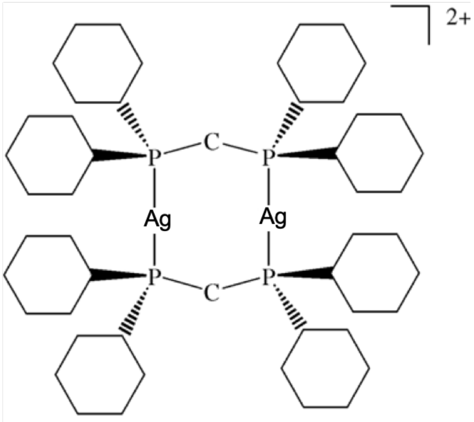

Figure 1.11: Schematic representation of the $[Ag_2(dcpm)_2](PF_6)_2$ complex.

Among all the well-known binuclear Ag(I) complexes demonstrating argentophilicity, the $[Ag_2(dcpm)_2](PF_6)_2$ complex stands out due to its well-defined rigid structure and strong argentophilic character. This complex has nearly linear Ag–P–Ag coordination and a short Ag···Ag distance of approximately 2.89 Å. Figure 1.11 illustrates the schematic structure of this complex. The PF_6^{2+} counter-ions ensure charge neutrality for overall complex, allowing clear structural insights via single-crystal X-ray diffraction. The UV-vis absorption band at 261 nm of $[Ag_2(dcpm)_2](PF_6)_2$ indicates the $4d\sigma^* \rightarrow 5p\sigma$ transitions from Ag(I)···Ag(I) interactions. This complex exhibits photoluminescence in the solid state at room temperature.

A follow-up investigation resulted on unraveling the photophysical behavior of $[Ag_2(dcpm)_2](PF_6)_2$ complex using advanced time-resolved spectroscopy. This study provides critical insight into the excited-state dynamics, emphasizing the role of argentophilic interactions in ultrafast relaxation processes. Using pump–probe fragmentation action spectroscopy, the study indicated that upon UV photoexcitation, the complex undergoes a rapid structural reorganization within 0.6/6 ps, associated with significant changes in the Ag···Ag distance [61]. This initial relaxation is followed by slower vibrational cooling on the picosecond timescale (100 ps). The comparative gas-phase and solution-phase studies show the crucial role of solvation in modulating the extent and timescale of the Ag···Ag rearrangement. These findings underline the dynamic character of argentophilicity and its direct involvement in the photophysics of coinage-metal complexes.

The significance of argentophilic interactions in the $[Ag_2(dcpm)_2](PF_6)_2$ complex extends beyond structural and spectroscopic aspects, serving as a fundamental model to explore non-covalent Ag(I)···Ag(I) interactions. In this PhD thesis, the $[Ag_2(dcpm)_2](PF_6)_2$ complex was included to perform the comparative study of the $[MM'(dcpm)_2](PF_6)_2$

complexes, where M, M' = Au(I), Ag(I), Cu(I). Further investigation and experimental details are explained in the following chapters.

1.3.3 Cuprophilicity

The attractive metal–metal interactions of closed-shell d^{10} copper(I) centers is known as cuprophilic interactions or cuprophilicity, similar to its heavier congeners aurophilicity and argentophilicity. The cuprophilic interaction was documented initially in 1978 and explained through *spd*-hybridization [62]. These interactions arise from a subtle balance of dispersion forces, weak relativistic effects, and metal-centered electron correlation [63]. The structural and spectroscopic studies pointed out unusually short Cu(I)···Cu(I) distances in a range of polynuclear copper(I) complexes, often below the sum of their van der Waals radii, providing evidence for the presence of attractive interactions between the Cu(I) centers. By the same token, the Cu(I)···Cu(I) distances are always shorter, around 2.5–2.7 Å, compared to their corresponding Ag(I)···Ag(I) and Au(I)···Au(I) distances observed in argentophilic and aurophilic complexes [60, 64].

These cuprophilic interactions are particularly favored in binuclear complexes, stabilized by bridging ligands such as phosphines, halides, carboxylates or polydentate ligands, which provide both geometrical preorganization and electronic environments to promote metal–metal overlap [20]. The strength and characteristics of these interactions are influenced by a variety of factors, including ligand electronic properties, coordination number, and counter-ion effects. Although relativistic effects are less pronounced in copper than in silver or gold, according to the quantum chemical calculations they still contribute to the bonding interactions, particularly when supported by π-accepting ligands that stabilize the d^{10} configuration and enhance dispersion interactions [65]. The cuprophilicity plays a critical role in supramolecular assembly, photophysical behavior, and electron transfer processes in multinuclear copper systems, influencing the applications of these complexes in various fields. The deep understanding of cuprophilic interactions continues to evolve with the advanced spectroscopic techniques, such as X-ray absorption spectroscopy and time-resolved X-ray scattering, which provide direct probing of the Cu···Cu spatial and electronic dynamics in both ground and excited states [66].

Among structurally well-characterized cuprophilic systems, the $[Cu_2(dcpm)_2](PF_6)_2$ complex (dcpm = bis(dicyclohexylphosphino)methane) is prominent as a typical example of a metal–metal bonded Cu(I) complex and aligns perfectly with the purpose of this thesis work. Figure 1.12 represents the schematic structure of the $[Cu_2(dcpm)_2](PF_6)_2$ complex. This was first synthesized and structurally characterized in 1994 with a remarkably short Cu···Cu distance of 2.564 Å, clearly indicative of a significant cuprophilic interaction. Here the dcpm ligand enforces a rigid geometry, allowing a direct comparison of metallophilic interaction with its homologous coinage metal complexes $[Au_2(dcpm)_2](PF_6)_2$ and $[Ag_2(dcpm)_2](PF_6)_2$. The observed Cu···Cu distance in this complex is shorter than the corresponding Ag···Ag and Au···Au distances [18, 67].

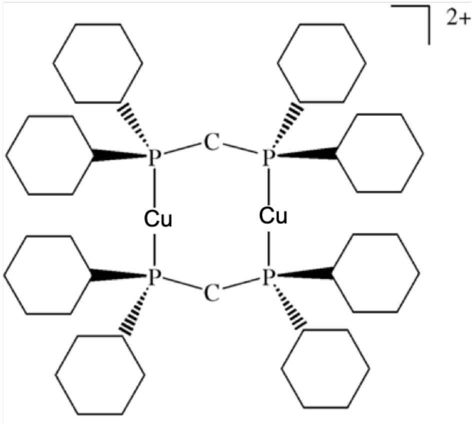

Figure 1.12: Schematic representation of the $[Cu_2(dcpm)_2](PF_6)_2$ complex.

While $[Au_2(dcpm)_2](PF_6)_2$ is known for its intense luminescence behavior, and $[Ag_2(dcpm)_2](PF_6)_2$ has been explored for its photophysical properties and halide sensing, the $[Cu_2(dcpm)_2](PF_6)_2$ complex has potential application in multinuclear photophysics, supramolecular chemistry, and catalysis. Recent studies have extended these complexes to heterometallic systems and explored the strength of the metal–metal bond and orbital hybridization, described in section 1.3.1 [68].

Compared to the gold and silver analogues, the $[Cu_2(dcpm)_2](PF_6)_2$ complex remains relatively underexplored in terms of its electronic structure, excited-state dynamics, and solution-phase behavior. Additionally, the nature of its excited states, the excited-state relaxation pathways, the influence of solvent interactions, and vibrational dynamics of the Cu···Cu interaction are still incomprehensible. This limits our ability to rationalize and predict the behavior of cuprophilic systems in photochemical or catalytic applications. Moreover, there remains an open question regarding how cuprophilic interactions persist or evolve in non-crystalline environments, such as in polar solvents or under X-ray photoexcitation. The comparative experimental studies across the Au, Ag and Cu analogues under identical conditions remain limited, which hinders a more complete understanding of the periodic trends in metallophilic interactions.

In this thesis, the investigation of the $[Cu_2(dcpm)_2](PF_6)_2$ complex addresses these gaps by investigating the time-resolved structural response in acetonitrile solution upon photoexcitation, with a focus on Cu···Cu bond modulation and ligand reorganization, utilizing time-resolved X-ray scattering to probe their excited-state structure.

1.4 Hetero-metallophilicity

Hetero-metallophilicity refers to attractive interactions between closed-shell d^{10} or d^{8} metal centers in low oxidation states of different elements, such as Au···Cu, Au···Ag, Cu···Ag, Au···Pt, or Ag···Hg [18]. Unlike homometallophilic interactions, hetero-metallophilic interactions exhibit directional preferences and distinctive bonding characters due to differences in electronegativity, size, and relativistic stabilization of the orbitals involved. These interactions are also characterized by inter-metallic distances shorter than the sum of van der Waals radii but longer than covalent bond lengths, suggesting a semi-bonding nature [64, 69].

The recent study of luminescence spectra and emission anisotropy of the alkynyl-phosphine Au-Cu cluster complex $[HC(PPh_2)_3Au_3Cu(C_2C_{13}H_{10}OH)_3Cl]$ in different experimental conditions: amorphous solid, solution, and crystalline phases reveal different relaxation pathways in different conditions. There is almost no conformational relaxation in the triplet state (T^1) in amorphous solid, whereas significant red shift of emission energy is observed on the conformational relaxation in the T^1 state in solution phase [70].

Another study of stimuli-responsive $[Au_2(dpam)_2][CuCl_2]_2$ and $[Au_2(dppm)_2][CuCl_2]_2$ complexes with bis(diphenylarsino)methane (dpam) and bis(diphenylphosphino)methane (dppm) ligands, reveals the formation of four-metal chain as Cu···Au···Au···Cu, connected through homo- and hetero-metallophilic interactions [71]. The intense phosphorescence (quantum yields up to 0.97) at room temperature, are supported by the DFT calculations with the co-existence of both homo- and hetero-metallophilic interactions. This opens up new opportunities for the further investigations of the efficient emission, phase transition behaviors, and effects of diarsine and diphosphine ligands on the properties of these hetero-metallophilic interactions [72].

The significance of hetero-metallophilicity extends beyond structural considerations, impacting luminescence, redox properties, and catalytic behavior. For instance, in photophysical applications, hetero-metallic complex involving Au(I) and Cu(I) often exhibit phosphorescence at room temperature due to enhanced spin–orbit coupling introduced by gold, which facilitates inter-system crossing and promotes emission from triplet states. Therefore, understanding and exploiting hetero-metallophilic interactions is crucial for the design of multi-metallic complexes with tailored electronic and functional properties.

Considering all these facts, a further extension of this thesis work has been initiated to investigate such hetero-metallophilic interactions in solution and solid state, and indicated in Section 8.1.

1.5 Objective

One of the key objectives of this thesis is to investigate the structural and electronic factors governing aurophilic interactions in the binuclear gold(I) complex $[Au_2(dcpm)_2](PF_6)_2$. This complex was chosen as a model system due to its well-defined, ligand-constrained geometry, which enforces close Au···Au proximity, and due to its well-documented significant enhancement of Au–Au interactions in the excited-state. In this thesis, the ab initio synthesis and related preliminary characterization of the $[Au_2(dcpm)_2](PF_6)_2$ complex are described. The following chapters includes experimental quantitative determination of the Au-Au distance and ligand architecture in the ground state in acetonitrile solution phase, performed by means of extended X-ray absorption fine structure (EXAFS) measurements around the gold L_3-edge. EXAFS enables element-specific probing of local coordination environments, revealing precise short-range structural details around the gold centers, such as Au–P and Au···Au distances, and thus allowing to refine the solution phase ground state structure of the complex. As the next step, the time-resolved wide-angle X-ray scattering (TR-WAXS) measurements were employed to characterize the transient molecular conformation, refine the structure of excited state of the complex in solution. TR-WAXS complements the investigation by capturing simultaneously the subtle intramolecular and medium-range intermolecular structural changes thus providing the global sensitivity to the changes in the complex, its solvation and solvent thermalization. The combined result of these two experiments in the solution phase should reveal full structural evolution over the photoexcitation and relaxation processes and thus aid in understanding the full photophysics cycle of the complex as a plausible potential energy diagram. More detailed analysis of this are explained in Sections 6.3.1 and 7.1.

Additionally, the other two structurally similar complexes, $[Au_2(pnnp)_2]Cl_2$ and $[Au_2(pnnp)Cl_2]$ complexes were similarly synthesized and characterized. To obtain detailed structural information under solution-phase conditions, TR-WAXS measurements were performed in $[Au_2(pnnp)_2]Cl_2$ complex for investigation of solvent-mediated structural dynamics, and extend of enhanced aurophilic interaction in excited state, offering complementary insights to those obtained from theoretical and crystallographic studies. More detailed information are explained in Sections 6.3.4 and 7.2.

For $[Au_2(pnnp)Cl_2]$ complex, the solute contribution in WAXS signal in solution was very weak and lacked sufficient contrast for reliable structural interpretation. The low scattering intensity, combined with overlapping contributions from solvent background and possible dynamic disorder, made it highly challenging to extract the meaningful structural parameters from the experimental data. As a result, the WAXS analysis was not included further for this complex.

1.6 Thesis outline

This thesis includes the study of ultra-fast structural dynamics using both experiments and analysis. The thesis is organized with different chapters as follows:

Chapter 2 introduces the theoretical description of X-ray scattering, X-ray absorption spectroscopy and the theoretical calculation used in the modeling of the bimetallic molecular system under study.

Chapter 3 describes the experimental setups and data collection strategies used for the ultrafast time-resolved X-ray scattering and X-ray absorption spectroscopy experiment performed at XFEL and synchrotrons on transition metal dimer complexes in solution.

Chapter 4 describes the detailed synthetic procedures for the preparation of transition metal dimer complexes and their characterization using common available techniques.

Chapter 5 outlines the data reduction methods with different reduction steps for the collected EXAFS data from P64 beamline and ground state structure refinement for $[Au_2(dcpm)_2](PF_6)_2$ complex.

Chapter 6 outlines the data reduction methods with different reduction steps for the collected WAXS data from FXE beamline at European XFEL, along with the data analysis methods used to determine the structural dynamics of bimetallic complexes studied in this thesis. This section also includes most of the experimental results.

Chapter 7 presents the detailed analysis and discussion of the experimental results with the data interpretation of the bimetallic transition metal complexes.

Chapter 8 provides the main conclusions of the research work and the future perspective of the project to investigate the metallophilic interactions.

Chapter 2

Experimental Methods

This chapter provides a concise overview of the theoretical background used in this dissertation. It briefly introduces the fundamental principles of X-ray scattering and absorption techniques, particularly the Wide-angle X-ray scattering and Extended X-ray Absorption Fine Structure. These two techniques were extensively employed in this work to investigate the origin of aurophilicity in the Au-dimer complexes in solution, specifically in the context of aurophilic interactions and Au-Au distance shortening in the excited-state. For a more comprehensive and detailed description of these topics, readers are referred to relevant literature sources.

2.1 X-ray Scattering

When X-rays illuminate a molecular system, an interaction occurs between the electric field of the incident X-ray light and the electrons within the sample, causing the light either to be absorbed or to scatter in various directions. X-rays are high-energy electromagnetic waves that in the non-resonant case induce the acceleration of the tightly bound core electrons in the illuminated atoms. Because of this acceleration, a secondary radiation is emitted. According to the classical electromagnetic theory, this radiation is known as the scattered radiation. This X-ray scattering phenomena are classified into two categories: elastic scattering and inelastic scattering. In the case of elastic scattering, the energy (and wavelength) of the scattered photons remains unchanged, and at larger distances it forms a wave with the same frequency as the incident beam [73, 74]. In contrast, during the inelastic scattering, an energy transfer occurs from the incident photon to the electron which results the re-emission of a photon with lower energy, and the ejection of a recoil (free) electron. When the photon interacts with a loosely bound outer-shell electron, then this inelastic scattering phenomenon is known as the Compton scattering [75, 76].

In elastic X-ray scattering, the spatial distribution of electron density within the sample gives rise to interference patterns in the scattered intensity, and those patterns are directly related to atomic positions or rather interatomic distances and thus to the structure in the probed volume.

The scattering amplitude, $A(q)$, of the X-ray wave is given by Equation 2.1

$$A(\mathbf{q}) = \int \rho(\mathbf{r})\, e^{-i\mathbf{q}\cdot\mathbf{r}}\, d\mathbf{r} \tag{2.1}$$

where $\mathbf{q}$ is the momentum transfer, $\rho(\mathbf{r})$ is the electron density of the sample, and $\mathbf{r}$ is the three-dimensional position vector. This equation can also be written in terms of the electron density as [77]

$$\rho_e(\mathbf{r}) = \frac{1}{(2\pi)^3} \int A(\mathbf{q})\, e^{i\mathbf{q}\cdot\mathbf{r}}\, d\mathbf{q} \tag{2.2}$$

The momentum transfer $\mathbf{q}$ is defined as the difference between the wavevectors of the incident $\mathbf{k}_0$ and the elastically scattered $\mathbf{k}$ X-ray waves, i.e., $\mathbf{q} = \mathbf{k} - \mathbf{k}_0$. These wave vectors are directly related to the X-ray wavelength λ, where the magnitude of the wave vectors are equal, is given by

$$|\mathbf{k}_0| = |\mathbf{k}| = \frac{2\pi}{\lambda}, \tag{2.3}$$

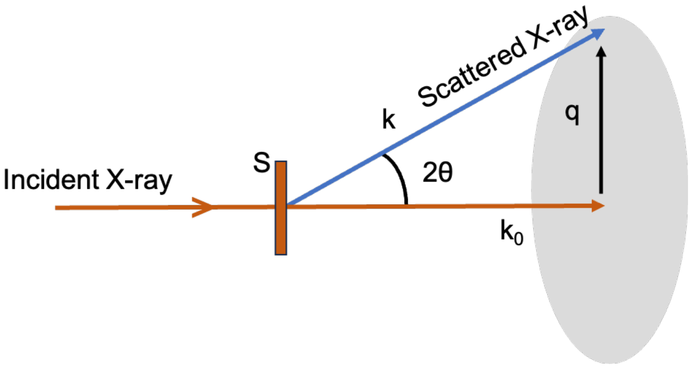

Figure 2.1: Schematic representation of momentum transfer in X-ray scattering. The incident X-ray hits the sample (S) and scattered with scattering angle 2θ.

$\mathbf{q}$ is consequently linked to the X-ray scattering angle θ through the schematic illustration (Figure 2.1), where θ is half the scattering angle between $\mathbf{k}$ and $\mathbf{k}_0$.

The magnitude of the momentum transfer is expressed as:

$$|\mathbf{q}| = \frac{4\pi}{\lambda} \sin\theta \tag{2.4}$$

These expressions establish the geometric and physical connections between the scattering process and the experimental observable quantities, enabling the investigation of structural and dynamical properties of molecular systems in solution.

For the calculation of X-ray scattering from a molecule, there are two conceptual steps involved. Firstly, the scattering from a single molecule is evaluated with the consideration of the interference among X-rays scattered by (mostly) core electrons of individual atoms within the molecule. The corresponding intensity is derived in B.E. Warren's foundational book on X-ray diffraction, and is expressed as [78],

$$S(\mathbf{q}) = \sum_m f_m(\mathbf{q}) e^{i\mathbf{q}\cdot\mathbf{r}_m} \sum_n f_n(\mathbf{q}) e^{-i\mathbf{q}\cdot\mathbf{r}_n} = \sum_{m,n} f_m(\mathbf{q}) f_n(\mathbf{q}) e^{i\mathbf{q}\cdot\mathbf{r}_{mn}} \tag{2.5}$$

where:

- the indices m and n, include all the atoms in the sample,
- f_m, f_n are the atomic form factors of m^{th} and n^{th} atoms, respectively as a function of the scattering vector magnitude q,
- $\mathbf{r}_m$, $\mathbf{r}_n$ are the position vectors of respective atoms,
- $\mathbf{r}_{mn} = \mathbf{r}_m - \mathbf{r}_n$ is the interatomic distance vector between atoms m and n,

In the expression, the summation extends over all the pairs of atoms in the sample to consider the overall contribution.

For liquid samples, the probed volume represents an ensemble of randomly oriented molecules. For these random molecules irrespective of their symmetry or lack of crystallinity, the orientational averaged signal are considered and described by the Debye scattering function [79]. The Debye formula performs the isotropic averaging of $S(\mathbf{q})$ into $S(q)$. The total elastic scattering intensity, $S(q)$ is then expressed as:

$$\begin{aligned} S(q) &= \sum_{m,n} f_m(q) f_n(q) \frac{\sin(qr_{mn})}{qr_{mn}} \\ &= \sum_n f_n^2(q) + \sum_n \sum_{m\neq n} f_n(q) f_m(q) \frac{\sin(qr_{nm})}{qr_{nm}} \end{aligned} \tag{2.6}$$

The atomic form factors are the Fourier transform of the electron density $\rho(\mathbf{r})$ of respective atoms [77], alternatively known as scattering amplitude and expressed as

$$f(q) = \int \rho(r)\, e^{(-iq\cdot r)}\, dr \tag{2.7}$$

Equation 2.6 is the key working formula for scattering, particularly for gas-phase scattering. Due to the disordered nature in liquid samples, the enormous number of possible combinations of distances in m and n atoms, makes the Debye equation nearly impractical. Therefore, it is convenient to introduce the pair distribution functions,

$g_{nm}(r)$ for atom types n and m to describe liquid structure rather than a set of individual distances used in Debye formula and this can be defined as: $g_{nm}(r) = \rho_{nm}(r)/\rho_{nm,0}$, where $\rho_{nm}(r)$ is the radial number density, expressed as $\rho_{nm}(r) = dN_m(r)/4\pi r^2\,dr$ of species m at a distance r from an atom of species n, and $\rho_{nm,0}$ is the corresponding average number density in an ideal gas (i.e., in the absence of any structural correlations). In other words, the pair distribution function $g_{nm}(r)$ is the normalized density of probability to find atom m at a distance (r) from atom n.

At very short interatomic distances, the radial distribution function $g(r)$ is essentially zero, since the strong repulsive interactions prevent atoms from approaching closer than the sum of their atomic radii. At intermediate distances, $g(r)$ displays distinct peaks corresponding to the interatomic distances within the first two or three coordination shells. As the r increases further, the amplitude of these peaks progressively diminishes and the features broaden, indicating the loss of structural correlation over longer distances. Eventually, at sufficiently large r, the $g(r)$ approaches a value of 1 as the density tends to its average value [80].

After considering all the facts, the scattered intensity, $S(q)$ can be rewritten as:

$$S(q) = \sum_n N_n f_n^2(q) + \sum_n \sum_{n \neq m} \frac{N_n N_m}{V} f_n(q) f_m(q) \int_0^\infty [g_{nm}(r) - 1] \frac{\sin(qr)}{qr} 4\pi r^2\,dr \quad (2.8)$$

where the indexes n and m include pairs of all atom types, N_n is the number of n-type atoms and V is the volume of the liquid sample. $4\pi r^2 g_{nm}(r)\,dr$ in the equation is the probability of finding a m-type atom at the distance r from an n-type atom [77].

The total scattering signal collected during the experiment also contains inelastic X-ray scattering. However, without the energy resolution, this component does not contain any structural information of the samples as the phase of the photons is lost in this process [79]. In this thesis, we are focusing on the investigation of the structural changes, and subtracted the inelastic X-ray scattering components in the difference scattering signal.

2.1.1 Scattering from solution

In the present thesis, the X-ray scattering technique is employed to investigate the metal-dimer complexes in acetonitrile solvent. Hence, a thorough understanding of the theoretical background underlying X-ray scattering from solutions is essential and presenting the expressions of solution scattering signals is crucial for interpreting the experimental data.

A liquid solution consists of two components: a minor component (the solute) dispersed within a major component (the solvent). Therefore, for a solution, the total

X-ray scattering signal can be described by three distinct contributions as dictated by the analysis methodology:

- the scattering only from the solute molecules, denoted as $(S(q)_{solute})$
- the scattering only from the solvent molecules, denoted as $(S(q)_{solvent})$
- the scattering from the solute–solvent interactions, referred to as the solute–solvent cross-term or "cage" contribution, denoted as $(S(q)_{cage})$

and the total scattering signal can be defined as

$$S(q) = S_{\text{solute}}(q) + S_{\text{cage}}(q) + S_{\text{solvent}}(q) \tag{2.9}$$

The equation 2.8 can be further refined for the solution by regrouping the atomic indices m and n according to whether they belong only to solute atoms, solvent atoms, or solute–solvent pairs.

$$\begin{aligned} S_{\text{solute}}(q) = & \sum_{n_{(\text{in solute})}} N_n f_n^2(q) \\ & + \sum_{n_{(\text{in solute})}} \sum_{m \neq n} \frac{N_n N_m}{V} f_n(q) f_m(q) \int_0^\infty g_{nm}(r) \frac{\sin(qr)}{qr} 4\pi r^2 \, dr \end{aligned} \tag{2.10}$$

$$\begin{aligned} S_{\text{cage}}(q) = & \sum_{n_{(\text{solute-solvent})}} N_n f_n^2(q) \\ & + \sum_{n_{(\text{solute-solvent})}} \sum_{m \neq n} \frac{N_n N_m}{V} f_n(q) f_m(q) \int_0^\infty \left[g_{nm}(r) - 1\right] \frac{\sin(qr)}{qr} 4\pi r^2 \, dr \end{aligned} \tag{2.11}$$

$$\begin{aligned} S_{\text{solvent}}(q) = & \sum_{n_{(\text{in solvent})}} N_n f_n^2(q) \\ & + \sum_{n_{(\text{in solvent})}} \sum_{m \neq n} \frac{N_n N_m}{V} f_n(q) f_m(q) \int_0^\infty \left[g_{nm}(r) - 1\right] \frac{\sin(qr)}{qr} 4\pi r^2 \, dr \end{aligned} \tag{2.12}$$

The scattering part only from the solute equals to the gas-phase scattering and the indices n and m indicate the all atom types within the solute molecules. If the solution is very diluted such that the solute molecules are sufficiently separated, then the inter-solute interactions are negligible, and the interference contributions between different solute molecules can be ignored in the typical ranges of covered momentum transfer. Therefore, the scattering contribution from the solute is easily calculated from atomic coordinates of the solute. The solute-solvent term in equation 2.9 is due to the cross interference between solute and solvent molecules in the first solvation shells which represents the local organization of solvent molecules around the solute, often referred to as the "cage" structure. The indices n corresponds to atom types within the solute and m refers to atom types in the solvent. The last term originates from the solvent-solvent correlations, known as solvent term where both the indices n and m run over atom types exclusively within and between solvent molecules. This solvent term describes the structural properties of the bulk solvent and these properties are strongly influenced by thermodynamic parameters such as temperature, pressure, and density, as explained in section 2.1.

2.1.2 Time-resolved X-ray scattering

During the time-resolved scattering experiment, a small fraction of the sample undergoes structural or electronic changes upon photoexcitation (perturbation). Therefore, the net signal is obtained by subtracting the scattering pattern of the unperturbed (ground-state) sample from that of the perturbed (excited-state) sample. This resulting difference scattering signal reflects only the structural changes induced by the photoexcitation and eliminates the static background. Similar to the total scattering signal expressed in Equation 2.9, the difference scattering signal can be decomposed to three components. Thus, the expression for $\Delta S(q,t)$ is structurally similar to that of the total scattering, but each term is now a time-dependent difference quantity:

$$\Delta S(q,t) = \Delta S_{\text{solute}}(q,t) + \Delta S_{\text{cage}}(q,t) + \Delta S_{\text{solvent}}(q,t) \tag{2.13}$$

where, the solute-only term represents the changes in the solute structure; the cage term describes the changes in the solute–solvent correlations (variations in solvation shell structure or solvation dynamics); the solvent-only term reflects the thermodynamic changes in the bulk solvent (e.g., due to heating and subsequent thermal expansion).

The first two terms of equation 2.13 are considered as the solute-related contribution and can be expressed as

$$\Delta S_{\text{solute}}(q,t) + \Delta S_{\text{cage}}(q,t) = \frac{1}{R}\left[\sum_k c_k(t)S_k(q) - c_g(t)S_g(q)\right] \tag{2.14}$$

where,

- k: index of the solute molecules (including reactants, intermediates, and products),
- $c_k(t)$: the concentrations of the k^{th} species as a function of time t,
- $S_k(q)$: solute-related (solute + cage) scattering intensity of species k,

- $S_g(q)$: scattering intensity of the reactants (k = reactants),
- R: scaling factor, the number of solvent molecules per solute molecule (i. e. one liquid unit cell).

The equation 2.14 assumes that the time-dependent scattering signal can be factorized into a product of two terms, $c_k(t)S_k(q)$, where $c_k(t)$ is time-dependent concentration and $S_k(q)$ is time-independent species-specific scattering signature. This factorization inherently considers that the transitions between the electronic or structural states occur on an ultra-fast timescale.

For the ground and excited state structures, the solute signals are generally calculated from the theoretical calculations, most commonly using Density Functional Theory (DFT). The corresponding cage signals are evaluated using Molecular Dynamics (MD) simulations.

For solutes containing multiple high-Z atoms and undergoing significant overall structural rearrangements, the solute contribution typically dominates the scattering signal and the cage term contributes only marginally [40, 42]. In contrast, with only a single heavy atom and minimal structural changes in the solute, but where photoexcitation induces large charge redistribution and consequently strong solvation effects, the cage contribution may even become the dominant term. However, it is important to mention that in this thesis, the cage contributions were neglected during the experimental analysis as the collected experimental data sets contain extended q-range (high spatial resolution) with major contribution from the structural rearrangement in the bimetallic complexes. The validity of this approach is confirmed by MD simulations in the thesis, showing that the cage term primarily contributes in the q range outside of the one used for solute signal analysis.

The $\Delta S_{\text{solvent}}(q,t)$ contribution is very sensitive to the thermodynamic state (such as temperature, and density) of the bulk solvent. These states may vary during the photoexcitation experiment due to the energy transfer from light-absorbing solute molecules to the neighboring solvent molecules. The excitation then followed by a relaxation to equilibrium with the surrounding environment of the scattering volume. According to the well-established methodology, the temporal progression of the solvent response following photoexcitation can be expressed as a linear combination of two independent thermodynamical variables, temperature and density [81, 82]. In the analysis of metal-dimer complexes, we also considered temperature and density as the thermodynamical variables. Now, the solvent scattering signal change can be expressed as

$$\Delta S_{\text{solvent}}(q,t) = \left(\frac{\partial S}{\partial T}\right)\Delta T(t) + \left(\frac{\partial S}{\partial \rho}\right)\Delta\rho(t) \tag{2.15}$$

where, $\Delta T(t)$ is the temperature change and $\Delta\rho(t)$ is the density change at the time delay t with respect to those before the photoexcitation. These values can be first estimated and fitted based on the known values of the energy differences between the transient species and the ground state, the hydrodynamic properties of the solvent, and the parameters of laser beam parameters [82].

The two partial derivatives $\left(\frac{\partial S}{\partial T}\right)_\rho$ and $\left(\frac{\partial S}{\partial \rho}\right)_T$ are considered as time-independent components related to the solvent and can be determined from separate measurements, either from molecular dynamics (MD) simulations or through solvent-heating experiments using a dye containing solution [81].

Hence the Equation 2.13 for total scattering can be written as

$$\Delta S(q,t) = \Delta S_{\text{solute}}(q,t) + \Delta S_{\text{cage}}(q,t) + \left[\left(\frac{\partial S}{\partial T}\right)\Delta T(t) + \left(\frac{\partial S}{\partial \rho}\right)\Delta\rho(t)\right] \tag{2.16}$$

$$\Delta S(q,t) = \frac{1}{R}\left[\sum_k c_k(t)S_k(q) - c_g(t)S_g(q)\right] + \left[\left(\frac{\partial S}{\partial T}\right)\Delta T(t) + \left(\frac{\partial S}{\partial \rho}\right)\Delta\rho(t)\right] \tag{2.17}$$

2.1.3 Wide-Angle X-ray Scattering

Wide-Angle X-ray Scattering (WAXS) is a powerful technique employed to investigate the structural organization of materials exhibiting short-range to intermediate-range ordering and semi-crystalline materials. By measuring the scattering signals at relatively large angles, WAXS provides information corresponding to interatomic distances and in time-resolved case, to their changes in the sub-angstrom range, making it suitable for investigating both large and small scale structures.

To probe the structural evolution in photoexcited bimetallic transition metal complexes, WAXS measurements were performed and analyzed using the methodology presented above. The WAXS experiments were performed at FXE beamline situated at European XFEL facility and ID09 beamline at ESRF. The experimental setup and the collected-large data analysis process are briefly explained in the Section 3.2 and 6.

2.2 X-ray Absorption Spectroscopy

X-ray Absorption Spectroscopy (XAS) involves the measurement of X-ray absorption as a function of the incident photon energy, E. When an X-ray beam of initial intensity, I_0, traverses a material of thickness x, the transmitted intensity decreases according to the material's intrinsic absorption properties and the path length of the irradiated medium.

The absorption process follows the differential equation:

$$\frac{dI}{I} = -\mu(E)dx \tag{2.18}$$

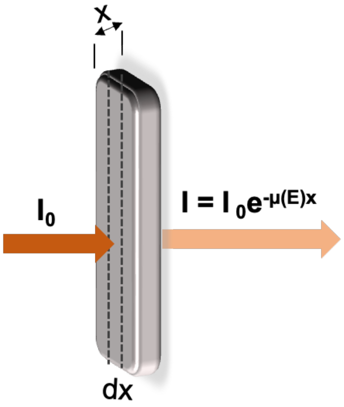

Figure 2.2: Schematic representation for the setup of X-ray Absorption Spectroscopy.

By integrating both sides with the limits for the intensity ranging from I_0 to I_t and the path length ranging from 0 to x, we obtain:

$$I_t = I_0 e^{-\mu(E)x} \tag{2.19}$$

where: I_t represents the transmitted intensity, I_0 is the incident intensity, $\mu(E)$ is the energy-dependent linear absorption coefficient, x is the material's path length.

This equation encapsulates the exponential decay of the X-ray intensity as it propagates through a medium, directly relating the transmitted intensity to the absorption characteristics of the material and the thickness of the sample.

2.2.1 X-ray Absorption Fine Structure

The physical description of the quantum mechanical X-ray Absorption Fine Structure process is related to the photoelectric effect [83]. When the X-ray radiation is absorbed by an atomic core level with a specific binding energy, a photo-electron with wave number k is created and propagates away from the absorbed atom. However the probability of X-ray absorption from a specific core-level is fundamentally determined by the availability of suitable final states for the emitted photoelectron. For successful absorption to occur, there must exist a quantum state that not only matches the exact energy of the photoelectron but also satisfies the angular momentum selection rules. In the absence of such an accessible state, transitions from that core level are forbidden, and consequently, no absorption is observed [83]. Nonetheless, some degree of absorption may still occur due to the excitation of electrons from higher-energy orbitals into unbound continuum states.

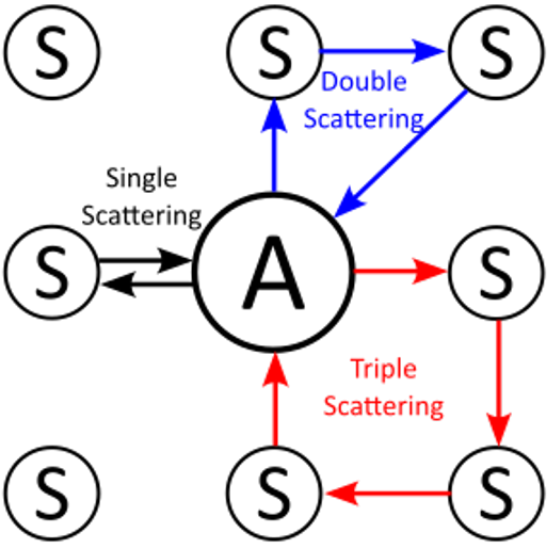

Figure 2.3: Schematic representation of different scattering pathways in X-ray Absorption Spectroscopy, where A = absorbing atom and S = scattering atom.

In presence of a neighboring atom, the photo-electron leaving the absorbing atom does not simply propagate outward, it may undergo elastic scattering by the potential of the neighboring atom. The back-scattered photo-electron can return to the absorbing atom, where it interferes with the outgoing photoelectron wave. This scattering process of the photo-electron's wave is illustrated in Figure 2.3.

The interference modulates the transition probability between the initial core state and the final continuum state. Since the X-ray absorption coefficient is inherently dependent on the availability of unoccupied electronic states with the appropriate energy and angular momentum, the back-scattered photoelectron influences this probability, and can modify the absorption coefficient in an energy-dependent manner. This phenomenon is referred to as the origin of X-ray Absorption Fine Structure (XAFS), illustrated in Figure 2.4 [83].

The wavelength λ of the photoelectron can be calculated by the *deBroglie* equation [84].

$$\lambda = \frac{h}{p} = \frac{h}{m_e v_e} \tag{2.20}$$

where h is Planck's constant, p is the linear momentum of the photoelectron, m_e is the mass of the photoelectron, and v_e is the velocity.

Assuming that the entire energy of the incident X-ray photon is absorbed in the excitation of a single core-level electron, the resulting kinetic energy E_{kin} of the emitted photoelectron can be expressed as the difference between the X-ray photon energy and the binding energy $E_{binding}$ of the electron. This relationship is based on the

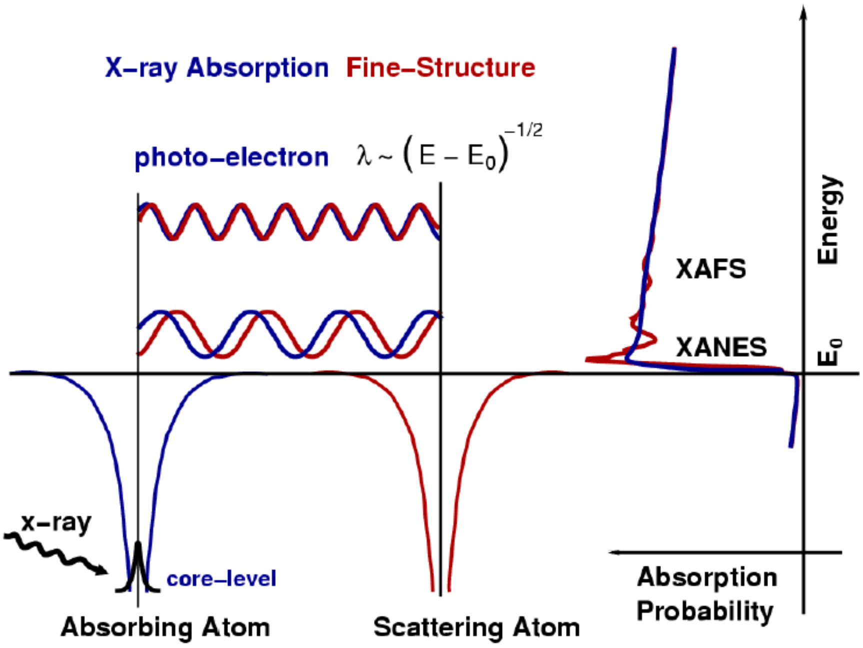

Figure 2.4: Schematic illustration of the X-ray Absorption Fine Structure (XAFS) process. Upon absorption of an X-ray photon, a core electron is excited, generating a photoelectron wave that scatters off neighboring atoms, producing interference patterns sensitive to local structure.

conservation of energy and is given by [85]:

$$E_{\text{kin}} = \frac{p^2}{2m_e} = h\omega - E_0 \tag{2.21}$$

Where, $h\omega$ represents the energy of the incident X-ray photon, with angular frequency of ω. E_0 denotes the binding energy of the core electron (also referred to as the edge energy). As mentioned earlier, if the incident X-ray energy is larger than the binding energy of a core-level electron, then the electron gets excited to the continuum with a sharp rise in the absorption spectrum and the absorption coefficient of XAFS originates from the quantum mechanical interference between the outgoing photoelectron wave and the back scattered waves resulting from interactions with neighboring atoms. Thus the total amplitude of the electron wave function can be reduced or enhanced depending on the phases of the outgoing and back-scattered waves [86]. This interference pattern has the important role in shaping the oscillatory features observed in the XAFS spectrum. When the two waves are in phase, they interfere constructively, resulting in a local maximum in the spectrum. Conversely, destructive interference occurs when the waves are out of phase, producing a minimum in the spectrum.

As the photoelectron energy varies due to changes in the incident photon energy, the wavelength of the photoelectron changes as well, in accordance with its kinetic energy described in equation 2.20. This variation in wavelength alters the relative phase between the outgoing and back-scattered waves. This wavelength related phase difference is influenced by the interatomic distance (R) between the absorbing atom and the neighboring backscatterer.

The amplitude of the backscattered photoelectron wave is strongly dependent on the type of the backscatterer especially on the atomic number and electronic structure. Heavier atoms with higher atomic numbers generally produce stronger backscattering due to their larger electron density and stronger scattering potential. Thus the modulation observed in the XAFS spectrum is a direct consequence of the wave-like nature of the photoelectron, where constructive and destructive interference patterns encode detailed information about the atoms surrounding the absorber. The XAFS spectrum is broadly divided into two spectral regions: X-ray Absorption Near Edge Structure (XANES), defined as the region within approximately ±30 eV of the absorption edge, and Extended X-ray Absorption Fine Structure (EXAFS), which spans the higher-energy region extending beyond 30–50 eV above the edge, an example XAFS spectra shown in Figure 2.5. Although this separation is not strictly defined, both the XANES and EXAFS arise from the wave nature of the emitted photoelectron and the scattering of the wavepacket by the neighboring atoms [85].

An essential aspect of interpreting XAFS spectrum lies in the concept of scattering paths, which represent the possible trajectories by the photoelectron wave as it is emitted

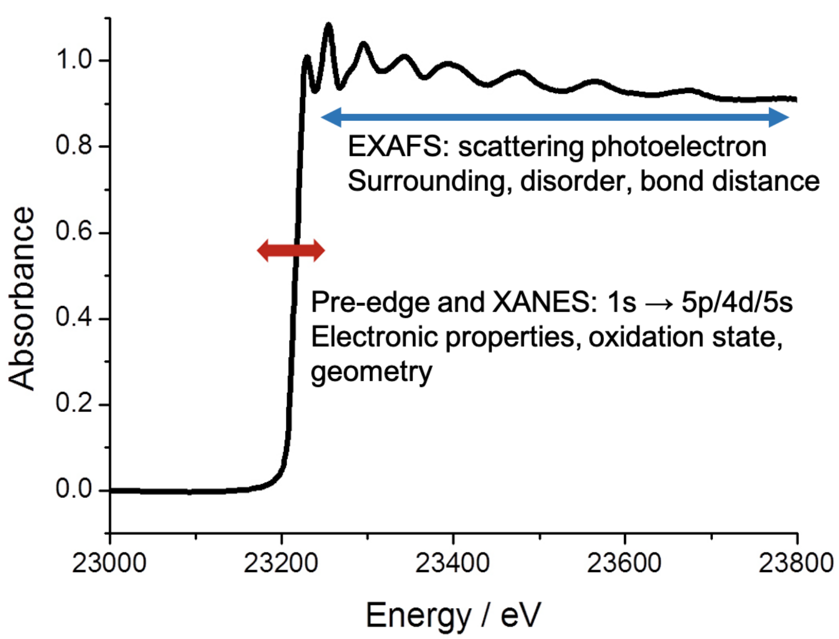

Figure 2.5: Schematic representation of the X-ray Absorption signal, including X-ray Absorption Near Edge Structure (XANES) and Extended X-ray Absorption Fine Structure (EXAFS).

from the absorbing atom followed by the scattering interactions with neighboring atoms, and subsequently returns to the absorber atom. These paths can be classified as either single scattering (SS) or multiple scattering (MS), depending on the number of atomic interactions involved in the scattering. At high energies in the EXAFS region, the photoelectron has a shorter de Broglie wavelength and a reduced mean free path [87]. Thus single scattering are the dominating factor in the EXAFS region and provide the information regarding the local structural environment, including coordination numbers, interatomic distances, and disorder parameters [88]. In contrast, at low energies in the XANES region the photoelectron has much longer wavelength and larger mean free path than in the EXAFS region [86]. This allows the photoelectron to interact with multiple atoms before returning to the absorber atom, resulting in the dominance of multiple scattering processes and providing information of electronic structure, oxidation state, and bond angles within the absorber's coordination environment [83, 89].

In the investigation of Au-dimer complexes reported here, the EXAFS spectra predominantly featured contributions from single scattering (SS) paths, which were acquired experimentally during the synchrotron-based measurements and subsequently analyzed. A detailed theoretical discussion of EXAFS with the analytical procedure and resulting structural insights will be presented in the following sections.

2.2.2 EXAFS

Extended X-ray absorption fine structure (EXAFS) is the oscillatory part of the X-ray absorption spectrum typically extending from approximately 30 eV above the absorption edge and ranging up to 800 eV [85, 90]. These oscillatory features arise due to the interference between the outgoing photoelectron wave emitted when an X-ray photon is absorbed by a core-level electron and the waves back-scattered from surrounding atoms. By analyzing this oscillations in the X-ray absorption spectrum, EXAFS provides valuable insights of the local atomic structure including the electronic and vibrational fingerprints around the absorbing atom. EXAFS encodes critical information about the determination of interatomic distances, coordination numbers, and structural disorder, being quantified by the Debye-Waller factor. This renders EXAFS a versatile technique applicable to a broad spectrum of scientific disciplines including chemistry, biology, geophysics, catalysis research, materials science, and solid-state physics. Despite its broad applicability, the extraction of meaningful structural data from EXAFS spectra is intrinsically non-trivial.

As discussed in the previous section, with increasing energy the SS dominates the scattering process and for the energies above 50 eV, the MS effects are weak enough to be neglected, if just nearest-neighbor structural information has to be extracted. However, for more accurate calculations, it is important to include MS effects into the calculation to consider longer distance contributions to signals from the first coordination shell [88].

For a given X-ray absorption spectrum photon energy E, where the absorption coefficient $\mu(E)$ is measured, the EXAFS spectrum $\chi(E)$ is defined as

$$\chi(E) = \frac{\mu(E) - \mu_0(E)}{\Delta\mu_0} \tag{2.22}$$

where, $\mu_0(E)$ is a smooth background absorption coefficient which represents the absorption of an isolated atom, and $\Delta\mu_0$ is the (measured) absorption jump at the threshold energy E_0 [83, 87].

The oscillatory component of the EXAFS spectrum, $\chi(k)$, usually expressed as a function of the photoelectron wavenumber k, can be derived as [91]

$$k = \sqrt{\frac{2m_e(E - E_0)}{\hbar^2}} \tag{2.23}$$

where m_e is the electron mass, and $\hbar$ is the reduced Planck's constant. The EXAFS oscillatory component typically exhibits relatively low amplitudes, particularly at higher k-values (as illustrated the EXAFS region in Figure 2.5).

To enhance the visibility of these oscillations and to improve the signal-to-noise ratio in the higher-k region, it is a usual practice to apply a weighting factor of k^n, where $n = 1, 2$, or 3, depending on the specific analysis. The classical EXAFS equation can be defined by the following equation [88, 92]

$$\chi(k) = S_0^2 \sum_j \frac{N_j e^{-2\sigma_j^2 k^2} e^{-2R_j/\lambda(k)} f_j(k)}{kR_j^2} \sin(2kR_j + 2\delta_c + \Phi) \tag{2.24}$$

where j represents the coordination shell of identical atoms and the other parameters in the equation are:

- N_j: Coordination number (number of equivalent scatterers) of the j-th shell of neighboring atoms.
- S_0^2: Amplitude reduction term.
- R_j: Distance between the absorber and the backscatterer (interatomic distances).
- $f_j(k)$: Scattering amplitude of the neighboring atom (backscattering amplitude).
- σ_j^2 : Debye-Waller factor, accounting for the temperature dependent root-mean-square fluctuation in bond length along with structural disorder.
- $\lambda(k)$: Energy dependent mean free path of the photoelectron.
- δ_c : Central atom partial wave phase shift of the final state.
- Φ : Additional phase shift which presents the wavelike nature of the backscattering photoelectron.

There are a few significant physical conclusions about EXAFS from the above equation 2.24. Firstly, EXAFS inherently functions as a local structural probe due to the presence of mean free path $\lambda(k)$ and the inverse square distance dependence term R^{-2}. Additionally, the exponential damping term $e^{-2\sigma_j^2 k^2}$, referred as the Debye-Waller factor, accounts for the attenuation of the EXAFS signal due to both thermal vibrations of atoms about their equilibrium positions and static structural disorder in the local atomic environment [87]. With increasing energy, the effect of the Debye-Waller factor increases and when the photoelectron wavenumber approaches a magnitude of approximately $k \approx \frac{1}{\sigma}$ (typically corresponds to around 10 Å^{-1}), the EXAFS signal becomes significantly damped. As a consequence, this imposes a practical limit on the structural sensitivity of EXAFS, and its sensitivity is typically limited to a spatial range of approximately 5 Å from the absorbing atom [86]. Secondly, the $sin(2kR)$ term represents the EXAFS oscillatory part which consists of different frequency components associated with different interatomic distances corresponding to each coordination shells. This frequency-based structure motivates the use of Fourier transforms in the analysis of EXAFS spectrum to determine the interatomic distances, R_j between the absorber atom and the surrounding coordination shells [92]. In addition, the amplitude reduction factor S_0^2 is introduced in the equation 2.24 to account for many-body effects which also includes MS effects, specifically the relaxation of the remaining core electrons (excluding the excited photoelectron) into the core-hole created during the X-ray absorption process [87]. This amplitude reduction term S_0^2 is typically treated as a constant, with values commonly in the range $0.7 < S_0^2 < 1$. The $e^{-2R_j/\lambda(k)}$ term represents the decay of the photoelectron wave. The mean free path $\lambda(k)$ is typically in the range of 5 to 30 Å, and exhibits a significant dependence on the photoelectron wavenumber k [83]. Finally, in order to accurately extract the structural parameters such as interatomic distances and coordination numbers, it is crucial to use the accurate values of the scattering amplitude $f(k)$ and the phase shifts $\delta(k)$, where both of them are dependent on the photoelectron energy and the nature of the scattering atoms.

Therefore, the equation 2.24, provides all the key parameters essential to fit the local atomic structure around the absorbing atom and provides the information about the interatomic distances, coordination numbers, and disorder parameters of the EXAFS data collected for a complex.

To perform a quantitative analysis of EXAFS spectra, $f(k)$ and $\delta(k)$ are typically determined by using various softwares such as *FEFF* [91,93]. FEFF 9.0 is a computer program for ab initio multiple scattering code widely employed for the calculation of X-ray Absorption Spectroscopy (XAS) spectra, including both EXAFS and XANES regions [87]. Similarly, ORCA is an ab initio quantum chemistry software package, extensively used for simulating the pre-edge region in the XAS spectra, as well as constructing molecular structures, simulating X-ray Emission Spectroscopy (XES) and UV-vis spectra of atoms and molecules [94,95]. There are several other computational tools exist such as Gaussian [96], ADF (Amsterdam Density Functional) [97], MXAN [98,99], and Quantum ESPRESSO [100,101]. However, this thesis primarily utilizes FEFF for EXAFS simulations and ORCA to generate and optimize the molecular geometries of the molecular systems. Therefore, only FEFF and ORCA are discussed in detail in the subsequent sections.

FEFF

In the analysis of EXAFS spectrum in this thesis, the calculation was performed using Free Energy Force Field (FEFF) with the FEFF 6.0 version [102]. FEFF 6.0 is an advanced ab initio computational code where the name originates from the spherical wave backscattering amplitude $f_{\text{eff}}(k, r)$ in the XAFS equation. The software is based on a self-consistent multiple scattering Green's function formalism, which accounts for core-hole interactions, inelastic losses, polarization dependence, vibrational damping, and local field corrections. All these effects are calculated through the use of a real-space, all-electron, relativistic Green's function approach with no symmetry constraints, and relying on the self-consistently derived spherical muffin-tin scattering potentials [89]. The Green's function can be calculated in two primary ways. The first way uses the multiple scattering path expansion based on the Rehr-Albers multiple scattering formalism [103]. This method allows for the explicit enumeration and summation of finite scattering paths. Hence, it is computationally efficient and appropriate for extended energy regions above the edge (i. e. EXAFS region). In the other method, FEFF executes a full multiple scattering (FMS) calculation for a cluster of atoms centered around the absorbing atom [91, 104]. This FMS approach is computationally more intensive and scales with the cluster size, but it is crucial for accurately modeling near-edge structure [102]. Hence, mostly used for the XANES region, where the photoelectron has lower kinetic energy and undergoes more complex multiple scattering processes. FEFF includes both inelastic losses and vibrational effects using the GW self-energy and correlated Debye-Waller factors. It provides a wide range of spectroscopic properties, including local density of states (LDOS), scattering amplitudes, and phase shifts [105]. These parameters are critical inputs for modern EXAFS analysis software such as Artemis (description in section 5.1) [106, 107]. The FEFF program is controlled by a set of user-defined input cards and can be typically set in the input file by feff.inp. More details of FEFF are described in the FEFF manual [108].

The feff.inp file used for the analysis of $[Au_2(dcpm)_2](PF_6)_2$ complex is included in the Appendix A.

2.3 Theoretical calculation: Simulations

To complement the experimental results of the bimetallic complexes on the structural dynamics, density functional theory (DFT) calculations [109] were performed using the ORCA 6.0 quantum chemistry software package [110, 111]. The simulation for the potential ground-state and excited state structures of the bimetallic complexes were performed by Dr. Dmitry Khakhulin. The geometry optimizations were carried out in the liquid phase to account for the effects of the solvent molecules, as the experiments are performed in solution as the most relevant condition for molecules under study. Such simulations allow to improve initial structural models and even create structural trajectories for experiment-based refinement of molecular geometries in the ground and excited states.

ORCA

ORCA is an ab initio software package that employs Density Functional Theory (DFT) within a semi-empirical self-consistent field (SCF) molecular orbital framework. In addition to geometry optimizations, ORCA is also capable of computing electronic excitation spectra, including X-ray absorption (XAS) and X-ray emission spectra (XES) [94]. In this work, ORCA was employed to optimize the ground and excited state molecular structures using DFT for the bimetallic Au complexes at the PBE0/def2-TZVP level of theory as well as for scanning the structural parameters such as Au-Au distance while relaxing the remaining molecular structure by computation. The optimized ground-state geometries obtained from ORCA served as reliable structural models for the interpretation of EXAFS experimental data while the ES structures and their respective Au-Au distance-dependent trajectories were used to fit the TR-WAXS data and extract the refined structure. This approach ensured enhanced structural information and consistency with the local atomic environment around the absorbing atom, "locking" the ground state, while the excited state is refined from the time-resolved scattering results.

All geometry optimizations were performed in ORCA using the Conductor-like Polarizable Continuum Model (CPCM) to account for solvation effects [112]. As the metal–dimer complexes studied in this thesis were measured in solution, incorporating CPCM was therefore essential to ensure consistency between the theoretical predictions and the experimental spectroscopic observations.

A series of molecular geometry structures were generated by systematically varying the metal–metal (e. g. Au-Au) distances over a defined range. For each structure, the coordination environment including all the remaining atomic positions in the ligands, was adjusted to maintain realistic molecular conformations and to reflect steric and electronic effects. This was done to simulate potential structural variations and to assess their influence on EXAFS and WAXS signals (in GS and ES respectively). These model geometry structures were further used as the input geometries for theoretical EXAFS simulations (details in Chapter 5.1) and to compare with experimentally derived bond lengths and coordination numbers.

2.3.1 Classical Molecular Dynamics

In solution phase the structure of solvation shells around the solute is defined by mechanical, electrostatic and quantum-chemical interactions between the solvent and solute molecules. As the solute is promoted to an excited state, the solvent molecules in the nearest solvation shells rearrange to accommodate the new electronic and structural configuration of the solute giving rise to the solute-solvent cross-term (cage term) in the difference X-ray scattering signals (as shown in Equation 2.13). The magnitude, length scales and thus the relevant q-range depends on the specific case. For metal dimers, the cage term is typically only a small contribution to the total difference signals and therefore was not explicitly included in the structural refinement here. However, it is important to estimate the potential strength of the effect and its relevant q-range in terms of difference scattering. We therefore performed classical Molecular Dynamics simulations in acetonitrile solvent using the optimized GS and ES structures of the $[Au_2(dcpm)_2](PF_6)_2$ dimer that were fixed during the MD simulation runs. The classical MD simulations were performed for this work and explained briefly in Section 7.1.

Chapter 3

X-ray experiments at large scale facilities

Following the background discussions in Chapter 2 regarding the X-ray scattering and absorption techniques, this Chapter is dedicated to the instrumentation of experimental setups used for the study of ultra-fast dynamics upon the optical excitation of bimetallic complexes. The two different types of X-ray sources were used in this investigation, mainly differing in the X-ray pulse intensity and duration, consequently in the accessible timescales. The Synchrotron-based X-ray sources typically deliver X-ray pulses with durations on the order of 100 picoseconds, restricting their ability in resolving ultrafast dynamics on sub-100ps timescales. In contrast, X-ray Free-Electron Lasers (XFELs) are capable of producing ultrashort pulses with durations reaching down to below 100 fs, allowing access to the femtosecond timescale dynamics involved in primary photochemical processes.

Here the first section starts with a brief introduction of synchrotron radiation and relevant instrumentation, particularly the Petra III P64 beamline and ID09 beamline at ESRF, followed by the X-ray Free Electron Laser (XFEL) description and FXE beamline at European XFEL research facility. In the next section, the experimental methodology will be explained with the basic aspects of XAS experiment and the relevant X-ray detectors. The last sections of this chapter includes details of the liquid jet setup used for the experimental measurements.

3.1 Synchrotron radiation

The elemental principles underlying the generation and control of synchrotron radiation are deeply rooted in classical electrodynamics. The beam dynamics and design of various components constituting the particle accelerators were established through the foundational contributions of James Clerk Maxwell [113], Hendrik Antoon Lorentz [114], and Albert Einstein [115]. These prominent scientists pioneered the concepts and the physical understanding of electromagnetic wave propagation, relativistic effects, and radiation phenomena, required to build and operate these modern particle accelerators and synchrotron light sources.

The third generation Synchrotron radiation (SR) sources started operation in the early 1990s and as of today, represent a dozen or more large-scale facilities worldwide. In total, more than 70 synchrotron radiation research facilities are currently in operation or under construction globally, serving interdisciplinary areas of science. These include, but are not limited to, condensed matter and atomic physics, chemistry, biology, materials science, medical imaging, and various industrial applications [116]. Decades of continuous development have made synchrotron sources the main providers of reliable and stable X-ray radiation, which are crucial for advanced investigations across many disciplines, including physical chemistry. For our studies on metal-dimer complexes, PETRA III and ESRF synchrotrons were used as explained briefly in the following sections. PETRA III (Positron-Electron Tandem Ring Accelerator) is a state-of-the-art third-generation synchrotron radiation source located in Hamburg, Germany, and is operated as part of the Deutsches Elektronen-Synchrotron (DESY) research facility. The European Synchrotron Radiation Facility (ESRF), based in Grenoble, France, operates the largest electron synchrotron in Europe.

Modern synchrotron radiation facilities are based on large-scale electron accelerators that generate relativistic electrons. When these electrons are deflected through magnetic insertion devices such as undulators or wigglers, they emit intense, highly collimated, and tunable X-ray beams. These facilities are consist of a closed-loop storage rings filled with bunches of circulating electrons (or positrons) which are kept at constant energies typically in the range of several GeVs. The overall design of a synchrotron contains several major components including an electron gun, a linear accelerator (known as LINAC), a booster ring, the storage ring, several beamlines, and lastly the experimental end stations. The electron gun provides the initial electron bunches, which may be produced either via thermionic emission from a heated cathode or by photoemission from a photocathode using a laser pulse.

These emitted electrons are then accelerated in the LINAC to energies of several hundreds of MeV, after which they are injected into the booster ring. Inside the booster ring, the energies of the electrons are further increased to the operational energy required for continuous circulation in the storage ring. Once the accelerated electrons are injected into the storage ring, the high-energy electrons (in several GeVs) are circulated within the ring for up to 8 hours, depending on the operation mode of the particular synchrotron [117]. The storage ring contains a series of magnetic structures which are responsible for the generation of synchrotron radiation, these are either bending magnets or insertion devices such as wigglers and undulators. The bending magnets produce uniform magnetic fields to force the electrons into a curved trajectory, resulting the broad-spectrum radiation emitted tangentially to the electron path. In first generation synchrotrons, due to these bending magnets, the synchrotron radiation (SR) was only emitted in a large angle in the plane of the ring, also known as parasitic effect. Till date even in second and third generation of synchrotrons, the bending magnets are often used as the source of X-rays since it is always present due to electrons orbiting in the ring. However, the modern synchrotron radiation facilities mostly use the insertion devices in the storage rings. Both wigglers and undulators are composed of a series of magnets with alternating polarities, assembled after each other and separated by narrow gaps. As electrons passes through these alternating magnetic fields, the electrons oscillate in a sine curve due to the Lorentz force and result the electron to radiate the SR along the axial direction. A schematic overview of a synchrotron radiation source is illustrated in the Figure 3.1.

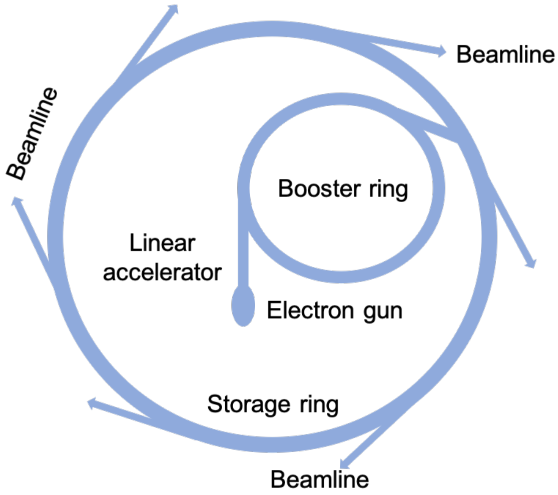

Figure 3.1: Scheme of a third-generation Synchrotron Light Source Facility.

The characteristics of this emitted radiation are strongly influenced by the dimensionless deflection parameter, K:

$$K = \frac{eB_0L}{2\pi m_e c} \approx 0.934LB_0 \tag{3.1}$$

where e is the the charge and m_e is mass of the electron, B_0 is the magnetic field strength, L is the undulator period, and c is the speed of light [79]. When $K \gg 1$, the insertion device operates in the wiggler regime and the electron deflections become significantly large and emit incoherent X-rays over a broader spectral range with N times higher intensity from successive oscillations [118]. In contrast, when $K \ll 1$, the insertion device operates in the undulator regime and the angular deflection of the electron beam remains smaller than the angular divergence of the emitted X-rays. In this case, the emitted coherent radiation from successive oscillations interferes constructively which results N^2 times higher intensity and produce intense, narrow-bandwidth, quasi-monochromatic X-ray beams. This fundamental distinction in the emitted radiation properties makes undulators preferable for the experiments requiring high brilliance and energy resolution, while wigglers are used when high flux over a wide spectral range is desired [119]. These *Brilliance* (also referred as spectral brightness) is represented as

$$Brilliance = \frac{Number\ of\ photons/second}{(mm^2) \cdot (mrad^2) \cdot (0.1\%\, BW)} \tag{3.2}$$

where *Number of photons/second* is the photon flux within a given spectral bandwidth, mm^2 is the source size (spatial distribution), $mrad^2$ is the vertical and horizontal angular divergence, and and $0.1\%BW$ refers to the relative spectral bandwidth, with the brilliance usually normalized to a relative bandwidth of 0.1%. This *Brilliance* is used to compare the different X-ray sources. Typically undulator-based synchrotron beamlines achieve *Brilliance* values several orders of magnitude higher than bending magnet sources.

Upon emission of SR, the electrons lose a fraction of their energy, which is compensated by the radio frequency (RF) cavity integrated into the synchrotron. The RF cavity generates an oscillating electromagnetic field with a phase-stable electric potential that supports the formation of "buckets" within which the electron bunches can be captured and confined. These buckets propagate synchronously around the storage ring. The revolution frequency f_{rev} of electrons circulating in the storage ring at nearly the speed of light is determined by the circumference of the storage ring, $l_{circumf}$. For PETRA III, the storage ring has a circumference of 2304 meters, this yields the revolution frequency of

$$f_{\text{rev}} = \frac{c}{l_{circumf}} \approx 130\,\text{kHz} \tag{3.3}$$

When the fundamental radio cavity frequency, f_{RF} is 500 MHz, then total number of buckets is given by

$$N = \frac{f_{RF}}{f_{rev}} = 3840 \tag{3.4}$$

A bucket can be populated with a bunch of electrons, in various bunch filling modes according to the different experimental requirements. At PETRA III, typical bunch operating modes include 40, 60, 240, or 960 buckets with bunch separations of 192 ns, 128 ns and 8 ns, respectively.

3.1.1 P64 beamline

The P64 beamline is situated at the high brilliance storage ring of PETRA III at DESY and specifically designed to support the advanced x-ray absorption spectroscopy (XAS) experiments which require high photon flux and energy stability. This beamline is well-suited for time-resolved studies such as quick extended X-ray absorption fine structure (EXAFS) spectroscopy and X-ray Absorption Near Edge Structure (XANES) on sub-second timescales (100 ms to μs). It is also capable of perfoming Resonant X-Ray Emission Spectroscopy (RXES), High Energy Resolution Fluorescence Detected XAS (HERFD-XAS) and Valence-To-Core X-Ray Emission Spectroscopy (VTC-XES) of highly dilute systems [120].

The radiation source for P64 beamline is a 58-pole undulator with a period of 32.8 mm and total 2-meter-long. This beamline provides a brilliant and tunable X-ray beam [121]. The beamline has two independent cryogenically-cooled (-196°C or -320°F) monochromators: channel-cut monochromator (CCM) (also known as quick EXAFS monochromator) and double-crystal fixed-exit monochromator (DCM). For detailed information of the monochromators, readers are referred to [120, 122]. DCM was employed during the beamtime of metal-dimer complexes which was operated in the continuous scanning mode. This was equipped with a Si(311) crystal pair, making it suitable for high-resolution X-ray absorption spectroscopy for the energy range of 12 keV. The Si(311) monochromator in general operates for the energy range of 4.6–103 keV and suitable for superior energy resolution, in-spite of a lower photon flux compared to Si(111). During the scans, the monochromator ran continuously to enable efficient and time-resolved data acquisition. The liquid nitrogen cooling minimized lattice strain on the crystals, ensuring the energy stability and consistent beam positioning throughout the measurements. A schematic view of the P64 beamline is shown in Figure 3.2, adapted from [123], which was used for the static EXAFS measurement of metal-dimer complexes.

For the static EXAFS measurements, Rhodium (Rh)-coated Si mirrors were employed for reducing the intensity of higher harmonics and focusing the beam. These Si mirrors with 800 mm each in length, are positioned downstream of the monochromator and serve to effectively attenuate the higher-order harmonics to avoid artifacts in the EXAFS-spectra. Among the available three different types of coating, the Rh coating was specifically chosen for the intermediate energy range whereas Pt coating is for the higher and no coating (bare Si) is for the lower energy range. For focusing the beam, the first mirror provided the horizontal focusing by two grooves with different radii in the energy range of 2.4 keV to 22 keV. The bendable second mirror, enabled vertical focusing over the entire energy range.

During the experiment of metal-dimer complexes, the undulator was operated at the third harmonic, resulting a focused beam size of approximately 250 µm (horizontal) × 100 μm (vertical) and a photon flux of $6{\times}10^{11}$ photon/s at 12 keV. For further details, one can refer to the [120, 122]. The incident X-ray beam irradiated the samples in 0.5 mm round liquid jet, exciting the Au atoms and producing characteristic fluorescence around the L_3 absorption edge. This fluorescence signal was either collected with a diode in total fluorescence yield (TFY) mode or dispersed by the von Hamos spectrometer

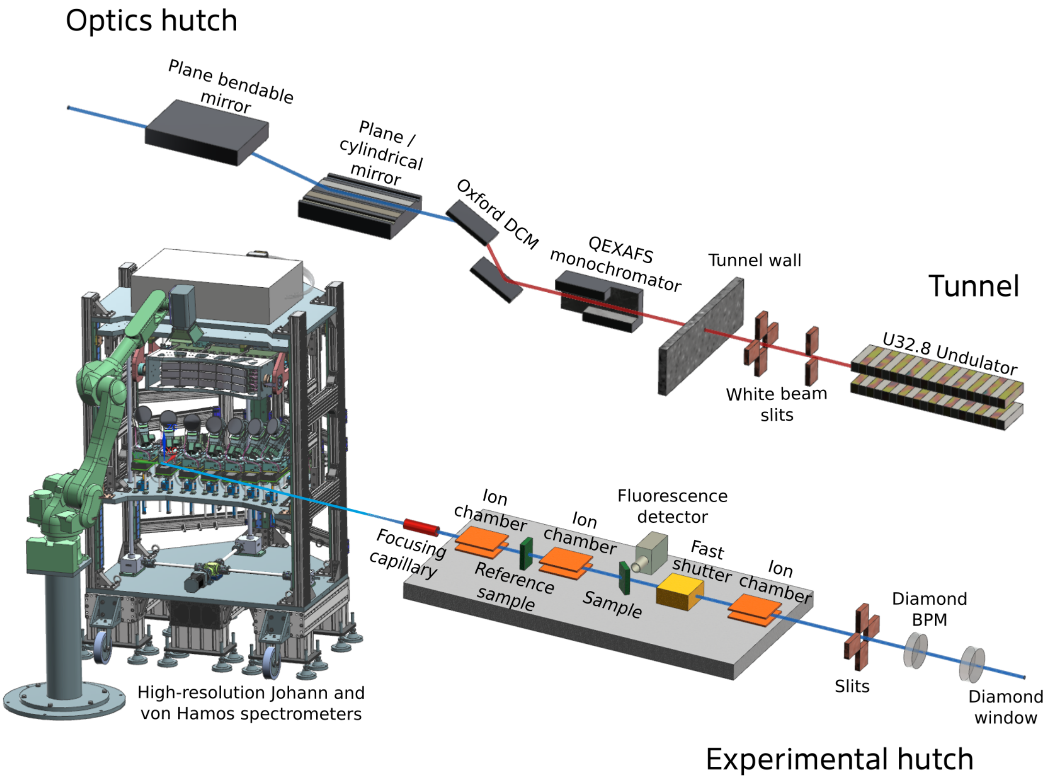

Figure 3.2: Schematics of P64 beamline [123].

to isolate the narrow L_a emission range and subsequently recorded with the avalanche photodiodes, as described in Section 3.5.

3.1.2 ID09 beamline

The ID09 beamline at the ESRF is a long-established and well-recognized end-station dedicated to time-resolved structural dynamics in solution and solids. Over the years, ID09 has hosted a wide range of ultrafast X-ray experiments, and its technical design and beamline components have been thoroughly documented in the literature and their websites, such as [124–126]. Therefore, a detailed description of the general beamline setup is not repeated here; instead, this section focuses specifically on the experimental configuration employed for studying structural dynamics in bimetallic complexes in solution.

For the presented experiments, 100 ps pulse of a pink beam generated from the U17 undulator was employed, providing a high-flux X-ray source well suited to pump–probe wide-angle X-ray scattering (WAXS) studies. The beam energy was tuned in the 18–19 keV range, which enables to cover a broad range of momentum transfer thus accessing to the relevant structural features of the bimetallic complexes. A continuous free-flowing round liquid (capillary) jet was employed as the sample delivery method, providing constant renewal of the probed volume between successive pump–probe cycles, effectively preventing cumulative radiation damage and ensuring experimental reproducibility. The optical excitation was provided by a synchronized Ti:Sapphire femtosecond laser system and two excitation wavelengths were used: 320 nm generated via a tunable TOPAS system with pulse energies of 30–40 μJ per pulse, and 266 nm obtained via third-harmonic generation (THG).

3.2 X-ray Free Electron Laser

In the 1960s, the advent of novel sources of coherent radiation, named masers and, later as lasers – became of a great interest due to their remarkable unique properties of generating radiation with high intensity and coherence [127]. Later in 1971, a revolutionary concept was proposed by John M. J. Madey wherein a beam of free electrons traversing a periodic magnetic structure, known as an undulator, could serve as the gain medium [128]. It was named as the Free Electron Laser (FEL) as the electrons in the undulator were not bound to any atoms or molecules. The first practical implementation of this FEL idea was demonstrated in 1977 [129].

In 1980, A. M. Kondratenko and E. L. Saldin further advanced the concept of FEL by introducing the Self-Amplified Spontaneous Emission (SASE) mechanism. They demonstrated that during this process the initial random field of spontaneous radiation can be amplified in the sufficiently long undulator and could interact with the electron bunch causing micro-bunching and producing a fully coherent radiation output [130]. The length of the these undulators should be typically five to ten times longer than those used in the synchrotron radiation sources [116]. In the 1992, the first proposal was made to build an X-ray FEL (XFEL). In 2005, FLASH, the first XFEL began to operate in the XUV and soft X-ray region. The SASE mechanism eliminated the need for an optical cavity which removed the limitation on the minimum wavelength and enabling the design of FELs capable of producing X-ray radiations. Later in 2009, the first hard X-ray XFEL, LCLS began user operation [131]. Currently around ten XFELs are in operation and among other areas are actively used for investigations on chemical and structural dynamics. For the investigation of metal-dimer complexes, European XFEL was used as described briefly in the following section.

3.2.1 European X-ray Free-Electron Laser facility

The European X-ray Free-Electron Laser (EuXFEL) facility is a user research laboratory operating since 2017 and providing soft and hard X-ray FEL radiation to seven scientific instruments that enables cutting-edge investigations of matter at electronic and structural level and on femtosecond (fs) time scales. The facility spans 3.4 km from the linear accelerator in DESY in Hamburg to the experimental hall in Schenefeld. The European XFEL delivers extremely intense, ultrashort, and transversely coherent X-ray pulses, with each pulse containing more than 10^{12} photons within its typical duration of below 100 fs. The X-ray radiation is produced in high-repetition-rate bursts (or pulse trains), which repeat every 100 ms, corresponding to a burst repetition rate of 10 Hz. Each burst lasts for approximately 600 μs and can contain up to 2700 individual pulses, emitted at an intra-train repetition rate of 4.5 MHz with 222 ns separation between successive pulses. Thus, the facility can deliver up to 27,000 intense and ultrashort X-ray pulses per second, making it one of the most powerful sources for investigations of time-resolved dynamic processes on fs timescales [132]. For better understanding readers can refer to the Figure 3.3.

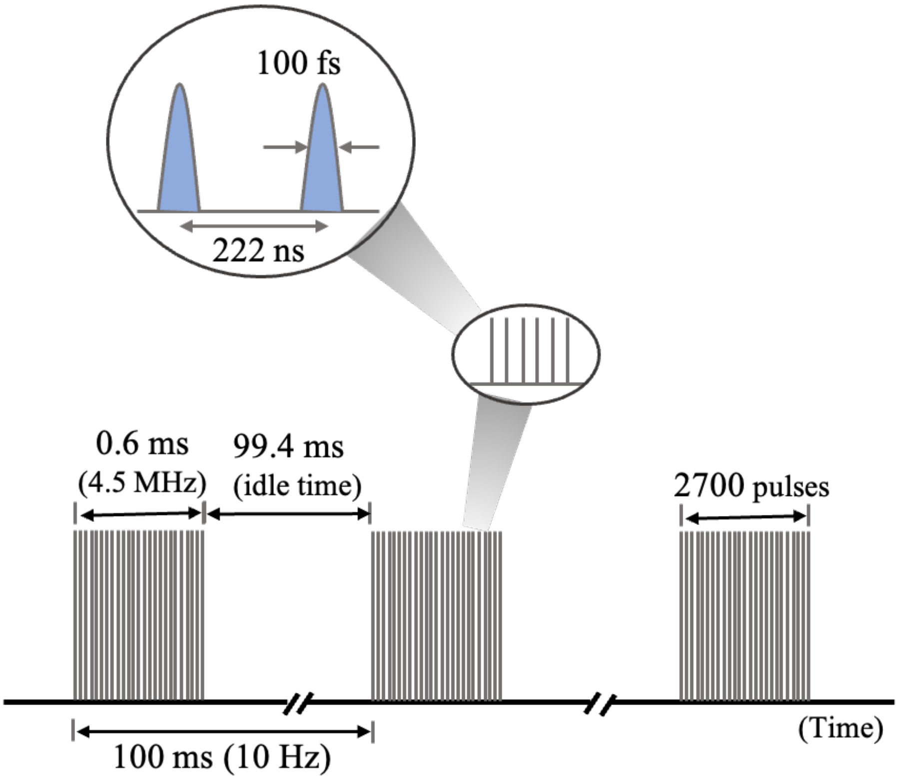

Figure 3.3: Distribution of European XFEL pulses.

The entire European XFEL facility is situated underground, in a 5.2 m diameter tunnel at depth of about 6 to 25 m below the ground surface level [133]. The European XFEL facility consists of three sections where each section plays a critical role in the generation and delivery of high-brilliance X-ray FEL radiation.

The first section includes a photo-injector, a 17.5 GeV superconducting linear accelerator (LINAC) and undulators. The 43 m long photo-injector generates electron bunches (electron cloud) via the photoelectric effect: ultraviolet laser pulses strike a Cs_2Te photocathode, releasing electrons. These emitted electrons are initially accelerated to approximately 6 MeV and then injected into the first superconducting acceleration module. To linearize the longitudinal phase of accelerated electrons, the electrons subsequently pass through a 3.9 GHz super-conducting acceleration module. This module ensures proper shaping of the electron bunches before they are injected into the main LINAC.

The main LINAC accelerator consists of a series of superconducting radio-frequency (SRF) cavities with 96 modules operated at 2.2 K ($-271\,^{\circ}$C). The cavities are made of Niobium (12 m long each module) and operate at 1.3 GHz. In total, the LINAC extends over a length of approximately 1.7 km. This setup accelerate the electron bunches to near-light speed and to the final energy of up to 17.5 GeV with high beam quality, low emittance, and minimal energy spread—parameters essential for efficient FEL gain in the subsequent undulator sections [132].

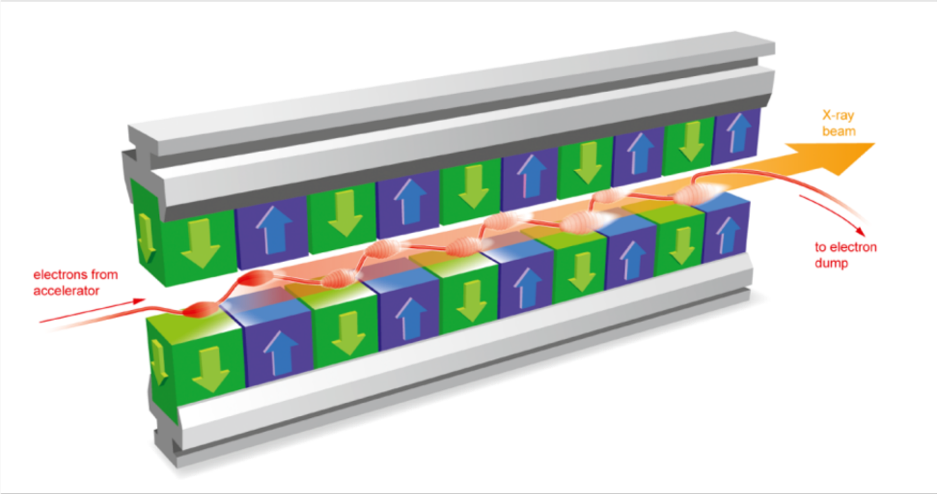

Figure 3.4: Schematic representation of the magnetic undulator at the European XFEL [134].

These high-energy electron bunches are then distributed simultaneously into three dedicated tunnels, each equipped with FEL undulator modules (Figure 3.4, adapted from [134]) where the XFEL radiation is generated via the SASE process, the three tunnels are denoted by SASE1, SASE2 and SASE3. In around 100 meters long undulators, the relativistic electrons pass through periodic arrangements of magnets, causing electrons to take a zig-zag "slalom" course. This process amplifies the radiation intensity as it interacts coherently with the electron bunch itself causing electrons to form smaller bunches (microbunching) according to the generate electric field which results resulting an intense, coherent X-ray pulses with each turn [135]. The SASE1 and SASE2 are optimized for the hard X-ray radiation generation in the energy range of approximately 3 to 25 keV. In contrast, SASE3 is dedicated to soft X-rays generation, operating in a lower energy range of approximately 250 eV to 3 keV. This distribution of SASE lines enables the European XFEL to cover a broad spectral range, making it suitable for a diverse array of applications in structural biology, material science, ultrafast chemistry, and condensed matter physics [132, 133].

The second section includes the photon beam transport system for specific beamline. These systems are dedicated to the transporting, focusing, steering, and monitoring of the generated X-ray FEL beams before they enter the experimental area. Precision X-ray optics, such as grazing incidence mirrors and diagnostic tools, ensure beam stability and alignment. The mirrors are also used to direct the beam toward the scientific instruments positioned downstream of each FEL source.

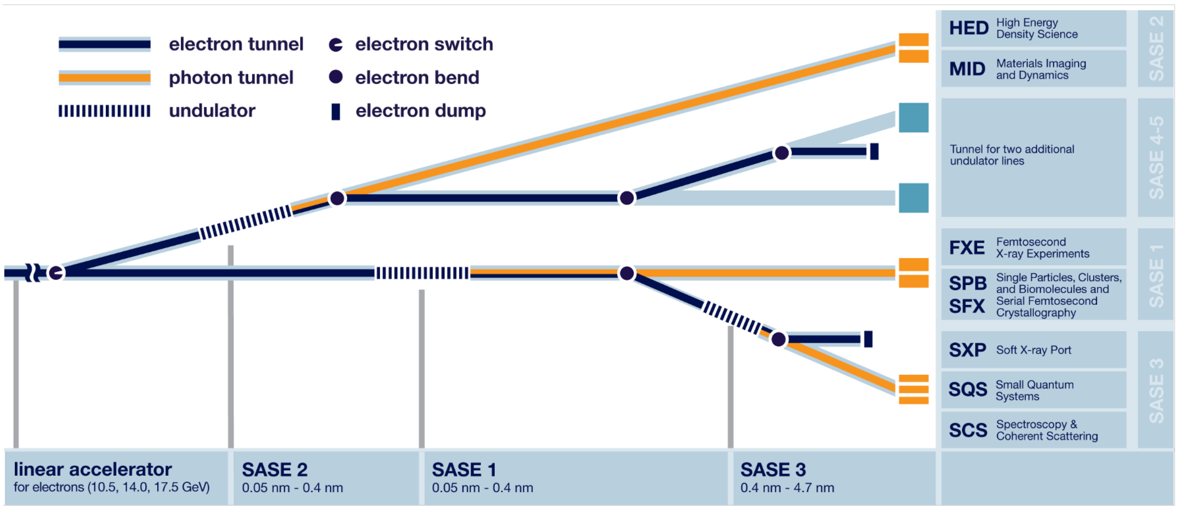

Figure 3.5: Beamline layout of the EuXFEL research facilities with seven operational instruments [134].

The third section is the experimental hall, which extends along the beam direction and accommodates all the scientific instruments and where user experiments are conducted. The beamline layout of the experimental hall with all the instruments are illustrated in the Figure 3.5, taken from [134]. This modular setup allows simultaneous operation of multiple experiments, enhancing the facility's experimental throughput and versatility for a broad range of scientific applications.

In this work, the FXE instrument was employed to investigate bimetallic complexes in solution by means of femtosecond WAXS measurements. The instrument is briefly described in the following section.

3.2.2 FXE beamline

The scientific instrument Femtosecond X-ray Experiment (FXE) is located at the end of the 915 m-long SASE1 FEL beamline, while primarily focusing in the field of photo-induced ultrafast dynamics in condensed phase. The instrument enables ultrafast structural and electronic investigations down to sub-100 fs timescales using different techniques such as ultrafast X-ray Absorption Near Edge Structures (XANES) along with Extended X-ray Absorption Fine Structure (EXAFS), Wide Angle X-ray Scattering (WAXS), Resonant Inelastic X-ray Scattering (RIXS), and non-resonant X-ray Emission Spectroscopy (XES) in the liquid and solid phase. Using different methods FXE instrument is capable of capture the earliest steps of chemical reactions, and ultimately facilitating the creation of molecular movies that reveal both atomic rearrangements and transient electronic structure dynamics.

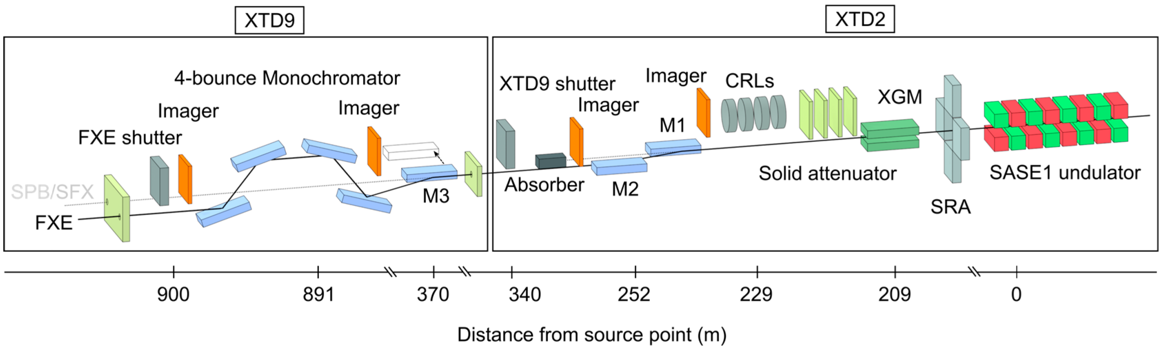

Figure 3.6: Scheme of 900 m long X-ray beamline. The SASE1 undulator exit is in the right side, from where the X-ray beam travels towards the experimental hall on the left side [136].

After the undulator exit, several components are installed for improving the beam quality with better beam size, shape and intensity. Figure 3.6 represents this section of the FXE beamline, taken from [136]. At 230 m downstream from the SASE1 undulator, a ten-element compound refractive lens (CRL) system is installed for beam collimation to a beam size of 1–2 mm. This collimation allows the full beam to transmit efficiently through the subsequent beamline optics, including the three grazing incidence mirrors (M1, M2, and M3), which are responsible for beam steering and focusing. These mirrors allow to optimize transmission and direction of the main part of the available X-ray flux into the FXE experimental hutch, thereby maximizing photon delivery to the sample interaction region [137]. Inside the tunnel a double-channel-cut Si(111) monochromator is installed 10 m upstream of the FXE photon beam tunnel transport wall. With four-bounce geometry, the monochromator preserves the original x-ray beam axis regardless of whether the beam is operated in pink (broadband) or monochromatic mode. In the current research experiment at FXE beamline, pink beam was used to study the bimetallic complexes.

Figure 3.7 illustrates the FXE beamline inside the experimental hutch, taken from [138]. Inside the experimental hutch, the 8-meter-long optics branch (OPT) is dedicated to beam conditioning and focusing via several diagnostics and beam shaping components, including the three beam imaging units (BIUs) for visual imaging of the incoming X-ray beam intensity - made of Ce-doped YAG crystal, single-shot spectrum

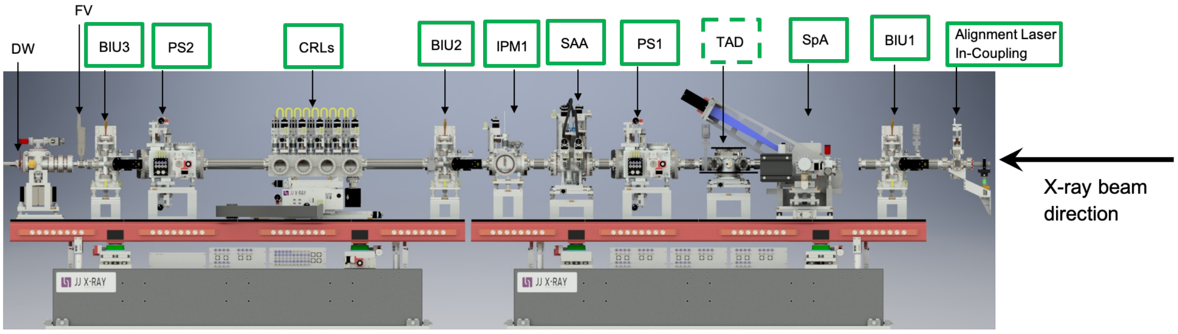

Figure 3.7: Optics section of the FXE instrument hutch with different components used for focusing the beam [138].

analyzer (SpA) to determine the spectrum for every single shot, two water-cooled power slit systems (PS1 and PS2) to withstand the full unattenuated X-ray beam, a solid attenuator assembly (SAA) to attenuate the beam, and a ten-element Be-lens focusing optics (CRLs) for for focusing the beam. The total photon transmission efficiency has been quantitatively evaluated and determined to be $> 70\%$.

To excite transient states in samples, FXE instrument uses a specially developed burst-mode femtosecond laser system, named as the Pump-Probe Laser (PPL) [139]. These initiated transient states in matter are subsequently probed by the synchronized femtosecond X-ray pulses to capture their structural and electronic evolution on fs timescales. The unique burst-mode pulse structure of the EuXFEL is supported by the PPL to enable repetitive pump-probe measurements. The output of PPL is tunable across a broad spectral range in near-IR regions with the possibility of using 50 fs or 15 fs pulses with 800 nm fundamental beam or, alternatively approximately 800 fs long pulses with wavelength of 1030 nm [136, 139]. The 800 nm fundamental radiation can also be converted to generate the second (400 nm) and third (267 nm) harmonics. For additional continuous wavelength tunability, a TOPAS (travelling-wave optical parametric amplifier of superfluorescence) system is installed for selective excitation across a broader spectral range.

In the interaction region, the optical pump and X-ray beams are overlapped in the sample and then the scattered or emitted signals are recorded in the aligned spectrometers and detectors. The two available spectrometers, Johann and von Hamos X-ray emission spectrometers can operate simultaneously. The Johann spectrometer is more suitable for low signal yield experiment, specially with extremely low concentration and for high energy resolution experiments as RIXS or high energy-resolved fluorescence detection (HERFD) measurements. The von Hamos spectrometer is applicable mostly for strong emission signals and for simultaneous acquisition of multiple emission lines from one or several elements, using the single-module Jungfrau 500k detector. For the investigation of bimetallic complexes, the available large pixel detector (LPD) was used

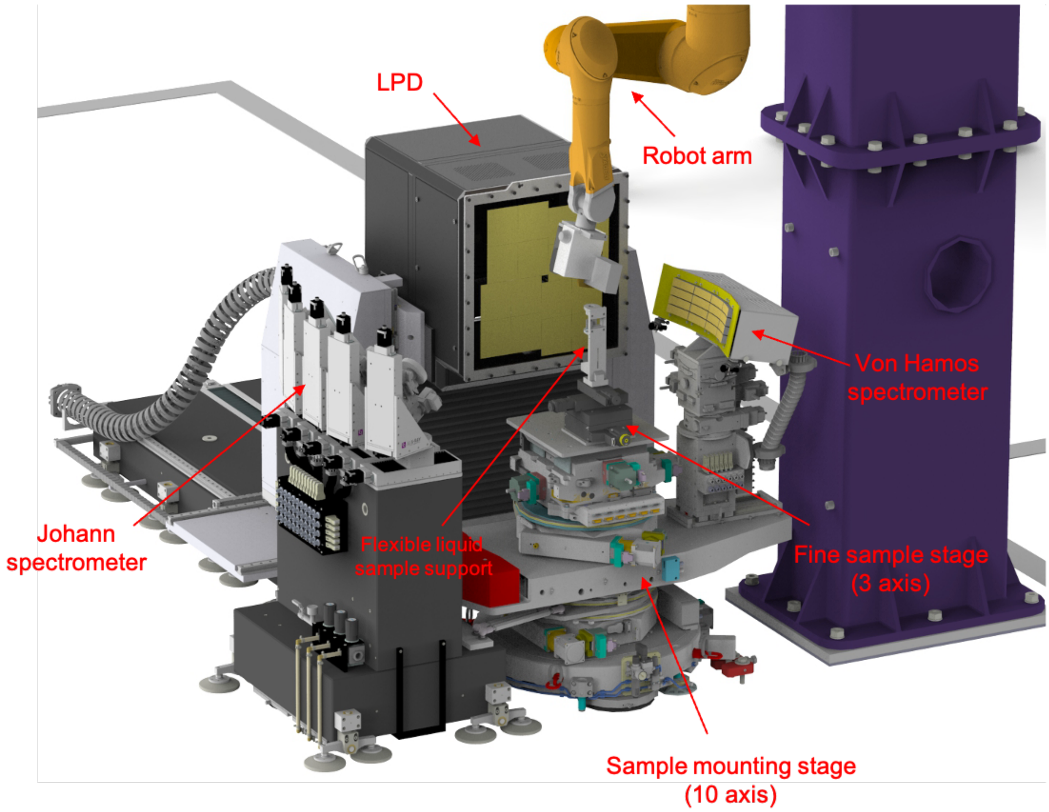

Figure 3.8: FXE instrumental hutch setup for simultaneous X-ray scattering /diffraction and spectroscopy measurements.

for the scattering measurement, for details see Section 3.5.

3.3 Time-resolved Experiments

To capture ultrafast structural and electronic dynamics during chemical reactions and phase transitions, the time-resolved X-ray experiments are required. The focus of the thesis is to study the ultrafast structural changes in the stimuli-responsive transition metal dimer complexes. Therefore, time-resolved measurements were crucial for this project and were performed using optical laser excitation combined with femtosecond and picosecond X-ray probe pulses.

These pump–probe experiments enabled the direct observation of transient states with transient structural changes in the excited states with atomic spatial resolution, thereby allowing a detailed characterization of their structural dynamics. The illustration of a typical setup of pump-probe experiment is shown in Figure 3.9.

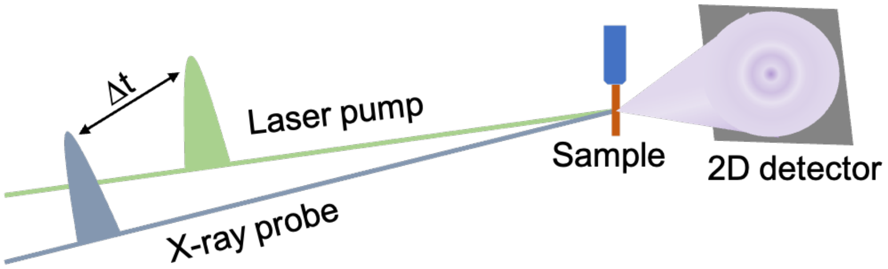

Figure 3.9: Scheme of a typical setup for a time-resolved experiment with a laser pump and X-ray probe. For solution phase study, the liquid jet contains the sample, which runs continuously under high pressure to fulfill the sample renewal between each pump-probe event.

An optical pump pulse (denoted with blue) first photo-excites the sample flowing through the jet and initiates the photochemical process in the sample system of interest. Then after a specified time delay, Δt $= t$ - t_0, where t_0 corresponds to the temporal overlap between pump and probe pulses at the sample position, the X-ray probe-pulse (denoted with red) interacts with the sample and scatters in a unique pattern, which is then collected by the detector. By varying the time delay Δt in each measurement, multiple measurement scans during the photochemical process can be collected, providing an insight of the temporal evolution as forming a ”molecular movie”.

The WAXS experiment for bimetallic Au complexes was performed at the FXE beamline of the European XFEL, where optical pump – X-ray probe measurements were conducted in a burst mode operation synchronized to the EuXFEL pulse structure. The optical excitation was performed using the femtosecond Pump-Probe Laser (PPL) system tuned to specific excitation wavelengths, while the probing X-ray pulses, delivered at a repetition rate of 141 kHz within the pulse train, captured snapshots of the evolving system structure. During the beamtime (proposal number 4507 at EuXFEL) allocated for measurements on bimetallic complexes, the solution was excited by two different spectral wavelengths. Optical pump of 266 nm was used for $[Au_2(dcpm)_2](PF_6)_2$ complex and 266 nm was used for $[Au_2(pnnp)_2]Cl_2$ complexes in acetonitrile solutions, according to the resonant excitations to the relevant excited states. The optical pump pulse at 320 nm was produced by the available TOPAS system and the 266 nm optical pulse was produced by the third harmonic generation of the fundamental laser wavelength. Further details are given in Section 6.

Similarly, during the WAXS beamtime at the ID09 of ESRF, time-resolved measurements were conducted using femtosecond optical excitation. The optical laser system provided pump pulses at 320 nm, generated via a TOPAS, with pulse energies in the range of 30–40 µJ per pulse. Additionally, excitation at 266 nm was generated using third harmonic generation (TH) of the fundamental laser wavelength.

3.4 XAS detection methods

To collect high quality experimental data, it is essential to select an appropriate detection method, which ensures detectors to operate within their linear response range, maintain X-ray beam stability throughout the measurement, and maintain the reproducibility of successive energy scans. There are two possible way to measure the XAS spectrum - either in transmission or or in fluorescence mode (either total, TFY, or partial fluorescence (e.g. by detecting only specific emission line in HERFD mode)) [140, 141].

The transmission detection technique is suitable for relatively thick samples with large absorption contrast. In contrast, the TFY detection technique is applicable to samples of varying with low absorption contrast e.g. dulite solutions . Furthermore, this is more suitable for the low-concentration samples with a low background. For the ground state EXAFS measurements at the P64 beamline of PETRA III, the total fluorescence yield detection method was carried out as the experiments were performed with low-concentration liquid samples.

3.4.1 Transmission mode

In transmission mode, the incident X-ray intensity (I_0) and the transmitted intensity (I) after passing through the sample are measured using ionization chambers or other calibrated detectors. The absorption coefficient, $\mu(E)$ is then determined from the Beer–Lambert law, $\mu(E) = \frac{1}{d} \ln\left(\frac{I_0}{I}\right)$, where d is the thickness of the sample. This direct measurement provides a linear relationship between the transmitted intensity and the absorption coefficient, making transmission mode particularly suitable for quantitative analysis [142, 143].

Transmission detection is advantageous when studying concentrated samples or materials with relatively strong absorption edges, where self-absorption or saturation effects in fluorescence measurements can become significant. However, the absorber concentration and thickness should fall within the optimal range where sufficient X-ray absorption occurs without complete attenuation. For dilute samples, transmission becomes impractical, and alternative detection methods such as fluorescence yield are preferred.

3.4.2 Total fluorescence yield mode

In the TFY mode, the intensity of the incident X-ray beam (I_0) is measured using an ionization chamber, while the emitted (result of core-level excitations) characteristic fluorescence X-ray signal (I_F), is collected by a detector, positioned at 90° respect to the incident beam to minimize elastic scattering contributions.

The absorption coefficient, $\mu(E)$ measured in fluorescence mode is proportional to the ratio of detected fluorescence to incident intensity, i.e., $\mu(E) \propto I_\mathrm{F}/I_0$, within the first-order approximation. This relation enables the indirect extraction of X-ray absorption spectra. In this method, the total integrated fluorescence yield from all decay channels is recorded as a function of the incident photon energy, whereas in the partial fluorescence yield mode a specific emission line is selected for example using crystal analyzers in emission spectrometers. Further theoretical explanations are explained in [141].

3.5 Detectors

For the investigation of metal-dimer complexes, two different types of detectors were utilized for WAXS measurement at different X-ray sources. For the WAXS measurement at FXE beamline, the LPD detector was used. The WAXS measurement at ID09 beamline was performed using the Rayonix MX170-HS detector. On the other hand, for EXAFS measurement at P64 beamline, the Avalanche photodiodes (APDs) were employed. In this section, a brief description of these detectors is presented.

3.5.1 Large Pixel Detector

The Large Pixel Detector (LPD) is a high-speed, hybrid pixel detector developed by the Rutherford Appleton Laboratory (RAL, UK) for unique high-repetition-rate applications at FXE instrument at the European XFEL [144]. The sensitive area of the detector is formed by square pixels of 500 μm × 500 μm size with 1024 × 1024 pixels in total and consists of 256 exchangeable rectangular tiles of 128 × 32 pixels. These tiles are further grouped into supermodules and quadrants. Each pixel is equipped with 512 analog memory cells, enabling the storage of up to 512 full frames each acquired with an integration time of 100 ns. This make the detector capable of taking data with 4.5 MHz frame rate. Then the stored images are transferred to a data acquisition system within the time interval between pulse-trains (100 ms) [137].

The LPD incorporates three parallel gain stages per pixel with gain factors of 1 × (low gain), 10 × (medium gain), and 100 × (high gain), which provide a wide dynamic range up to 10^5 photons at 12 keV. During the experiment with bimetallic complexes, fixed medium gain mode was used in the range 100-1000 at 17 keV. Depending on the photon energy, the system can automatically select the most appropriate gain per pixel in each frame, enhancing dynamic range and sensitivity. It features the 500-µm thick Si sensor which enables the X-ray detection with quantum efficiency of > 90% in the photon energy range of 5–13 keV and approximately 40% detection efficiency at 20 keV [137].

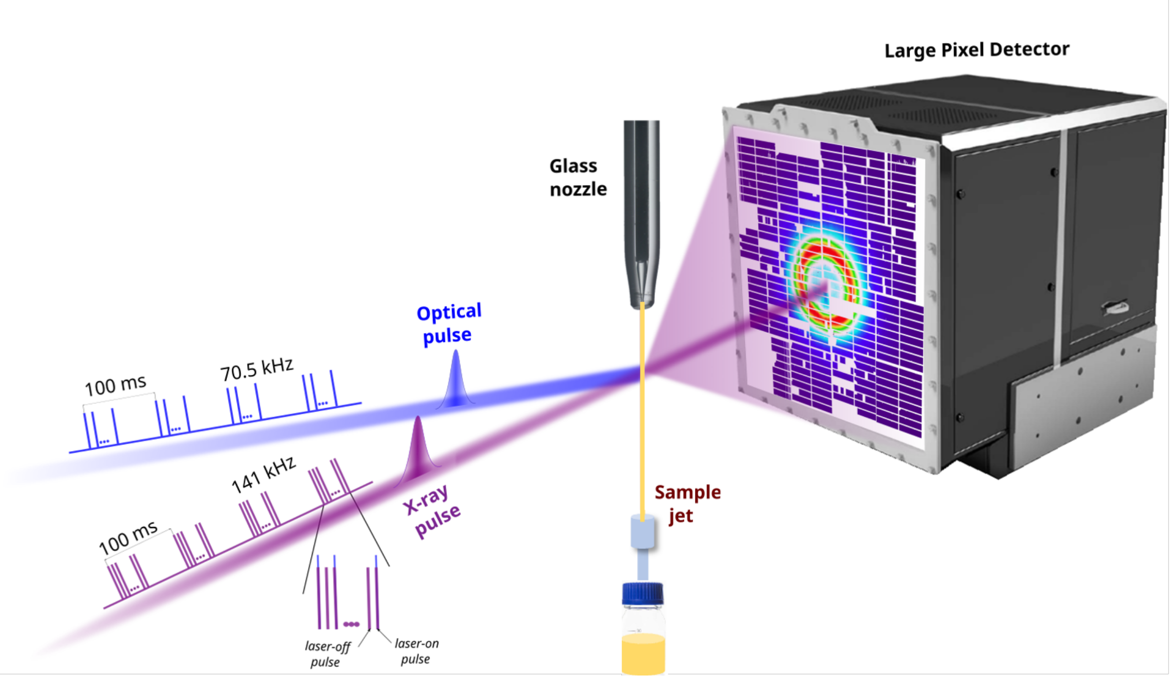

Figure 3.10: Schematic of the WAXS setup available at FXE beamline. The large Pixel Detector was used for the experiment of liquid bi-nuclear Au complexes to detect the X-ray scattering signals.

To optimize data quality, the LPD is equipped with a fast frame “veto” capability that allows selective image acquisition based on external or online diagnostics as well as fixed programmed veto patterns. Each image undergoes per-pixel, per-memory-cell, and per-gain calibration, with correction parameters stored in a comprehensive calibration database totaling 40 GB. These calibrations include offset, gain normalization, and geometrical corrections based on high-resolution photographic metrology.

3.5.2 Rayonix MX170-HS detector

The Rayonix MX170-HS detector at ID09 beamline at ESRF is large-area CCD-based system which provides a broad angular coverage and high dynamic range, enabling simultaneous detection of both intense low-Q solvent responses and comparatively weaker high-Q intramolecular scattering features. The MX170-HS offers sufficient frame-transfer speed and low readout noise to capture high-quality difference scattering signals across the full reciprocal-space range relevant for molecular structure analysis [145, 146].

3.5.3 Avalanche photodiodes

For the EXAFS measurements performed at the P64 beamline, avalanche photodiodes (APDs) were employed as the primary X-ray detectors, owing to their excellent time response, high linearity, and suitability for high-flux synchrotron radiation environments [147]. APDs are solid-state semiconductor detectors operated under high reverse-bias voltage, where the absorption of an X-ray photon generates a primary electron–hole pair that is subsequently multiplied through an internal avalanche process. This internal gain mechanism enables fast signal amplification with low electronic noise, making APDs particularly well suited for transmission and fluorescence EXAFS measurements where precise intensity monitoring and high signal-to-noise ratios are essential [148].

At P64, APDs are routinely used to record the incident and transmitted X-ray intensities (I_0 and I_1) as well as fluorescence signals in energy-scanning X-ray absorption experiments. Their sub-nanosecond temporal response and high count-rate capability ensure distortion-free detection even under the high photon flux delivered by PETRA III. Moreover, APDs exhibit excellent radiation hardness and stability over extended scans, which is critical for collecting reproducible EXAFS spectra over a wide energy range. These characteristics make APDs a reliable choice for high-quality EXAFS measurements, allowing accurate extraction of absorption coefficients and, consequently, robust determination of local structural parameters such as coordination numbers, interatomic distances, and disorder parameters.

3.6 Sample environment: free-flowing liquid jet

All the X-ray absorption and scattering measurements involved in this thesis were conducted in the liquid phase to investigate the structural properties of bimetallic complexes. To perform this, a free-flowing liquid jet was employed as the sample delivery system throughout the experiments during the available beamtimes.

For the EXAFS measurements performed at the P64 beamline of PETRA III, a stable and continuous liquid jet with 500 μm thickness was used. The jet was placed directly on the way of the X-ray beam. The continuous liquid flow was maintained using a peristaltic pump coupled with a damping system which minimized the instabilities induced by pulsation. This configuration ensured a uniform flow, enabling high-quality data acquisition for the whole beamtime, while minimizing radiation damage through constant sample renewal in the beam path [120].

For the WAXS experiment performed at the FXE beamline, a thinner liquid jet was utilized to cope up with the high brilliance and high repetition rate of EuXFEL and to improve temporal resolution degrading due to group velocity mismatch of the X-ray and optical pulses in the jet [136]. The inner diameter of the glass nozzle was 100 μm to allow a more collimated and stable jet stream. With the MHz repetition rates of EuXFEL, the investigation of structural dynamics was performed in acetonitrile solvent at very low concentrations (<5 mM). For this purpose, a dedicated He-filled sample chamber is available with large windows which allows simultaneous diffraction/scattering and spectroscopic experiments using the LPD detector and the von Hamos or Johann spectrometers, respectively. The chamber can be sealed with a Kapton window supported on aluminium frame attached by magnets. Three precision motors are mounted outside the chamber to avoid the possible chemical contamination due to the leaks or spraying of the liquid jets. These motors manipulates the XYZ translation stages of the nozzle to position the jet along the beam with a ca. 1 μm reproducibility [149]. A gas inlet with helium was employed as the filling gas to minimize X-ray attenuation and reduce undesired scattering contributions. The incident beam was guided through a 2 mm-thick silver flight tube inside the chamber, which contained the beam up to approximately 15 mm before the jet. A sample catcher is positioned into a 5 mm-diameter tube from the bottom of the chamber to collect the liquids from jet, directing it return back into the sample bottle located beneath the chamber. A scheme of sample delivery system is illustrated in Figure 3.11, adapted from [149].

The liquid solutions were continuously circulated using a high-performance liquid chromatography (HPLC) pump, which was connected to a round glass nozzle. The flow rate was maintained at approximately 30 mL/min with velocities up to approximately 64 m/s, ensuring complete sample renewal between consecutive pump–probe events at repetition rates of up to 564 kHz. This estimate depends on the solvent viscosity and the back pressure needs to be adjusted to ensure uninterrupted flow during the high-repetition-rate measurements. Two additional sample circulation pumps were connected with the sample delivery system for the study of in-line static UV-VIS spectroscopy and for solution/solvent refill to maintain constant sample concentration. All the pumps can be controlled remotely. The overall sample delivery system at FXE is

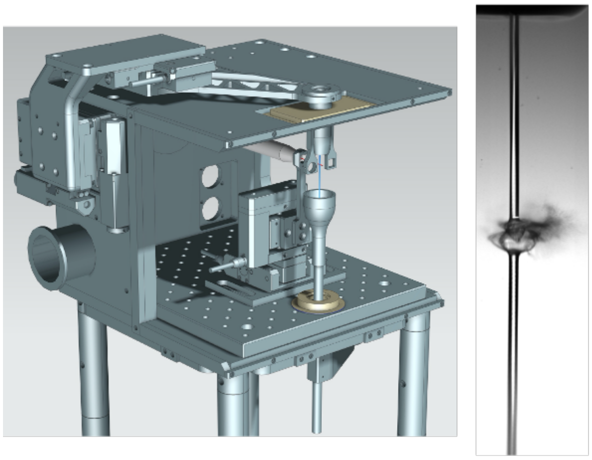

Figure 3.11: Scheme of liquid sample delivery system at FXE beamline with closed system facility.

suitable for the femtosecond-resolved studies, where sample path length and jet stability are critical for minimizing X-ray scattering background and achieving high temporal and spatial resolution.

Chapter 4

Total Synthesis of Metal dimers

In this thesis, the synthesis of bimetallic complexes with phosphine ligands from basic starting material constituted a crucial component of the thesis work and was given particular importance, as the preparation of these compounds was an essential prerequisite for subsequent experimental investigations. All synthetic work was carried out by the author, at the University of Leipzig in the laboratory of Prof. Dr. Evamarie Hey-Hawkins with Peter Wonneberger, and at the University of Hamburg in the laboratory of Prof. Axel Jacobi von Wangelin.

4.1 Chemicals

All reagents were purchased from commercial suppliers and used without further purification, except for the solvents. All solvents were dried and degassed using standard laboratory techniques when required. Due to the toxicity and corrosive nature of several reagents, particularly Na metal, HF-containing species and volatile organic solvents, all procedures were performed in a well-ventilated fume hood with appropriate personal protective equipment.

4.2 Chemistry laboratory setup

All reactions and manipulations were carried out under a dry argon atmosphere by using standard vacuum-line techniques. Solvents were purified, dried, deoxygenated, and distilled before use. The synthesis commenced with preparation of the apparatus. All of the glassware used during the synthesis process were thoroughly cleaned using multiple solvents to remove any contaminants, then dried under an inert gas stream to ensure a moisture-free environment. The dried glassware was then purged and filled with flowing argon gas to maintain an inert atmosphere throughout the reaction.

4.3 Synthesis of PNNP Ligand

Step 1

The prepared three-necked round-bottom flask was flushed with a steady stream of argon gas to ensure an inert atmosphere. Into this inert flask, 35 g of diethyl phosphite was dissolved in 150 ml of anhydrous diethyl ether. Separately, another solution was prepared by dissolving 0.217 mol (30 g) of diethyl phosphite in 150 ml of diethyl ether, and this mixture was carefully cooled to -5°C.

Small pieces of sodium metal (5 g, 0.217 mol) were then added incrementally to the cooled solution. Each addition of sodium raised the temperature of the mixture, so an isopropanol bath with crushed ice was used to maintain a controlled temperature range of -5°C to +5°C. To prevent excessive temperature increase, no more than 3-5 pieces of sodium were introduced at once.

After all sodium had been added, the reaction mixture was continuously stirred within the isopropanol bath to sustain a stable temperature as the sodium reacted completely. This reaction process required approximately eight hours to ensure the full consumption of sodium.

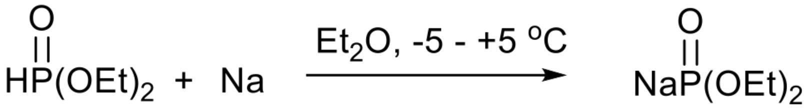

$$\overset{O}{\overset{||}{HP(OEt)_2}} + Na \xrightarrow{Et_2O,\ -5\ -\ +5\ ^{o}C} \overset{O}{\overset{||}{NaP(OEt)_2}}$$

1 **2**

Step 1: Synthesis of compound 2

Step 2

In an Erlenmeyer flask with a volume capacity of 250–500 mL, pyridine-N-oxide (20.4 g, 0.217 mol) was introduced as the starting material. To this flask, dimethyl sulfate (27.3 g, 0.217 mol) was gradually added in a stepwise manner while maintaining the temperature of the reaction mixture at 0°C. The controlled addition at low temperature minimizes the risk of exothermic reactions and aids in maintaining safe reaction conditions. During the addition process, the reaction mixture was continuously stirred to facilitate thorough interaction between the reactants. Stirring was continued until all the pyridine-N-oxide had completely dissolved, ensuring the formation of a homogeneous solution that indicated the completion of the initial phase of complex formation.

Steps 1 and 2 are considered complete when the sodium is fully dissolved in the diethyl phosphite solution in diethyl ether, and the pyridine-N-oxide is entirely dissolved in dimethyl sulfate (Me_2SO_4).

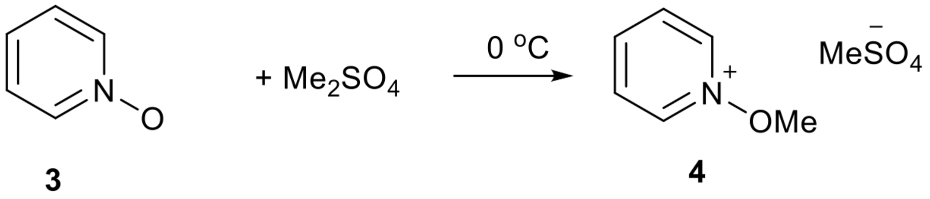

Step 2: Synthesis of compound 4

Step 3

After completing steps 1 and 2, an additional 50 ml of diethyl ether were added to the reaction mixture. The pyridinium salt (compound 4) was then placed in a dropping funnel, and ensure the reaction mixture remained cooled to -5°C. The addition of pyridinium salt was subsequently started dropwise, ensuring that the temperature remained between -5°C and 0°C throughout the process.

Important Safety Note: The reaction does not initiate immediately, leaving the pyridinium salt initially undissolved in the reaction mixture. However, after the addition of 5-15 ml of the compound 4, the reaction will proceed rapidly, accompanied by an exothermic release of energy. To prevent spillage or ejection of the reaction mixture, pauses were introduced after every 5-7 drops of the salt. The reaction was carefully monitored for any signs of diethyl ether boiling; if boiling was observed, the addition of the salt was paused, and liquid nitrogen was immediately added to the cooling bath to maintain stability.

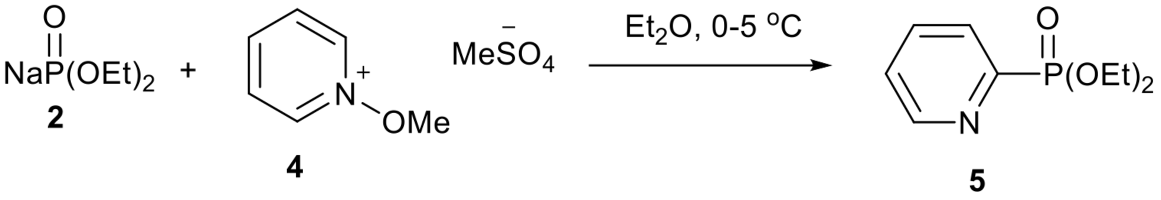

Step 3: Synthesis of compound 5

Once the reaction mixture developed a slight brown color, the dropwise addition of pyridinium salt was resumed without interruption, while continuously monitoring the temperature of the cooling bath and the boiling point of diethyl ether. After the complete addition of the pyridinium salt, the cooling bath was allowed to warm gradually to room temperature. Upon reaching room temperature, the cooling bath was removed, and the reaction mixture was stirred for an additional 12-14 hours.

Subsequently, the reaction mixture was cooled to between 0°C and +5°C, and carefully 100 mL of distilled water was added dropwise. There are two layers of solvents in the reaction mixture: the upper organic solvent layer and the lower aqueous layer.

The organic solvent layer was separated using a 500-1000 ml separating funnel and transferred into a flask containing Na_2SO_4 or $MgSO_4$ for drying. The aqueous layer was washed with 100 mL of chloroform in three separate steps. All the collected organic layers were combined and allowed to dry over Na_2SO_4 or $MgSO_4$ overnight.

The dried solution was transferred to a clean 1000 mL round-bottom flask and the solvent was evaporated by distillation. The residue was distilled under reduced pressure (10^{-2} to 10^{-3} mbar), considering the boiling point between 120-140 °C at this pressure. The temperature of the heating bath should not exceed 185 °C, as temperatures above this threshold may lead to decomposition of the product.

Step 4

A suspension of $LiAlH_4$ (1.5 - 2 equivalents) in 200 mL of diethyl ether, and to this, a solution of diethylpyridine-2-phosphonate (compound 5) (1 equivalent) in 50 ml of diethyl ether was added dropwise, slowly, while maintaining the temperature at $-5\,^\circ$C. The addition of the phosphonate was accompanied by an exothermic reaction. After addition of all the phosphonate, the temperature of the reaction mixture was increased gradually to room temperature. The reaction mixture was stirred for 12-20 hours at room temperature. In the next step, approximately 100 ml degassed distilled water was added drop-wise to the reaction mixture, although the exact volume depends on the condition of the decomposed $LiAlH_4$. Once the solid phase started to form small balls the addition of water was stopped. The amount of added water is very crucial as excessive water can enhance the chance to form a paste-like consistency from the precipitate, which can complicate the subsequent extraction process. After the addition of water, the organic layer was separated using a cannula and transferred into a flask containing Na_2SO_4 or $MgSO_4$ for drying. The aqueous layer containing the decomposed $LiAlH_4$, was extracted with 100 mL of diethyl ether three times. The combined organic layers were then dried over Na_2SO_4 or $MgSO_4$ for at least 8 hours. Subsequently, the diethyl ether was removed by distillation, and the residue was distilled under vacuum to obtain pure $PyPH_2$, with a boiling point of 40-60 °C at 10-20 mbar. The color of the $PyPH_2$ product may vary, appearing orange, pink, or red.

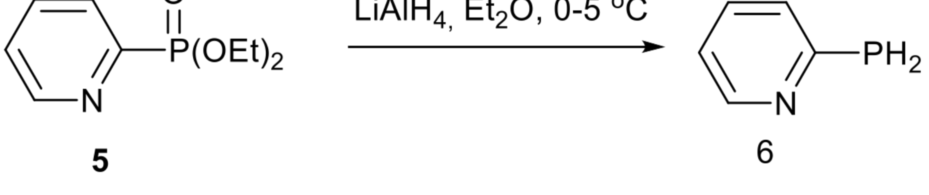

Step 4: Synthesis of compound 6

Step 5

All reactions and manipulations were carried out under a dry argon atmosphere by using standard vacuum-line techniques. A mixture of 2-pyridylphosphine (1.39 g, 12.5 mmol) and paraformaldehyde (0.75 g, 25.0 mmol) was stirred at 110-120°C until the mixture became homogeneous. To this, 5 ml of dry ethanol and a solution of p-toluidine (12.5 mmol) in 5 ml of ethanol were added. The reaction mixture was stirred at 80°C for 2 hours, during which a white precipitate formed. The precipitate was filtered, washed with ethanol three times, and dried under reduced pressure.

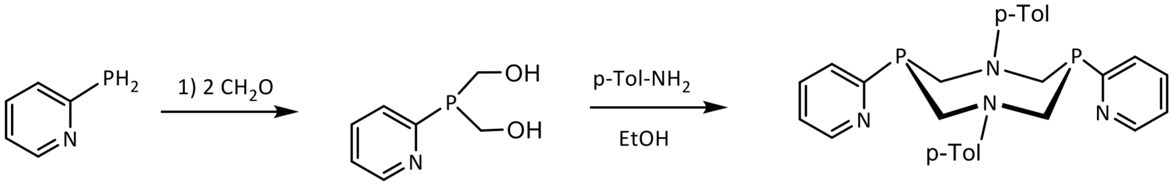

Step 5: Synthesis of PNNP ligand

The ^{31}P NMR spectrum of the product should show a signal at -40 to -45 ppm. Additionally, a minor signal may appear in the range of -30 to -35 ppm, which could correspond to another isomer of 1,5-diaza-3,7-diphosphacyclooctane. However, this minor signal will not affect the outcome of subsequent reactions. All procedures were performed under an inert atmosphere. A mixture of 12.5 mmol of 2-pyridylphosphine (1.39 g) and 25.0 mmol of paraformaldehyde (0.75 g) was heated and stirred at 110-120°C until the mixture became homogeneous. To the obtained homogeneous mixture, 5 mL of dry ethanol and a solution of p-toluidine (12.5 mmol) in 5 mL of ethanol were added. The reaction mixture was stirred for 2 hours at 80°C, resulting in the formation of a white precipitate. The precipitate was filtered, washed three times with ethanol, and then dried under reduced pressure.

4.4 Synthesis of [Au_2(pnnp)Cl_2] and [Au_2(pnnp)$_2$]Cl_2

5 g of tetrachloroauric(III) acid hydrate was dissolved in a mixture of ethanol (40 ml) and distilled water (10 mL). To the resulting solution, tetrahydrothiophene (2.5 equivalents) was added dropwise using a glass pipette. After the complete addition, a white precipitate was formed. The reaction mixture was stirred for 30 minutes, with the flask wrapped in aluminum foil to protect it from light. Then the precipitate was filtered and washed with ethanol three times, followed by washing with diethyl ether three times. Finally, the precipitate was dried under vacuum to remove any residual solvents.

Important Safety Note: It is essential to avoid the use of metal equipment during this synthesis, as gold(III) acid can cause the oxidation of metals, leading to contamination of the product with iron oxides. Only glass equipment should be used.

Synthesis of [Au(tht)Cl]

4.4.1 Synthesis of [Au_2(pnnp)Cl_2]

To a solution of [Au(tht)Cl] (2 equivalents) in dichloromethane (5 ml), a solution of the ligand (1 equivalent) in dichloromethane (5 ml) was added. The reaction mixture was stirred for 0.5 hours at room temperature, protected from light. After this period, a white precipitate formed. The precipitate was then filtered and washed thrice with 10 mL of dichloromethane each time. The desired product was 1.5 g of the complex. To obtain a larger quantity of the product, it is recommended to perform the synthesis in multiple batches, using 200-300 mg of the ligand per batch.

Synthesis of [Au_2(pnnp)Cl_2]

The synthesized complex was characterized by UV–Vis spectroscopy, which clearly displayed two distinct electronic transitions. The spectrum, shown in Figure 4.1, is in good agreement with the reported literature data for [Au_2(pnnp)Cl_2] in acetonitrile, thereby confirming the successful formation of the desired complex. The absorption band observed below 270 nm corresponds to π-π^* transitions within the pyridyl and para-tolyl moieties of the ligand. A broader feature in the range of approximately 290–330 nm is attributed to electronic transitions from the HOMO, predominantly localized on the para-tolyl fragments, to the LUMO, which is contributed by the atomic orbitals of both Au(I) ions and the pyridyl groups. This band arises from intraligand charge transfer (ILCT) processes mixed with ligand-to-metal charge transfer (LMCT) character.

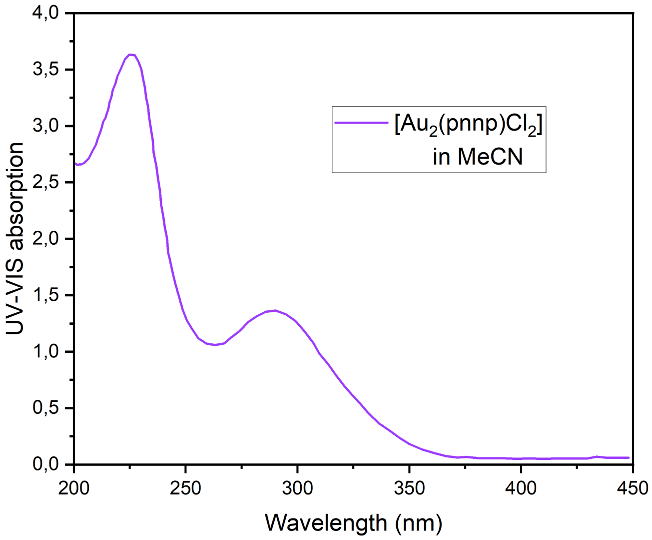

Figure 4.1: UV-Vis absorption spectrum of the synthesized [Au$_2$(pnnp)Cl$_2$] complex in acetonitrile solution which appears identical to the literature spectrum.

4.4.2 Synthesis of [Au$_2$(pnnp)$_2$]Cl$_2$

A solution of [Au(tht)Cl] (1 equivalent) in acetone (5 ml) was prepared, to which a solution of the ligand (1 equivalent) in acetone (5 ml) was added. Acetone was used as the solvent to ensure the separation of the resulting complex, as the product is insoluble in acetone. The reaction mixture was stirred for 0.5 hours at room temperature, protected from light. After this period, a white precipitate formed. The precipitate was filtered and washed thrice with 10 ml of acetone each time. The desired product was 1.5 g of the complex. To obtain a larger quantity of the product, it is recommended to perform the synthesis in multiple batches, using 200-300 mg of the ligand per batch.

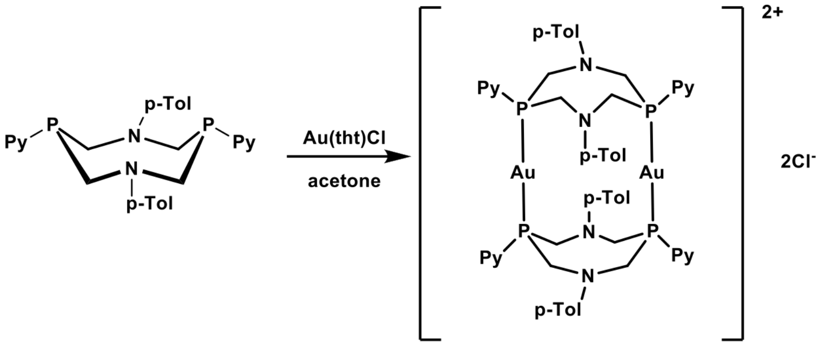

Synthesis of [Au$_2$(pnnp)$_2$]Cl$_2$

The synthesized complex was characterized by UV–Vis spectroscopy, which clearly displayed two distinct electronic transitions and are analogous to those observed for

$[Au_2(pnnp)Cl_2]$. The UV–Vis spectrum in Figure 4.2 resembles the reported literature data for $[Au_2(pnnp)_2]Cl_2$ complex in acetonitrile.

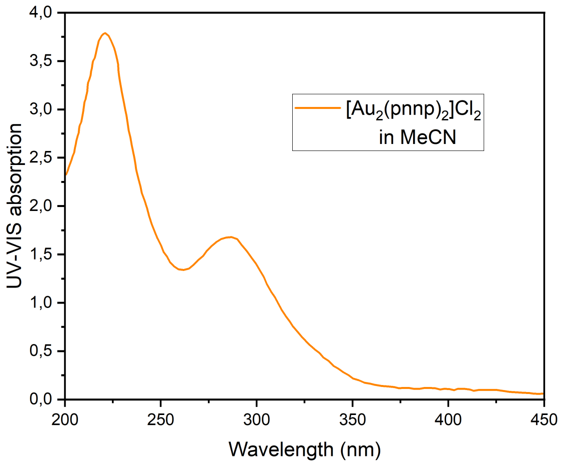

Figure 4.2: UV-Vis absorption spectrum of the synthesized $[Au_2(pnnp)_2]Cl_2$ complex in acetonitrile solution which appears identical to the literature spectrum.

4.5 Synthesis of $[Au_2(dcpm)_2](PF_6)_2$

In a 100 mL Erlenmeyer flask, 1.06 mmol of $K[AuCl_4]$ (0.4 g) was dissolved in 40 mL of methanol and stirred for 10 minutes on a stirring heating mantle. Once the $K[AuCl_4]$ was fully dissolved, 2.12 mmol of thiodiglycol (0.22 mL) was added to the reaction mixture, which was then stirred for an additional 15 minutes. Then 1.04 mmol of solid bis(dicyclohexylphosphino)methane (dcpm) ligand (0.4 g) was added, and the mixture was stirred for another 15 minutes. Over time, a pale-yellow solid formed but dissolved upon gentle warming, yielding a colorless solution that was subsequently filtered. In the filtrate, excess NH_4PF_6 (approximately 4 g) was added, resulting in the formation of white precipitates. These precipitates were collected by filtration, then washed with distilled water and diethyl ether. The collected solids were further purified by recrystallization through slow evaporation from acetonitrile.

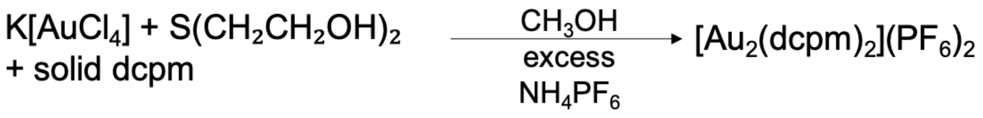

The compounds were characterized by ^{31}P NMR spectroscopy and UV-Vis spectroscopy. Figure 4.3 represents the UV-Vis spectrum for the $[Au_2(dcpm)_2](PF_6)_2$ complex in acetonitrile solution which is similar to the UV-Vis spectrum published in literature.

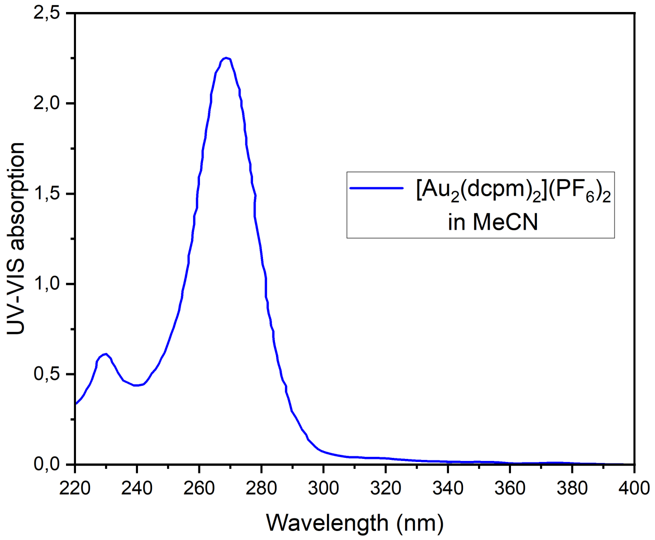

Figure 4.3: UV-Vis absorption spectrum of the synthesized $[Au_2(dcpm)_2](PF_6)_2$ complex in acetonitrile solution which is identical to the literature spectrum.

4.6 Synthesis of $[Ag_2(dcpm)_2](PF_6)_2$

In this synthesis, a suspension of silver hexafluorophosphate ($AgPF_6$) (0.10 g, 0.40 mmol) was prepared in 40 mL of dichloromethane, and bis(dicyclohexylphosphino)methane (0.16 g, 0.40 mmol) was added to the solution. The reaction mixture was stirred at 40°C for 5 hours, ensuring thorough mixing of the reagents to promote effective interaction between $AgPF_6$ and bis(dicyclohexylphosphino)methane. During this time, the suspension gradually developed, allowing the complexation to proceed under mild heating conditions. After the reaction time, the reaction mixture was concentrated by carefully reducing the solvent volume, which encouraged the formation of a solid product. Following this concentration step, diethyl ether was added to the mixture. The addition of diethyl ether induced the precipitation of a white crystalline solid, suggesting successful formation of the desired $[Ag_2(dcpm)_2](PF_6)_2$ complex.

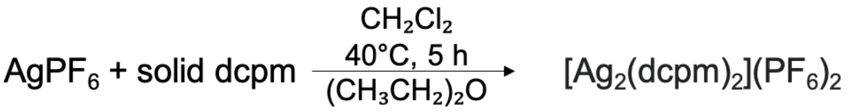

$$AgPF_6 + \text{solid dcpm} \xrightarrow[(CH_3CH_2)_2O]{CH_2Cl_2,\ 40°C,\ 5\ h} [Ag_2(dcpm)_2](PF_6)_2$$

To purify the product, recrystallization was conducted. This involved setting up a diffusion process where diethyl ether was allowed to slowly diffuse into a dichloromethane solution of the crystalline solid. Over time, this controlled diffusion resulted in the formation of pure colorless crystals, which were subsequently isolated as the final product. The recrystallization method by ether diffusion into dichloromethane provided an effective means to obtain high-purity crystals suitable for further characterization.

4.7 Synthesis of $[Cu_2(dcpm)_2](PF_6)_2$

Synthesis of $[Cu(CH_3CN)_4][PF_6]$

The following synthesis was conducted under a well-ventilated fume hood due to the toxic nature of acetonitrile and the hazardous hydrofluoric acid (HF) fumes generated during the procedure. Proper personal protective equipment (PPE) including gloves, safety goggles, and a lab coat were used, and all the measures were taken to avoid exposure to fumes or accidental contact with reagents.

A magnetically stirred suspension of 28 mmol of copper(II) oxide (4.0 g) was prepared in 80 mL of acetonitrile within a dry 125-mL Erlenmeyer flask. To this suspension, 10 mL of 60–65% HPF_6 (approximately 113 mmol) was added incrementally in 2-mL portions. The reaction was highly exothermic, leading to noticeable boiling of the solution. While the elevated temperature was not strictly controlled, the resultant warming was advantageous as it facilitated the dissolution of the reaction product. After the final portion of HPF_6 was added, the solution was stirred for an additional three minutes to ensure completion of the reaction.

The hot reaction mixture was then filtered through a medium-porosity fritter filter to remove small quantities of undissolved black residue. During this filtration step, some white crystalline material identified as $[Cu(CH_3CN)_4][PF_6]$ occasionally formed prematurely. This crystalline material was washed through the frit using a minimal volume of acetonitrile to ensure complete recovery. The resulting pale-blue solution was cooled to approximately $-20\,^{\circ}C$ by placing it in a freezer for several hours. Alternatively, equivalent results were achieved by adding an equal volume of diethyl ether and cooling the mixture to $0\,^{\circ}C$. In either case, cooling induced the formation of a microcrystalline blue-tinged white precipitate of $[Cu(CH_3CN)_4][PF_6]$. This solid product was collected by filtration and subsequently washed with diethyl ether to remove any residual impurities.

$$Cu_2O + HPF_6 + CH_3CN \longrightarrow [Cu(CH_3CN)_4]PF_6$$

The collected solid was immediately redissolved in 100 mL of acetonitrile to prepare it for further purification. A small amount of undissolved blue material, presumed to be a Cu^{2+} species, was observed in the solution and was removed by filtration. The slightly blue filtrate was then treated with 100 mL of diethyl ether and allowed to stand at $-20\,^{\circ}C$ for several hours, resulting in the precipitation of the target complex. If the precipitated complex exhibited a bluish cast, indicating the presence of impurities, a second recrystallization was performed to enhance the purity of the product. The second recrystallization was carried out by dissolving the impure product in 80 mL of acetonitrile and subsequently adding 80 mL of diethyl ether. The mixture was then cooled to $-20\,^{\circ}C$ to induce recrystallization. The purified product, now appearing as a pure white solid, was collected by filtration, washed with diethyl ether, and immediately dried under vacuum for approximately 30 minutes to remove residual solvents.

The final yield of $[Cu(CH_3CN)_4][PF_6]$ was 12.5 g, corresponding to a 60% yield. The overall yield was influenced by losses incurred during the recrystallization process. The pure white product was suitable for further applications or characterization, highlighting the efficiency of this synthesis and purification method.

Synthesis of $[Cu_2(dcpm)_2](PF_6)_2$

A mixture of $[Cu(CH_3CN)_4][PF_6]$ and bis(dicyclohexylphosphino)methane (dcpm) in a 1:1 molar ratio was prepared by combining the two reagents in 20 mL of acetone. This mixture was stirred at room temperature for 1 hour to ensure complete reaction between the components. After the stirring period, the acetone solvent was removed under reduced pressure, yielding a concentrated reaction mixture. Diethyl ether was then added to the residue, leading to the formation of a white solid precipitate. This solid was collected and further purified by recrystallization.

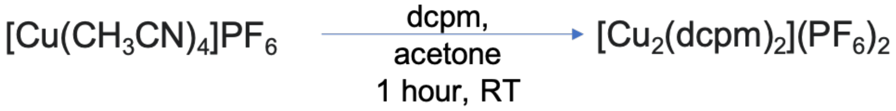

Recrystallization was achieved by dissolving the precipitate in a small amount of dichloromethane (CH_2Cl_2), followed by the slow addition of diethyl ether to facilitate the formation of purified crystals. The recrystallized final product was isolated as a white crystalline solid, suitable for further analysis or subsequent pump-probe measurements.

Chapter 5

Refining the ground state structure of gold dimers in solution phase

This chapter contains the detailed experimental results and data reduction procedure for the collected data from P64 beamline at Petra III using the EXAFS technique. This chapter begins with the EXAFS data reduction processing, followed by the ground state structural refinement for the $[Au_2(dcpm)_2](PF_6)_2$ complex in MeCN solution.

5.1 EXAFS data analysis

As described in the previous chapters, EXAFS provides detailed information on the local atomic environment, primarily bond distances and coordination shells around the absorbing atom in both ordered and disordered materials. The theoretical details of EXAFS technique are explained in Section 2.2.2 underlining the possibility of extracting relevant structural information about the material of interest.

To establish a meaningful correspondence between the experimental measurements and theoretical models, it is important to isolate the EXAFS oscillations, $\chi(k)$, from the collected absorption spectrum data. In this work, the EXAFS measurements were performed in acetonitrile solution at relatively low concentrations, a condition particularly relevant for probing aurophilic interactions in the $[Au_2(dcpm)_2](PF_6)_2$ complex. However, such measurements also make analysis challenging, as the signal intensity in solution is significantly weaker than that obtained from solid powders, leading to a lower signal-to-noise ratio and requiring careful data processing and averaging [38]. The systematic procedure of steady-state EXAFS data reduction and extraction of physical parameters are described in this section.

To enable efficient and accurate analysis of XAS data, several software packages have been developed including APEX program [150] and IFEFFIT packages [151] which fulfill a broad range of analytic and simulation goals. The IFEFFIT library includes ATHENA, and Artemis which provide a comprehensive, user-friendly graphical interface.

For data analysis of $[Au_2(dcpm)_2](PF_6)_2$ complex in acetonitrile solution, ATHENA and Artemis software were used. Both of them are built using the numerical and analytical capabilities of the IFEFFIT library [106] including the complete access of the AUTOBK [152] and FEFFIT program [153].

5.1.1 Data processing

ATHENA software is used for processing the raw data for further analysis where the data processing employs several steps including the conversion of raw data to $\mu(E)$ spectra, refining of the recorded data by rebinning, automated deglitching, truncation, and calibration. Then the background subtraction from the data is carried out using the AUTOBK [152] that fits a smooth spline curve to the absorption spectrum. This technique separates the EXAFS signal from the background by analyzing the difference in their Fourier components. ATHENA has another great feature of data merging by averaging several scans to obtain a good quality EXAFS spectrum. After that, the normalization of the data scans is performed. The normalization of the absorption spectrum involves the following key steps to isolate the EXAFS oscillations:

- **Threshold Energy Determination (E_0):** This is the energy at which the first derivative of the absorption coefficient $\mu(E)$ reaches its maximum. This energy marks the onset of the absorption edge and considered as the reference point for subsequent normalization.

- **Pre-edge and Post-edge Fitting:** Smooth polynomial functions are fitted to the pre-edge and post-edge regions of the spectrum to model the baseline absorption behavior. These polynomials are extrapolated to the threshold energy E_0, and the difference between their values at E_0 is defined by the edge step.

- **Normalization of the Spectrum:** The absorption spectrum is normalized by using the relation defined by Equation 2.22 - where $\mu(E)$ is the experimental absorption coefficient, $\mu_0(E)$ is the fitted background representing the absorption of an isolated atom, and $\mu_0(E_0)$ is absorption value at the edge energy E_0, used here to normalize the oscillatory component. The absorption coefficient in the pre-edge region becomes zero and normalizes the post-edge region to oscillate around one.

- **Extraction of the EXAFS oscillation function $\chi(E)$:** The $\chi(E)$ is converted to the photoelectron wavenumber k, by the Equation 2.23. The final EXAFS function $\chi(k)$ is multiplied by k^n, where $n = 1, 2$, or 3. The multiplication enhances the oscillations at higher k-values, improving the signal-to-noise ratio during the Fourier transformation [154].

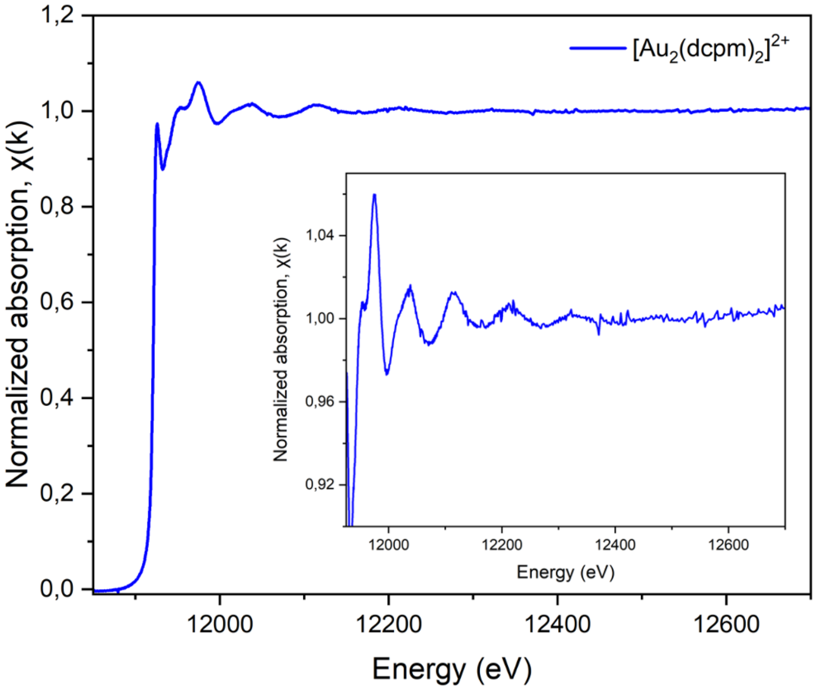

Figure 5.1: Experimental EXAFS signal of $[Au_2(dcpm)_2](PF_6)_2$ in acetonitrile, collected at P64 beamline. Inset shows a zoom of the higher energy range.

After the extraction of EXAFS function $\chi(k)$, the structural analysis can be performed in two ways. The first process follows the direct fitting of the $\chi(k)$ in k-space while the other method performs fitting of the Fourier transformation (FT) result in the real space (R-space). Figure 5.1 represents the EXAFS energy spectrum vs. $\chi(k)$. The FT of the $\chi(k)$ can be represented as the data in the form of a pseudo-radial distribution function $\chi(R)$. The peak positions and intensities in the $\chi(R)$ correspond to the phase shift which is the average distance from the absorber to the neighboring atoms, their types and quantity. For more focused and accurate analysis, the specific region of $\chi(R)$ are selected and a backward Fourier transformation is performed. The selected region usually contains the first or the first and second coordination shell peaks. The backward Fourier transformation isolates the contribution of those specific region to the overall EXAFS signal [154]. In the next section the fitting process using Artemis software is described.

5.1.2 Data reduction

After performing all the previous steps, the extracted EXAFS oscillations function from ATHENA contains important structural and non-structural parameters and the fitting procedure is performed to extract those parameters from the measured experimental data of the studied molecule. The fitting process is performed by comparing the experimentally measured EXAFS oscillation function to a theoretically calculated one.

To analyze the EXAFS oscillations of $[Au_2(dcpm)_2](PF_6)_2$ complex, the fitting process of the ground-state EXAFS spectra is carried out using the software named Artemis which is a part of the IFEFFIT packages [151]. This also includes FEFF codes which is explained elaborately in Section 2.2.2 [102]. The fitting process starts with a choice of model structure as the starting guess structure for the FEFF calculation (here FEFF 6.0 is used). This guess input model structure should be reasonably close to the structure of interest and are often either the DFT optimized coordinates or the X-ray crystallographic data. In this work, the optimized input atomic coordinates were used, prepared by Dr. Dmitry Khakhulin using DFT calculations in ORCA. Used feff.inp file to fit the $[Au_2(dcpm)_2](PF_6)_2$ EXAFS data is provided in the Appendix A. This feff.inp file is used to calculate the self-energy, Muffin-tin potentials, amplitude reduction factor (S_0^2) and phase shift ($\Phi(k)$) which are necessary to generate the fine structure according to the EXAFS equation (see Section 2.2.2 and Equation 2.24 for more details):

Artemis software provides convenient parameterization and refinement of structural variables in the EXAFS equation. The k - dependent scattering amplitudes Fj(k) ($F_j(k)$ and phase shifts ($\Phi(k)$), provided by the FEFF calculation remain constant during the fitting process. From the input structure, FEFF calculates all the scattering paths from the target atom of the molecule. As an output, a list of single and multiple scattering paths is generated and ordered according to their effective bond distance R_{eff} up to the maximum path length of R_{max}. From this scattering path list, one needs to consider the relevant paths to include in the fit. In this work, the feff.inp file produced a total of 880 scattering paths within 6.0 Å(including single- and multiple-scattering) where 9 of them have amplitudes higher than 19% (see Table 5.1). Those selected paths were then used by an appropriate parameterization strategy and evaluated by different combinations of fitting parameters with physically and chemically meaningful results.

Table 5.1: Calculated scattering paths using FEFF 6.0 using the input file of Appendix A. Only paths with amplitudes higher than 19% are listed. This includes both the single- and multiple scattering paths. Here, N is path degeneracy; R_{eff} is the effective path distance (in Å); Ampl. is amplitude (in %), SS and MS denote for the single scattering and multiple scattering paths

No.	**N**	**R_{eff} (Å)**	**Amplitude (%)**	**Type**	**Pathway**
1	2	2.330	100	SS	Au–P-Au
2	1	2.882	27.13	SS	Au-Au-Au
3	2	3.410	26.29	SS	Au-C-Au
4	2	3.486	24.70	SS	Au-C-Au
5	2	3.527	23.88	SS	Au-C-Au
6	2	3.580	22.90	SS	Au-C-Au
7	2	3.748	24.81	SS	Au-P-Au
8	2	3.768	19.72	SS	Au-C-Au
9	8	3.835	24.39	MS	Au–P–C-Au

Among all the calculated scattering paths, only the first 3 dominating paths from Table 5.1 were used for the fitting of Au L_3-edge of the $\text{Au}_2(\text{dcpm})_2(\text{PF}_6)_2$ complex. The Au-P-Au contributes the maximum scattering amplitude followed by the Au-Au-Au (Au1-Au2-Au1) scattering path. The Au-C-Au scattering paths are less dominant compared to the first two paths but may still contribute to the EXAFS signal. To improve the fitting quality in the higher-shell fitting, one of the Au-C-Au scattering path was included. Figure 5.3 shows the fitting with these selected paths.

During the EXAFS analysis, the Nyquist theorem is followed to estimate the maximum number of independent fitting parameters (N_{ind}) that can be reliably extracted from experimental data [88].

$$N_{\text{indep}} = \frac{2\Delta k \Delta R}{\pi} + 1 \tag{5.1}$$

where Δk is the data range selected in k-space (in Å^{-1}), and ΔR is the data range selected in real (R) space (in Å). For the analysis of EXAFS data of $Au_2(dcpm)_2(PF_6)_2$ complex in acetonitrile solution, the fitting is performed in R-space over the k-range from 3.0 Å^{-1} to 11.0 Å^{-1} using a Hanning-type window and ΔR is in the data range of 2 Å. The Hanning-type window is used to reduced the edge effects during Fourier transformation.

The primary objective of the EXAFS fitting in ground state structure is to refine the most significant structural parameters obtained from DFT calculation and to extract the key fitting parameters such as the Debye-Waller factors (σ^2), the amplitude reduction factor (S_0^2), the overall energy shift (ΔE_0) of the theoretical spectra to the experimental spectra and the change in bond distances between the neighboring atoms (ΔR). The fitting model has 12 parameters in total which is the maximum limit of Artemis software.

5.1.3 Ground state structural analysis

The EXAFS experiment was performed at the Au L_3-edge to extract quantitative structural information in the solution phase ground state of $[Au_2(dcpm)_2](PF_6)_2$ complex. Following the data processing and normalization using ATHENA, the $\chi(k)$ spectra of EXAFS signal (section 5.1) were modeled in Artemis, wherein the scattering paths were generated using FEFF based on the DFT calculated structure of the complex. The EXAFS data and corresponding fit results for the $[Au_2(dcpm)_2](PF_6)_2$ complex in acetonitrile solution are shown in Figure 5.2 and 5.3.

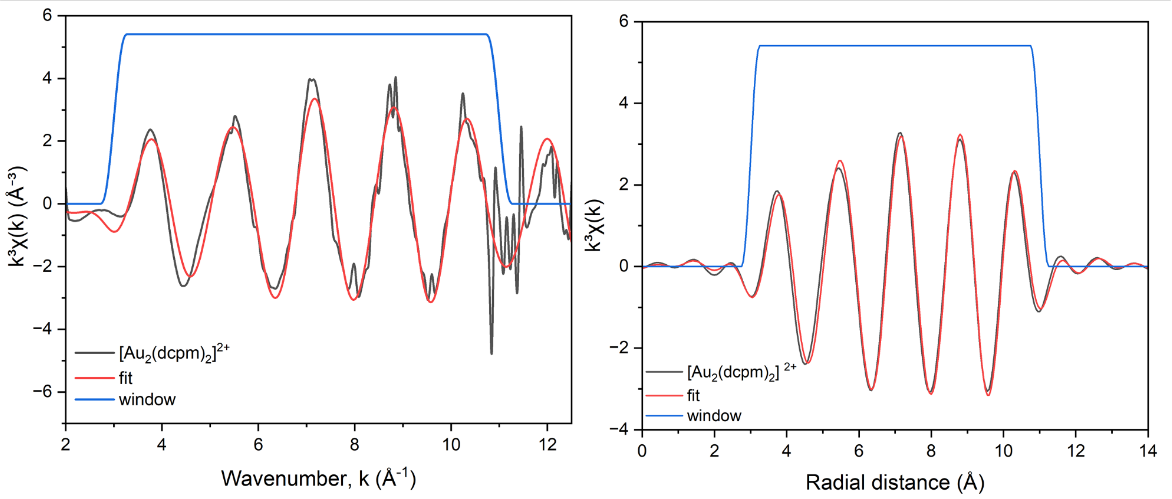

Figure 5.2: EXAFS signal of $[Au_2(dcpm)_2](PF_6)_2$ in acetonitrile, fitted with the simulated ground state structure obtained from DFT calculations. Left: fitting in k-space. Right: fitting in R-space.

Figure 5.2 illustrated the fitting in both k-space (left panel) and q-space (right panel) using the Artemis software package. In the representation, the black curve corresponds to the measured EXAFS data, the red curve to the optimized theoretical fit, and the blue curve indicates the window function used to define the fitting range in k-space. The initial assessment of the EXAFS data was performed in k-space, where the normalized EXAFS signal $\chi(k)$ has been k^3-weighted to amplify the higher-k oscillations and is plotted as $k^3\chi(k)$ against the photoelectron wavenumber k (Å^{-1}). The oscillatory features observed in the EXAFS spectrum provide the main structural sensitivity as they arise from the constructive and destructive interference between the outgoing photoelectron wave and the waves backscattered by neighboring atoms such as P, C, and the second Au center, surrounding the absorbing Au center. The close agreement between the experimental and fitted curves over the full fitting range (k-range) of approximately 3 to 11 Å^{-1} demonstrates that the fitted structural model accurately captures the phase and amplitude of the EXAFS oscillations. This indicates an accurate description of the local atomic structure. The increased fluctuation and deviation observed beyond $\sim$11 Å^{-1} is expected due to the reduced signal-to-noise ratio at higher photoelectron energies.

To isolate and refine specific components of the local structure, a back Fourier transform (back FT) strategy was employed. It involves selecting a specific range in R-space that contains the relevant structural features, applying a window function to filter the signal by excluding contributions from distant or poorly defined scattering paths, and then the filtered signal is back-transformed from R-space to k-space to carry out targeted fitting of those components. The right side of Figure 5.2 shows this back-transformed signal, where the back-transformed EXAFS function $\mathrm{k}^3\chi(k)$ is plotted against radial distance (Å). This representation isolates selected coordination shells, primarily the Au–P, Au–C, and short-range Au···Au distances —while excluding contributions from less-resolved or distant interactions to avoid further complications in the fitting since in general, the solution-phase measurements have more pronounced thermal disorder due to weaker signals and stronger elastic scattering background from the solvent. This focused representation improves the sensitivity and reliability of the fitting process. The close phase and amplitude matching between the filtered data and the model demonstrates that the main oscillatory features of the EXAFS signal originate from the coordination environment immediately surrounding the Au centers. This method also ensures accurate extraction of ground-state structural parameters such as bond distances, coordination numbers, and disorder factors.

A complementary and more intuitive view of the structural environment is obtained by examining the EXAFS data in R-space, as shown in Figure 5.3. This spectrum represents the modulus of the pseudo-radial distribution function, derived from the Fourier transform of the weighted EXAFS signal, $k^3\chi(k)$ function, plotted as a function of radial distance (Å) from the absorbing atom. It is important to note, however, that the distances observed in the R-space spectrum do not directly correspond to the true interatomic separations, as they are systematically shifted to lower R-values due to the phase shifts introduced by the photoelectron scattering process.

In the illustration, the black curve represents the experimental R-space data, while the red curve is the best-fit structural model. The plot also includes the individual contributions from specific scattering paths, such as Au–P (green), Au–C (yellow), and Au···Au (purple), along with the applied R-space window function (blue), which defines the radial range used for the back Fourier transform. The individual path decomposition in R-space provides a clear visual representation of how each scattering interaction contributes to the total EXAFS signal.

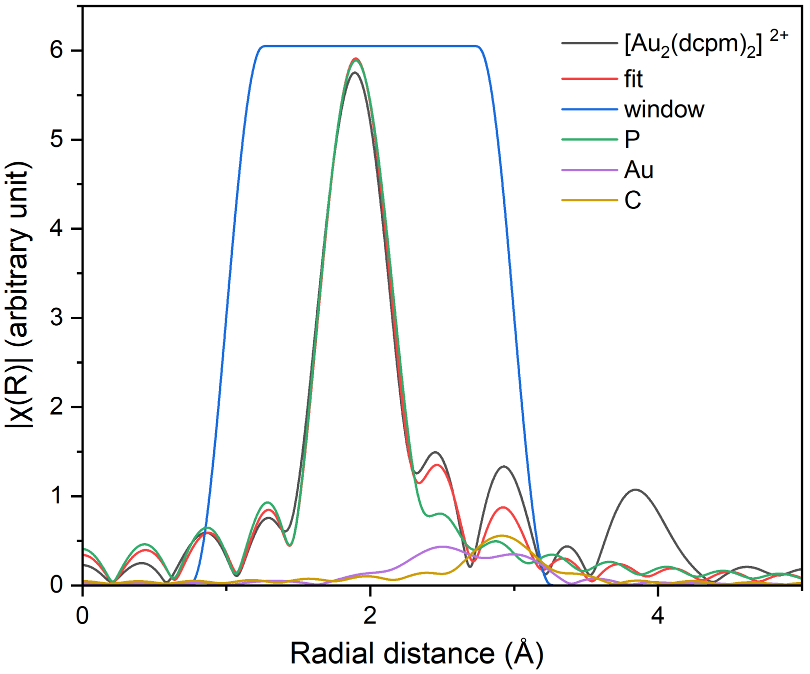

Figure 5.3: Individual contribution of different scattering pathways in EXAFS signal of $[Au_2(dcpm)_2](PF_6)_2$ in acetonitrile, collected at P64 beamline. The fittng was performed with the simulated ground state structure obtained from DFT calculations in r-space.

The dominant peak near ∼1.7-2.2 Å corresponds to the first coordination shell around the Au centers, and the peak near ∼2.9–3.1 Å corresponds to the 2nd coordination shell. After accounting for the phase-shift correction, these peaks correspond to actual interatomic distances of approximately 2.31 Å for the Au–P bond and 3.42 Å for the Au–C coordination, respectively, as obtained from the quantitative EXAFS fitting. The fitting indicates that these peaks are primarily composed of contributions from Au–P and Au–C scattering paths, arising from the dcpm ligands. The relative amplitudes and overlapping phases of these paths are accurately depicted in the fit, confirming that the local geometry around each Au atom includes two P and several C atoms in the expected spatial arrangement of ligands. The window function applied here isolates the most structurally informative region while suppressing contributions from longer-range scatterers and background noise. A weaker but distinct feature at ∼2.2-2.4 Å is assigned to the intramolecular Au···Au interaction, a key structural element of this bimetallic complex. Although this contribution is weaker in amplitude due to its longer distance and the reduced scattering power of gold in this context, the fitting successfully captures its presence and phase. This strongly supports that a short Au···Au contact (∼2.85 Å) persists in solution, which is consistent with the back-Fourier-transformed k-space fit (Figure 5.2, right panel), where the accurate reproduction of oscillatory behavior within the selected R-window further validates the inclusion of the Au···Au path in the model.

The R-space analysis, together with the filtered q-space fitting and the original *k*-space spectrum, provides a comprehensive and consistent picture of the ground-state structure of $[Au_2(dcpm)_2](PF_6)_2$ in solution. The quantitative fitting yielded refined structural parameters that closely match the expected geometry of the complex. The fitted Au–P distance was found to be 2.313 Å in excellent agreement with the crystallographic value (R_{eff} = 2.330 Å), indicating that the primary coordination geometry around Au is preserved in solution. The intramolecular Au···Au separation was refined to 2.893 Å (R_{eff} = 2.882 Å), confirming the persistence of a short Au···Au contact and strong aurophilic interaction under ambient conditions. Additionally, the longer-range Au–C scattering path, associated with the phenyl rings of the dcpm ligands, yielded a distance of 3.420 Å (R_{eff} = 3.410 Å), consistent with a rigid phosphine environment. The corresponding Debye–Waller factors (σ^2), which reflect the static and thermal disorder in each path, were reasonably small across all shells (0.004 - 0.010 $Å^2$,), supporting the presence of well-defined coordination. The fitted structural parameters obtained from Artemis for the $[Au_2(dcpm)_2](PF_6)_2$ complex are summarized in Table 5.2.

Table 5.2: Refined EXAFS fitting parameters for the ground state of $[Au_2(dcpm)_2](PF_6)_2$ complex in acetonitrile.

Scattering path	S_0^2	ΔE_0	R_{eff} (Å)	R_{exp} (Å)	ΔR (Å)	σ^2 ($Å^2$)
Au–P	1	4.575	2.329	2.313	-0.016	0.003
Au–Au	1	6.206	2.882	2.893	0.011	0.004
Au–C	0.987	3.985	3.410	3.420	0.010	0.004

The overall quality of the fit is further supported by the low reduced chi-square (χ^2_{red} = 0.768) and R-factor (0.004), indicating strong agreement between the experimental and theoretical spectra within the fitting range. The amplitude reduction factors (S_0^2) were constrained near unity, as expected from high-Z element Au. The small shift in energy origin (ΔE_0) for each path component (e.g., dep = 4.58 eV for Au–P) was consistent with previously reported values for gold-phosphine complexes [38]. These extracted values confirm that the ground-state structure of the $[Au_2(dcpm)_2](PF_6)_2$ complex in acetonitrile solution maintains the dimeric-ligand configuration and features strong metallophilic interaction as also reported for the solid-state structure [61].

This refined ground-state model serves as the reliable experimentally obtained structural reference for the time-resolved WAXS analysis to trace the transient structural rearrangements and aurophilic interactions following photoexcitation of the $[Au_2(dcpm)_2](PF_6)_2$ complex, as discussed in the following chapter.

Chapter 6

Ultrafast structural dynamics of coinage metal dimers in solution phase

WAXS provides structural information at the atomic to nanoscale level (typically < 10 Å), allowing for the investigation of local structures, phase transitions, and dynamic disorder. Time-resolved difference WAXS signal is highly sensitive to the changes in interatomic distances for all atom types in the probed volume, which makes it suitable for studying liquid phase samples including dilute solutions. The theoretical details of WAXS technique are explained in Section 2.1. With high-brilliance X-ray free-electron lasers (XFEL), the time-resolved WAXS experiments are capable of capturing ultrafast structural dynamics on femtosecond timescales with high signal-to-noise ratio. To extract quantitative information, the collected scattering patterns require careful processing and extraction, as the time-resolved difference signals are typically very weak, often below the permille level relative to the total scattering intensity.

In this section, the procedure for data processing and analysis of the large WAXS data collected during the experimental beamtime at FXE beamline of European XFEL are described briefly. For analysis and extraction of structural parameters from WAXS data, various dedicated Python and Matlab scripts created by Dr. Dmitry Khakhulin and available at FXE were used. Preliminary data reduction for the picosecond WAXS measurements from ID09 beamtline of ESRF synchrotron (sections 6.3.2 and 6.3.3) was performed using a dedicated dedicated txs package developed by Dr. Matteo Levantino [155].

After collecting the scattering data as images, it must undergo a series of preprocessing and data reduction steps before it becomes suitable for quantitative analysis. These steps are described in the following three different parts, denoted as data processing, data reduction and data analysis. Each section provides a concise overview of the workflow involved in transforming the raw detector output into analyzable scattering profiles which is a non-trivial process.

6.1 Data processing

The scattering data acquired in time-resolved liquid WAXS experiments are initially recorded as two-dimensional (2D) diffraction patterns, which must be transformed into one-dimensional (1D) scattering profiles for further analysis. Typically, each image is azimuthally integrated to yield the isotropic scattering intensity $S(q)$ as a function of the momentum transfer q. For each pump–probe delay, multiple images are averaged to improve the signal-to-noise ratio, followed by normalization to the incident X-ray intensity. The transient structural changes are then obtained by calculating the difference scattering signal $\Delta S(q)$ from laser-on and laser-off (or negative delay) conditions. These are suitable for comparing with the model spectra or the simulated scattering curves [77, 156].

At the ESRF ID09 beamline, a commercial Rayonix MX170-HS CCD detector was employed, for which all essential image corrections (dark, flat-field, and geometric) are automatically performed by the detector control system. Consequently, the recorded 2D diffraction patterns could be directly subjected to azimuthal integration without requiring additional preprocessing.

In contrast, the data collected at the FXE instrument at the European XFEL utilized the LPD, a modular prototype detector specifically designed for high-repetition-rate experiments at FXE. Owing to its segmented architecture and multi-gain operation, the raw LPD images require extensive corrections including dark subtraction, gain normalization, and geometric calibration—before azimuthal integration can be performed. These preprocessing steps ensure accurate reconstruction of the full detector image and correct mapping of the scattering intensity onto the reciprocal-space coordinate q. The final output from this workflow is a set of 1D difference scattering curves, suitable for comparison with model spectra or simulated scattering profiles.

For each sample, several scans are generally collected where every scan consists of thousands of images captured per pump-probe delay or incoming laser power setting depending on the type of scan. Typically the scans are collected repeatedly to gain sufficient statistics necessary to extract the small difference scattering signals due to the presence of background noise and artifacts. The data collection generally consists of a reference scan and a fixed delay point or several points forming a delay scan. The reference scans are collected with negative time delays which corresponds to X-ray pulse coming before the laser pulse on the sample jet and measures the steady state scattering while containing all possible artifacts coming from pipe-up of signals from previous pulses within the pulse-train. Moreover within each measurement, the optical excitation laser pulses have half the repetition rate of the X-ray pulses in each train, for example 70.5 kHz for the laser and 141 kHz for X-ray pulses. In this way a fast alternation of Laser-On and Laser-Off images is achieved, allowing to account for slow fluctuations and drifts happening from pulse train-to-train. One the difference scattering curve for a given delay is computed, it is then additionally corrected for a similar difference for negative delay, i.e. for the reference difference curve.

The full list of specific image corrections and data treatment steps is detailed as the following:

- **Raw data:** The collected data is stored in raw format, individually for each of the 16 LPD supermodules. The raw data is initially stored on a fast storage "Online cluster" and is eventually copied to the high-performance Maxwell cluster at DESY. For real-time visualization of the data during the beamtime, online analysis tools such as EXtra-foam [https://extra-foam.readthedocs.io] can be used [157]. However, such visualization does not process the entire data set at full rate and only provides preliminary analysis for initial experimental feedback.

- **Dark correction:** The first step of data processing workflow involves the dark correction of the electronic noise and background signal intrinsic to the detector, referred as the dark current. Even in the absence of both incident X-ray or optical laser pulses, a small current passes across the detector pixels, generating a non-negligible background that varies pixel-by-pixel and depends on the gain setting. To eliminate this, a series of dark images (high, medium and low gain, see section 3.5) are collected under identical experimental conditions, typically performed prior to the actual measurements when both X-ray and optical beams are blocked (i.e., with the both shutters closed). The averaged dark signals (typically over ca. 500 images per gain stage) produce a representative dark frame for each gain stage and memory cell of the detector to remove dark current pedestal, which is then subtracted from each corresponding scattering image to eliminate fixed-pattern noise and electronic offset inherent to the LPD detector, ensuring that only the photon-induced signal is retained in the corrected data before applying the gain constants.

- **Gain correction:** Following dark subtraction, gain correction was applied to account for the amplification factor of a specific gain stage per pixel of the LPD. For each pixel, the appropriate gain map was assigned based on the recorded photon intensity and the corresponding gain threshold. This procedure ensured a uniform scaling of pixel intensities across the entire detector, thereby allowing direct comparison of scattering signals spanning from weak diffuse features to strong Bragg peaks without distortion due to varying gain factors.

- **Geometry correction and assembling the images:** The next step involved assembling the 16 independent detector modules of the LPD into a complete 1M image. For this, the geometry calibration of individual module positions was performed using scattering data from a standard LaB_6 powder sample, whose well-defined diffraction rings provided reference peak positions. By refining the detector parameters (e. g. beam center, module positions and sample–detector distance) against the known LaB_6 pattern, a precise geometry file was generated. This calibration was subsequently applied to all experimental images, enabling the reconstruction of the full 2D WAXS patterns with accurate q-space mapping across the complete detector area.

- **Masking:** After the dark correction, detector masking is very important to remove the unreliable pixels and discontinuous and saturated scattering signals. For this process, a single image is loaded in pyFAI drawmask package [158]. A python script was used to assemble, average and save a representative image. The mask is drawn manually to remove the dead and hot pixels, the shadows from the nozzle, catcher, laser and X-ray beamstops, and other contaminated untrustworthy regions on the detector. This process ensures that only statistically meaningful and physically reliable pixel values are counted for further analysis.

- **Beam center correction:** Accurate determination of the beam center on the detector is essential for reliable calculation of the scattering signal and during the azimuthal integration. During the experiment, slight deviations in the beam position or final detector position can occur due to the mechanical misalignment, sample jet positioning, or beam drift, which should be corrected at this stage to ensure geometric consistency. For this purpose,a single calibration measurement of a crystalline LaB_6 powder was recorded and used solely to generate the geometry file for assembling the 16 LPD modules into a single coherent image. The LaB_6 Debye–Scherrer rings provide the reference peak positions and were therefore employed once to determine module translations, tilts and the nominal sample–detector geometry via the Data Analysis Group calibration scripts (Jupyter Notebook). Precise beam-center determination for the liquid-jet configuration was performed subsequently and independently of the LaB_6 calibration. The beam-center coordinates (x,y) were refined gradually by minimizing the width of the liquid ring width while maximizing its amplitude after the azimuthal integration for each beam center x and y values. These values are then used to correct the beam center for azimuthal integration of all images in the dataset. The mask and the corrected beam center values are applied to all the scans used for further analysis.

6.2 Data reduction

After the raw scattering data have been corrected for detector-specific parameters and experimental geometry, the resulting data undergo a series of data reduction steps to transform them into quantitatively interpretable 1D scattering curves. This process includes azimuthal integration, background subtraction, normalization, converting the corrected intensity patterns into absolute units (electron units) and isolating the structural signal of the solute from the total measured scattering. The following subsections describe these data reduction steps in detail.

- **Azimuthal integration:** The 2D corrected scattering scans are then followed by the azimuthal integration to generate one-dimensional (1D) scattering curves, as a function of the momentum transfer q using the pyFAI integrator.azimuthal module [159]. In this process, the scattering intensity is averaged over concentric rings centered at the calibrated beam center, effectively summing over all azimuthal angles to yield an isotropic radial intensity distribution. This step was performed with the dedicated script from FXE instrument using Python programming language in Spyder interface. The azimuthal integration is particularly suitable for solutions, where structural information is uniformly distributed in all directions. The final curves serve as the basis for structural analysis and are saved in the server of Maxwell cluster as reduced file with individual 1D curves for each image with FXE beamline section for further treatment.

- **Background Subtraction:** Background subtraction of the air scattering is an essential step in the data reduction process to avoid systematic errors when scaling the scattering signals from solution to electron units. For this, air reference signals were recorded under identical experimental conditions (X-ray energy, beam size, detector geometry, exposure) with the liquid jet blocked, dark/gain corrected, and averaged to obtain a representative air background. Then this air background was azimuthally integrated in an identical way and subtracted from all reduced 1D curves to eliminate contributions from air.

- **Normalization and averaging:** To eliminate the effects of fluctuations in incident X-ray intensity, random variations in jet thickness and other acquisition artifacts, each scattering curve was normalized prior to further analysis. The normalization was performed by scaling each $S(q)$ curve to the integrated scattering intensity within a defined normalization range of $q = 2.5$ – 7.5 Å-1. This q-region contains at least one isosbestic point of the expected difference signal, ensuring that the scaling is insensitive to transient structural changes. This normalization compensates for frame-to-frame intensity variations and ensures that all curves represent comparable scattering conditions.

After normalization, multiple scattering curves for the same delay are averaged to improve the signal-to-noise ratio. This averaging is essential because the time-resolved difference signal, $\Delta S(q)$, is typically small compared to the total scattering intensity. The magnitude of this transient signal depends on several factors, including the concentration of the photoexcited species, the extent of the induced structural change, and the X-ray scattering cross-sections of the constituent atoms. In the present case of the $[Au_2(dcpm)_2](PF_6)_2$ complex, despite the relatively low solute concentration (1.5 mM), the large structural rearrangement and the presence of heavy Au atoms result in a pronounced difference signal. By averaging multiple normalized frames per time delay, statistical noise is reduced, which reveals the underlying transient structural changes more clearly allowing for increased analysis precision. This step is particularly important for pump–probe measurements, as the analysis relies on detecting subtle difference signals between the laser-on and laser-off conditions. Therefore, any fluctuations in scattering intensity that are unrelated to the optical excitation must be minimized to ensure that the extracted signal reflects only the photoinduced structural changes.

- **Construction of difference curve:** The structural changes associated with the photoinduced excited state dynamics are generally very small, typically involving atomic displacements less than 0.1 Å. Therefore, oftentimes the corresponding changes in the measured scattering signals are very small, i.e. below 10^{-3}. Additionally, in the particular samples of interest, the concentrations are comparatively very low ranging from 1.5 mM to 5 mM, which means that each solute molecule is surrounded by tens of thousands of solvent molecules. As a consequence, the total scattering signal is highly dominated by solvent contributions. To enhance the structural response of the solute, the analysis is performed on difference scattering signals. These differential scattering curves are constructed by subtracting the scattering signal of the unexcited (laser-off) sample from the excited (laser-on) sample, as a function of both momentum transfer q and time delay t:

$$\Delta S(q,t) = S_{\mathrm{ON}}(q,t) - S_{\mathrm{OFF}}(q) \tag{6.1}$$

A representative comparison between the difference scattering signal and the corresponding S_{on} and S_{off} curves are illustrated in Figure 6.1.

- **Scaling to electron units:** After that, the obtained scattering data were quantitatively scaled from arbitrary units to the electronic units (e.u.). This scaling allows the experimental total scattering curves to be compared with

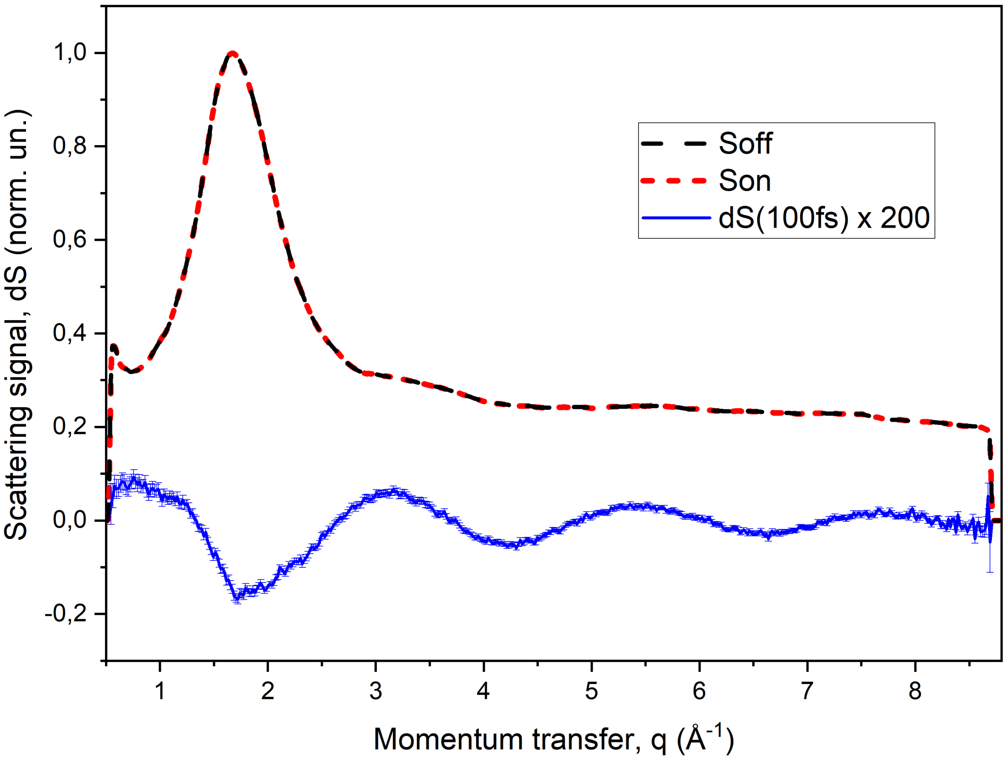

Figure 6.1: The difference X-ray scattering pattern of $[Au_2(dcpm)_2](PF_6)_2$ which was collected at FXE using 17 keV pink SASE X-ray beam from European XFEL. The collected data was reduced according to the procedure described in this section.

theoretical scattering calculated in the high-q region, where the scattering is dominated by independent atomic contributions. The theoretical reference is based on the Debye scattering formalism. In the high-q limit, it is assumed that the solution scattering converges to the coherent gas-phase molecular scattering, as determined by the stoichiometry of the liquid unit cell (one solute and many solvent molecules). The scaling factor obtained in this way from the averaged total scattering curves is applied to the differential scattering data, enabling quantitative extraction of the excited-state population of the solute and the corresponding solvent temperature after fitting with a theoretical model and the experimentally obtained solvent reference signals.

Prior to the model-based extraction of the structural information contained in the difference scattering data, all the above-mentioned steps were performed. All of these steps can vary depending on the X-ray facilities and detector type, making the exact data handling process different for each case. However, the reduction of pump-probe solution scattering data obtained using a prototype detector at a intrinsically unstable MHz XFEL facility in general represent an exhaustive case of possible artifacts that need to be corrected for. The following section focuses on data analysis and structural evaluation of metallophilicity in the binuclear Au complexes.

6.3 Excited state structural analysis

Time-resolved X-ray scattering is a powerful technique to probe transient structural changes in photoexcited molecular systems in solution-phase. Upon excitation by an optical pump pulse, the molecular system undergoes ultrafast structural rearrangements, which are subsequently captured by the X-ray probe as changes in the shape of total scattering signal along the q axis. The direct detection of these small magnitude of structural changes (in sub-Å) is challenging in the total scattering signal due to the presence of the strong background arising from the bulk solvent. To overcome this difficulty, the analysis of the reduced data focuses on the difference scattering signal, $\Delta S(q,t)$, defined as the time-resolved difference between the scattering intensity of the excited state and that of the ground (non-excited) state. This difference scattering signal minimizes contributions from static or unchanging components such as the elastic solvent scattering, elastic and inelastic backgrounds.

The plotted spectrum of $\Delta S(q,t)$ as a function of the momentum transfer, q, encodes structural information about the solute and its surrounding solvent shell as they evolve in time after excitation. The difference curves exhibits structural changes in solution leading to overall change in the shape of the difference curve $\Delta S(q)$ such as arising peaks, valleys and oscillations with frequency, phase and amplitude, which reflect changes in interatomic distances, bond angles, and solvation structure. These signals can originate from several sources:

- structural rearrangements within the solute molecule (e.g., bond and interatomic distance shortening or elongation, ligand displacement) - this is the most crucial component for this particular study of the molecular chemical dynamics in solution of metallophilic complexes,
- changes in the solvation environment in response to electronic re-distribution and solute structural changes, and
- changes in the bulk of the solvent due to energy dissipation and hydrodynamic response.

6.3.1 Result of $[Au_2(dcpm)_2](PF_6)_2$

Using the optical pump of 266 nm for$[Au_2(dcpm)_2](PF_6)_2$ complex in acetonitrile solvent, the WAXS data were collected from FXE instrument at European XFEL and then treated with all the necessary steps required to understand and extract the information contained within the data. For fitting of the excited state structure of $[Au_2(dcpm)_2](PF_6)_2$ complex in solution, the refined ground state structure from the solution phase EXAFS measurement was utilized (section 5.1) and using this reference, the DFT calculated excited state structures were employed to extract the structural information of the $[Au_2(dcpm)_2](PF_6)_2$ complexes.

Figure 6.2 presents the time-resolved difference scattering signals of $q\Delta S(q,t)/S(q)$ vs. q, collected using 17 keV X-rays energy at various pump–probe delay times ranging from –0.25 ps to 1.25 ps. Each curve in the figure corresponds to a specific delay time after photo-excitation, as indicated on the right-hand side of the plot. The plotted signal in the spectrum represents the differential scattering intensity, normalized by the static scattering profile, and multiplied by the momentum transfer q. This representation enhances the visibility of oscillatory features of the signal that primarily comes from transient change in the solute structure. The observed transient signals arise from the structural rearrangements in the solute molecule, particularly associated with changes in the gold-gold distance due to the heavy gold centers upon photo-excitation.

Before time zero, i.e. at negative pump-probe delays (–0.25 ps and –0.10 ps), the signal is basically flat, which confirms the absence of any optical pump-induced structural changes within the solute molecules or detection artifact in the measurements. With a closer inspection of the time-resolved difference scattering signals in Figure 6.2, the distinct oscillatory features are revealed emerging within the first 50 femtoseconds after photo-excitation. These oscillations begin to emerge in the q-range between ~ 1.5 and 8.5 Å^{-1}, reflecting ultrafast structural rearrangements triggered by femtosecond

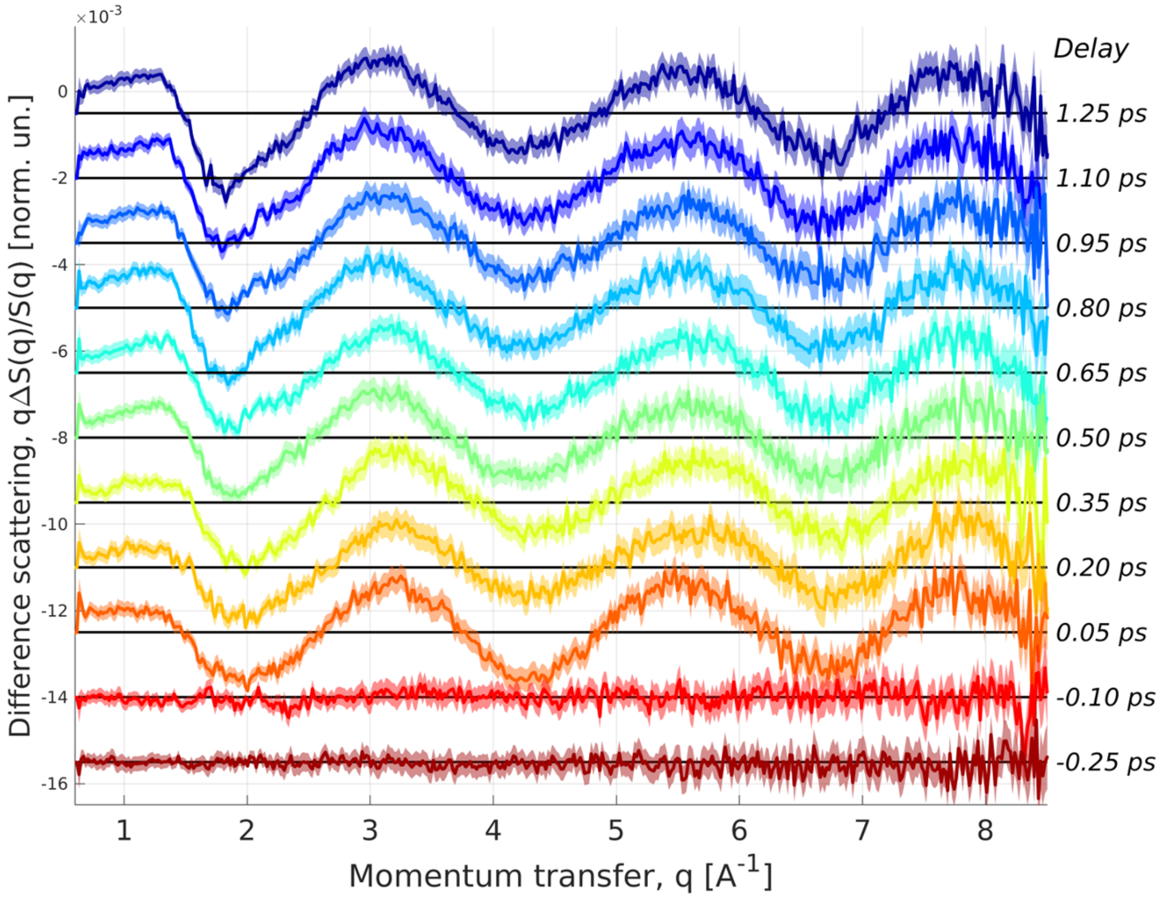

Figure 6.2: Difference scattering signals vs. momentum transfer of liquid $[Au_2(dcpm)_2](PF_6)_2$ in acetonitrile for selected time delays. From top to bottom, the time delay decreases and the signals show different features. Shaded areas in the plot represent experimental standard deviation extracted from statistical average.

excitation pulse. The rapid appearance of these oscillations at early time delay which is as early as 0.05 ps, suggests an immediate structural response involving Au···Au distance modulation or a concerted movement of ligands around the gold centers with only minimal contribution from signals related to changed in the bulk solvent.

As the system evolves from 0.05 to 1.25 ps, the magnitude and shape of these oscillations change over time, indicating dynamic structural modifications within the complex. The peaks shift slightly with increasing delay, indicating the progression of structural relaxation towards another excited state situated between the ground state and highest- level excited state. The difference signal amplitude increases up to approximately 1.25 ps, after which the response continues to grow as the bulk solvent contribution becomes more pronounced. This behavior reflects the onset of solvent thermalization and the establishment of thermodynamic equilibrium within the probed volume. These features will be quantitatively analyzed in the following chapter to extract time-resolved structural parameters and interpret the excited-state dynamics of the system. Moreover, the negative amplitude of the peak at q-range of ~ 1.8 and 2.2 Å^{-1} also increases with increasing time delay, reflecting the bulk solvent heating or potential rise of local density in the nearest solvation shells [160]. With longer time delay, the surrounded solvent molecules get enough time to get thermalised and the heating of the solvent molecules changes the density, showing features in this low q-range difference scattering signals.

For better understanding of the peak positions and to complement the line plots of the difference scattering curves at individual delay times, a two-dimensional color-map is shown in Figure 6.3. This 2-D map represents the normalized differential signal as a function of momentum transfer q and time delay, enabling the global visualization of the structural evolution within the photoexcited $[Au_2(dcpm)_2](PF_6)_2$ complexes in acetonitrile. This representation enables a more comprehensive view of the temporal evolution of the scattering signal across the entire q-range. Here in the map, red and blue regions represent difference signal, positive and negative, respectively.

A closer inspection of the map reveals that distinct vertical features appear immediately after time zero around $q = \sim 2.0, 4.0$ and 7.0 Å^{-1}, indicating that specific interatomic distances in the $[Au_2(dcpm)_2](PF_6)_2$ complexes undergo time-dependent modulation. The oscillatory components exhibit a slight shift in position with time delay, suggesting that the structurally-sensitive high-q component of the signal evolves according to the actual transient structural change in the complex. Moreover, the amplitude of the oscillations in q also appears periodically modulated over time.

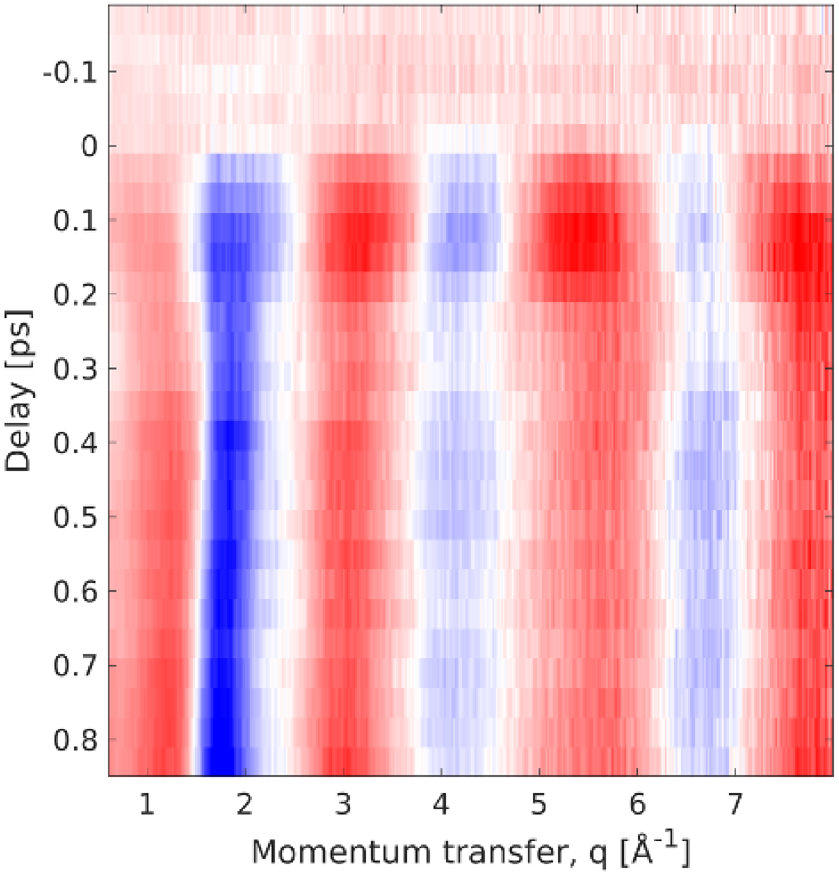

Figure 6.3: Difference scattering signals vs. momentum transfer in 2-dimensional (2D) mapping for $[Au_2(dcpm)_2](PF_6)_2$ in acetonitrile.

This periodic amplitude modulation is a characteristic signature of a vibrational wavepacket forming on an excited-state potential energy surface. Moreover, the changing frequency may indicate that the corresponding average bond length evolves dynamically due to either contraction or expansion of the Au···Au distance or surrounding ligand rearrangement. The variation in signal intensity, alternating between high and low amplitude regions, reflects the transient dynamics and dephasing of structural configurations.

All these initial observations suggest that further exploration via structural refinement and model fitting are required to provide clear conclusion on ultrafast structural rearrangements involving coherent Au-Au bond length modulations coupled with solvent reorganization. Additional structural refinement of the $[Au_2(dcpm)_2](PF_6)_2$ complex are described in Section 7.1.

6.3.2 Result of [Ag_2(dcpm)$_2$](PF$_6$)$_2$

Time-resolved WAXS measurements of [Ag_2(dcpm)$_2$](PF$_6$)$_2$ in acetonitrile were carried out at the ID09 beamline of ESRF using 266 nm optical excitation. The collected data were subsequently processed through all standard reduction and correction steps to isolate the solute response and enable structural interpretation. For preliminary fitting with experimental data, ground-state (GS) and excited-state (ES) molecular structures were obtained from DFT calculations performed with the ORCA package. The optimized structures used for the simulations are presented in the Appendix B.

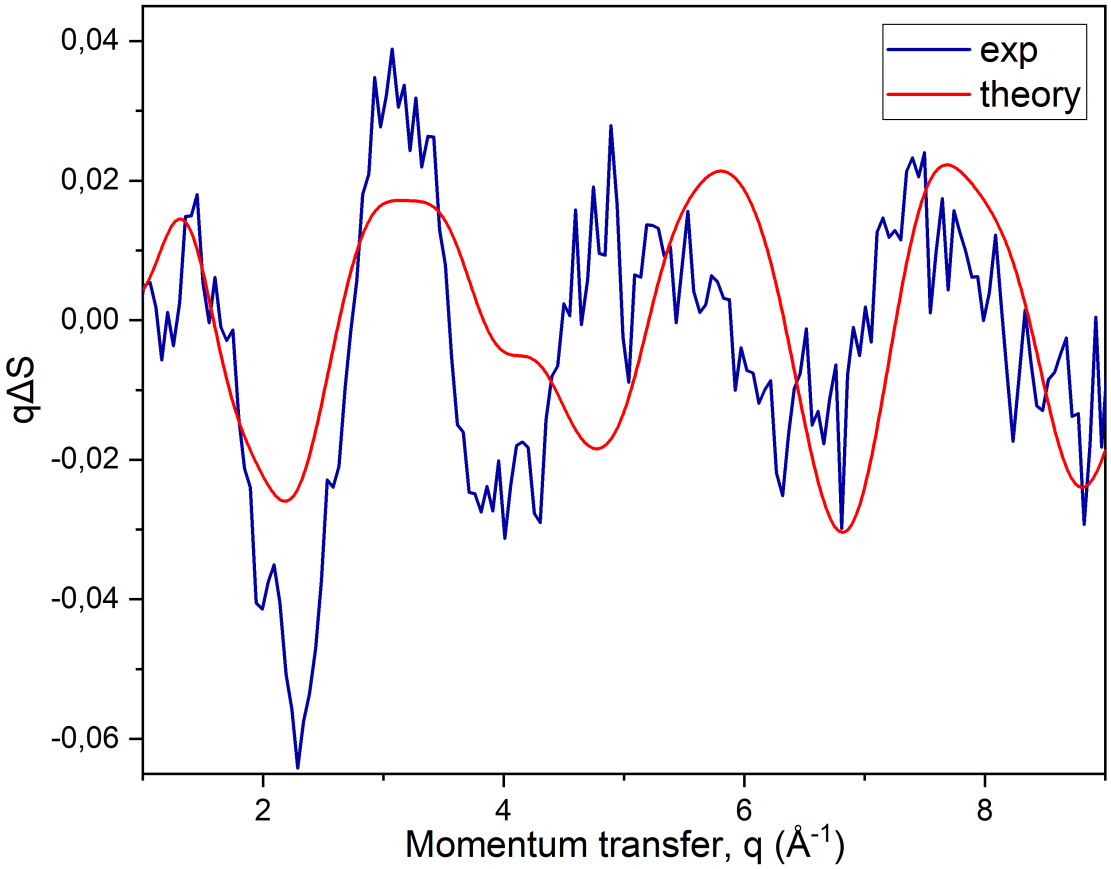

Figure 6.4: Experimental difference scattering signal of [Ag_2(dcpm)$_2$](PF$_6$)$_2$ at 200 ps after 266 nm excitation (blue) compared with theoretical scattering response (red).

Figure 6.4 shows the experimental difference scattering signal,$q\Delta S$ (t=200 ps) of 3 mM [Ag_2(dcpm)$_2$](PF$_6$)$_2$ complex in acetonitrile (blue) overlaid with a simulated signal (red). The experimental curve represents the solute response after subtracting the solvent/heating contribution obtained from a dye reference, so the residual structure primarily reflects photoinduced changes in the [Ag_2(dcpm)$_2$](PF$_6$)$_2$ complex and its immediate solvation shell at 200 ps. Both of the curves display a clear oscillatory pattern with nodes and antinodes and capture several notable phase relationships spaced across the measured q range. This alignment of positive and negative lobe indicates that the interatomic distance changes are consistent with the experiment and also encoded in the simulation. A noticeable amplitude and shape mismatches are present in the mid-q region ($\sim$ 4–6 $Å^{-1}$) and at higher q where the experiment shows sharper structure and more noise.

The present results demonstrate that the experimental signal captures the structural response of the solute and is consistent with an excited-state geometry involving argentophilicity-sensitive rearrangements in the Ag-Ag distance. To refine the comparison into a fully quantitative model, further analysis following the approach established for the $[Au_2(dcpm)_2](PF_6)_2$ complex is required. A more detailed investigation, including systematic fitting and solvent–solute contributions, is planned for future work and is therefore not included in this thesis.

6.3.3 Result of $[Cu_2(dcpm)_2](PF_6)_2$

Similar to the metallophilic $[Au_2(dcpm)_2](PF_6)_2$ and $[Ag_2(dcpm)_2](PF_6)_2$ complexes, $[Cu_2(dcpm)_2](PF_6)_2$ was investigated in acetonitrile solution. To characterize the transient structural dynamics, time-resolved WAXS measurements were performed at the ID09 beamline of ESRF with 5 mM $[Cu_2(dcpm)_2](PF_6)_2$ in acetonitrile using 320 nm optical excitation. For the preliminary fitting of the experimental data, the ground-state (GS) and excited-state (ES) molecular structures were derived from DFT calculations carried out using the ORCA package. The optimized structures used for the simulations are presented in the Appendix B.

Figure 6.5 presents the experimental difference scattering signals (violet) recorded at 200 ps delay, together with the simulated scattering response (red). The experimental signal displays a characteristic oscillatory pattern over the entire q-range, similar to other two analogues complexes. These features are indicative of a coherent structural response involving Cu-Cu bond distances and ligand re-orientations. The comparison with theoretical curve reproduces the phase and amplitude of the main oscillations, validating the assignment of a transiently shortened Cu$\cdots$Cu distance in the excited state.

A complete quantitative interpretation will require additional analysis based on the framework previously developed for the $[Au_2(dcpm)_2](PF_6)_2$ complex. Such investigation, including systematic fitting procedures and explicit treatment of solvent–solute interactions, remains a subject for future work rather than part of this thesis.

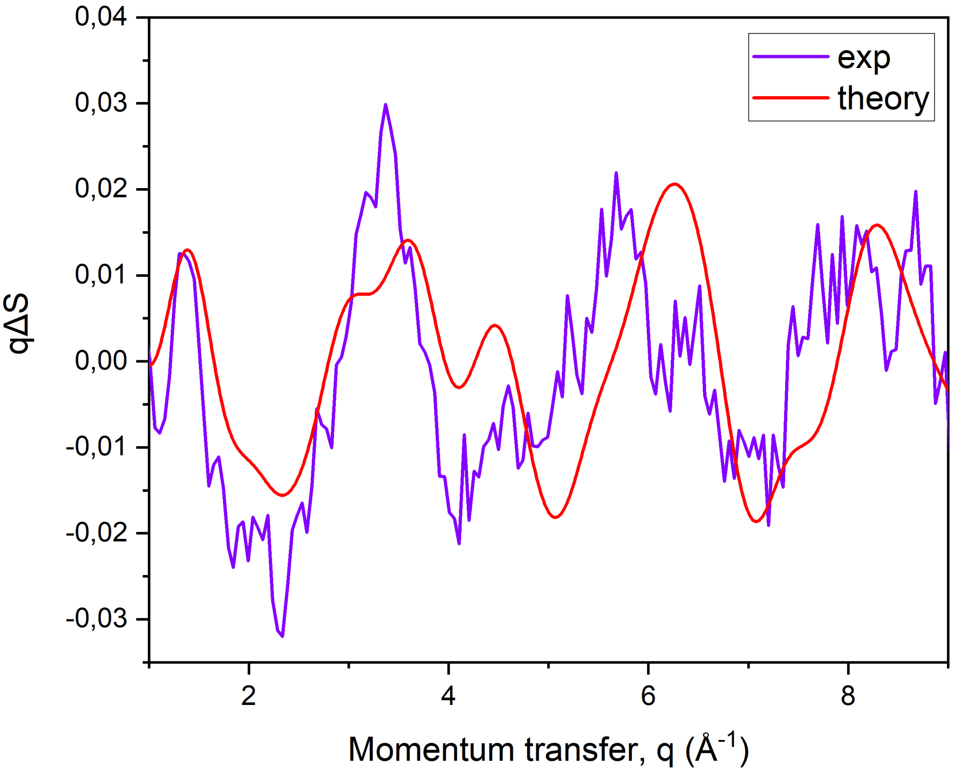

Figure 6.5: Experimental difference scattering signal of $[Cu_2(dcpm)_2](PF_6)_2$ at 200 ps after 266 nm excitation (violet) compared with theoretical scattering response (red).

6.3.4 Result of [Au_2(pnnp)$_2$]Cl_2

For [Au_2(pnnp)$_2$]Cl_2 complex in acetonitrile solution, the optical pump of 266 nm was utilized to obtain the WAXS signals at an X-ray photon energy of 17 keV from FXE instrument. Similar to the previous analysis of [Au_2(dcpm)$_2$](PF_6)$_2$ complex, the time-resolved difference scattering signals of [Au_2(pnnp)$_2$]Cl_2 complex were displayed in Figure 6.6. This figure shows the time-resolved difference scattering signals of $q\Delta S(q,t)/S(q)$ vs. q, collected across a series of pump–probe delay times ranging from –0.60 (pre-excitation baseline or negative delay) ps to 0.80 ps (following optical excitation). The differential scattering curves at negative delay times (–0.60 ps to –0.20 ps) shows no significant features, which confirm the stability of the ground-state reference and ensure that the observed structural dynamics are purely photoinduced.

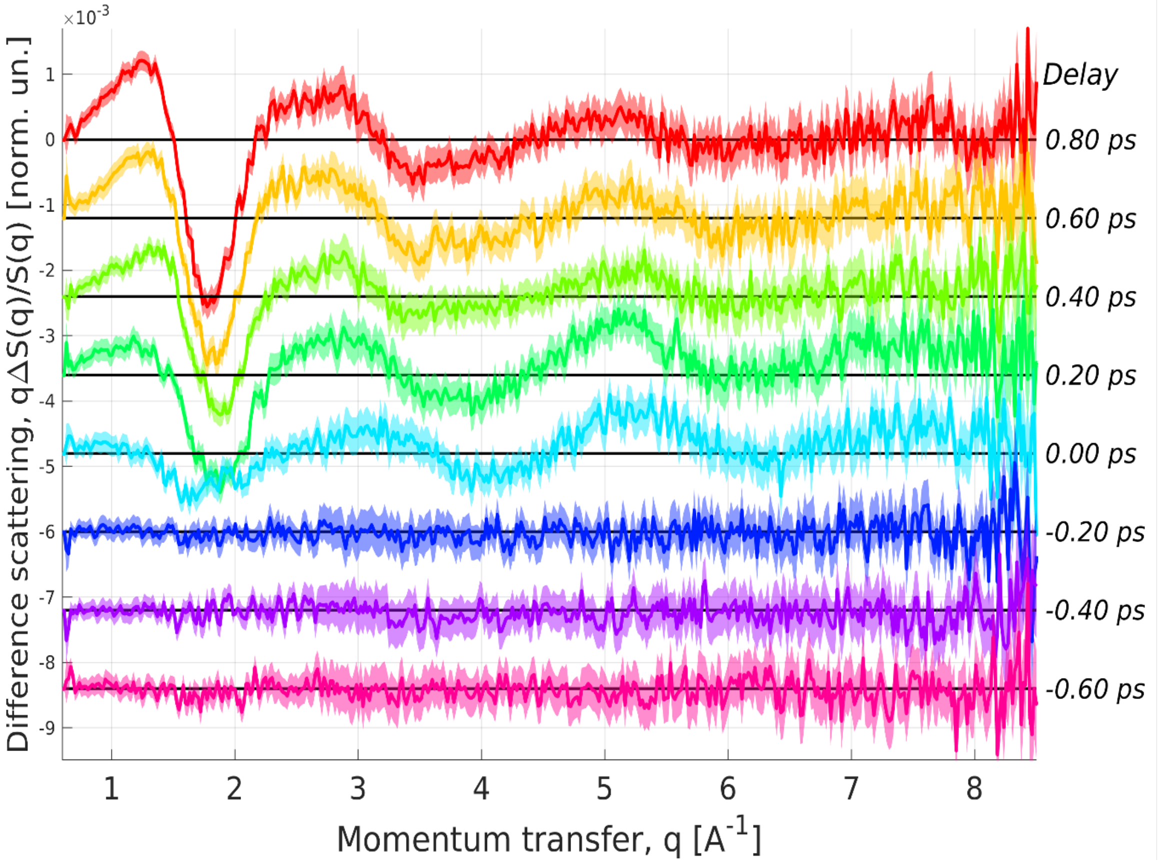

Figure 6.6: Difference scattering signals vs. momentum transfer of [Au_2(pnnp)$_2$]Cl_2 in acetonitrile for selected delays. From top to bottom, the time delay decreases.

Upon excitation with the optical pump-pulse, clear evolution of the difference signals within the first few femtoseconds reveal signatures of coherent vibrational dynamics, similar in nature to those observed for the [Au_2(dcpm)$_2$](PF_6)$_2$ complex, particularly within the q-range of $\sim$ 3.1 and 7.2 Å^{-1}. A prominent negative peak centered around

1.9 Å^{-1} arises after about 200 fs delay time and this feature gradually evolves in both amplitude and position with increasing delay time. This part of difference scattering signal as a function of momentum transfer is responsible of the solvation effects associated with excited-state relaxation processes.

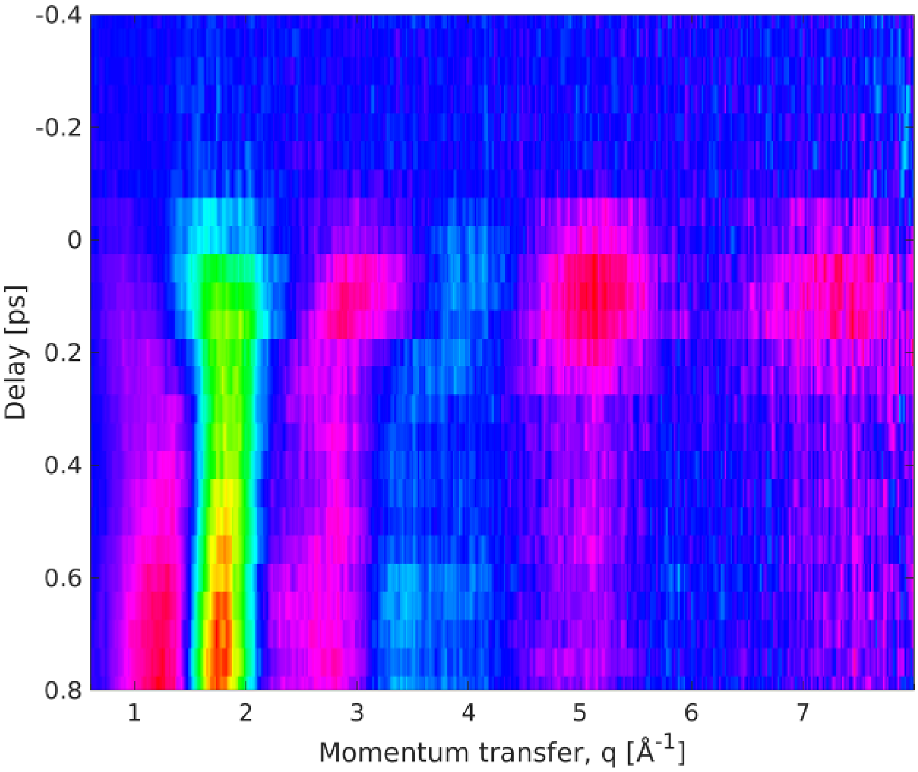

Figure 6.7: Difference scattering signals vs. momentum transfer in 2-dimensional (2D) mapping for $[Au_2(pnnp)_2]Cl_2$ in acetonitrile.

Interestingly, with increasing time delay from 0.20 to 0.80 ps, the magnitude and shape of these oscillations responsible for the solute structural rearrangement dissolve over time, indicating dynamic structural changes within the complex. At the early delay time of 0.20 ps, the amplitude of the oscillatory features in the difference scattering signal reaches its maximum, indicating ultrafast formation of the excited state in the solute. As the delay progresses to longer timescales (0.40 to 0.80 ps), a gradual decrease of the oscillation amplitude is observed, particularly in the high-q region (above 6 Å^{-1}). By 0.80 ps, these high-frequency oscillatory components have nearly disappeared, suggesting significant reduction the structural signal either due to relaxation to the ground state or another excited state with much smaller structural change.

The two-dimensional colormap, presented in Figure 6.7, provides a better understanding of the difference scattering signals at individual delay times for $[Au_2(pnnp)_2]Cl_2$ complex in acetonitrile. The vertical axis corresponds to time delay between optical-pump and X-ray-probe (from –0.40 to 0.80 ps), while the horizontal axis indicates the momentum transfer q (0.5 to 8 $Å^{-1}$). The blue/cyan color indicates the negative difference signals and the pink color is for positive difference signals in the colormap, highlighting transient structural changes upon photoexcitation. As explained before, the signal prior to time zero shows minimal variation, confirming the absence of any pump-induced structural rearrangement.

Immediately after photoexcitation at time delay 0.20 ps, strong intensity features appear in the low to mid q-range, particularly around $q = \sim 2.6, 5.0$ and 6.8 $Å^{-1}$. The most intense transient is observed around 0.20 ps. This sharp, fast signal suggests the formation of a vibrational wavepacket initiated by an impulsive change in the Au–Au distance, similar to what was observed in the $[Au_2(dcpm)_2](PF_6)_2$ complex. Notably, the overall signal gradually decays as the delay increases, indicating vibrational cooling or population redistribution to a more relaxed and long-lived excited-state or partially to the ground state. Another point to mention that the solvent signal at delays longer than 1 ps dominates the overall signal. The presence of temporally evolving signals in the high q-region with weaker intensity, suggests structural modulations involving ligand reorientation or solvent shell rearrangement around the photoexcited complex.

The initial observations from the 2D visualization suggest that the $[Au_2(pnnp)_2]Cl_2$ complex undergoes ultrafast structural rearrangements, initiated within 100 fs, involving Au-Au bond length modulations coupled with solvent reorganization, details of this rearrangement are explored via structural refinement and explained further in Section 7.2.

Chapter 7

Discussion

This chapter presents a comprehensive analysis of the reduced data and discussion of the time-resolved X-ray scattering data and structural refinement results for the two bimetallic gold complexes, $[Au_2(dcpm)_2](PF_6)_2$ and $[Au_2(pnnp)_2]Cl_2$. As explained in the previous chapter, both EXAFS and WAXS measurements were performed on the $[Au_2(dcpm)_2](PF_6)_2$ complex, while WAXS was employed for the investigation of the $[Au_2(pnnp)_2]Cl_2$ complex. The analysis of the WAXS data is performed by considering the main contributions of the scattering signal - the solute and solvent terms, whereas the cage term in these case is very weak, as shown in Section 7.1. This chapter focuses on the in-depth interpretation of the extracted time-resolved difference scattering data, combined with structural refinement, structural dynamics and potential energy surface interpretation for $[Au_2(dcpm)_2](PF_6)_2$, followed by MD simulations results summary for the cage term. A similar analysis for $[Au_2(pnnp)_2]Cl_2$ is also included, highlighting the nature of coherent vibrational wavepackets, solvent response, structural refinement, structural dynamics and potential energy surface interpretation.

7.1 Excited state Aurophilicity in $[Au_2(dcpm)_2](PF_6)_2$

The initial analysis of difference scattering signals as a function of individual time delays was described in Section 6.3.1. The plotted signal in Figure 7.1 was derived by integrating the absolute difference scattering signals in the q-range 3.4-7.5 $Å^{-1}$. The blue circles with error bars (denoted as Data FOM) show clear oscillatory behavior, superimposed on a rapidly rising signal. The following interpretation can be proposed. Immediately after photoexcitation, the Au–Au bond undergoes contraction, followed by an oscillatory response as the molecular system moves back and forth around a new equilibrium position, reflecting the formation and propagation of a structural vibrational wavepacket. These oscillations represent a structural wavepacket with a vibrational period of approximately 350 fs, corresponding to the motion of the Au atoms as they transiently move closer together upon excitation. Such wavepacket dynamics indicate coherent excitation and evolution on the potential energy surface of the excited-state complex.

Further quantitative analysis of these oscillations shows an exponential damping envelope with a decay constant of approximately 240 fs. The damping constant suggests rapid vibrational cooling, which can be interpreted physically in two ways. Firstly, it can be vibrational cooling within the initially excited singlet state, most likely associated with rapid redistribution of vibrational energy to the surrounding solvent molecules. Alternatively, it can also indicate ultrafast intersystem crossing (ISC), where the initial excited singlet state transitions to a longer-lived triplet state within hundreds of femtoseconds. Distinguishing between these mechanisms typically requires complementary spectroscopic studies or advanced theoretical modeling since the scattering technique only reports on the transient structural evolution.

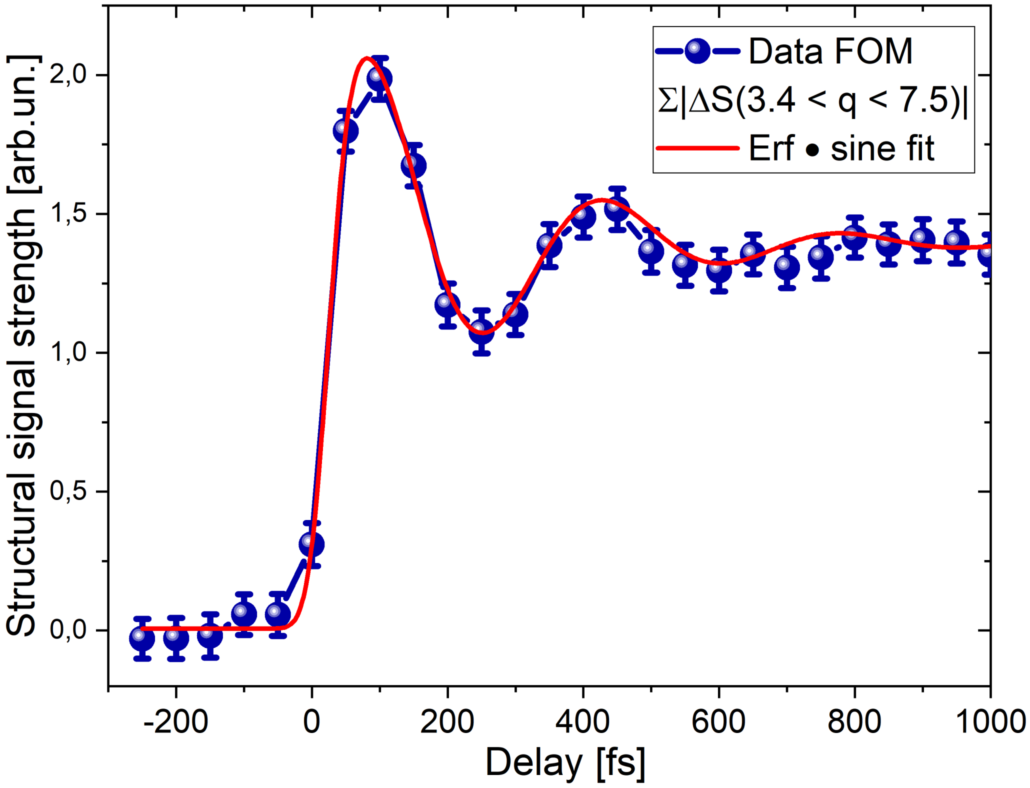

Figure 7.1: Difference scattering signals integrates in the q-range from 3.4 - 7.5 Å^{-1}, collected at FXE beamline for [Au_2(dcpm)$_2$](PF$_6$)$_2$ in acetonitrile solvent.

The red line in the plot represents a fit using an error function (erf) combined with a damped sine function, capturing both the rapid rise and the coherent oscillatory behavior of the structural signal. This model fit confirms the presence of a well-defined, coherent structural wavepacket formation. This process resolves these dynamics of femtosecond-scale structural rearrangements in solution-phase, which offers insights into the excited-state potential energy landscape of the [Au_2(dcpm)$_2$](PF$_6$)$_2$ complex and its early-time relaxation pathways.

Structural Refinement from Difference Scattering Data

With the high photon energy (17 keV) experimental configuration, structural refinement of the $[Au_2(dcpm)_2](PF_6)_2$ complex was carried out to quantitatively interpret the time-resolved difference scattering signals. For the structural refinement, previously optimized ground-state structure from EXAFS in solution phase was utilized as the starting point (Section 5.1.3). The density functional theory (DFT) was used to simulate the excited state structure at different fixed Au-Au distances in solution phase and then compared by fitting with the experimentally obtained difference scattering signals ($q\,\Delta S(q,t)$) at different time delays.

Figure 7.2 shows refined structural fits at three representative pump–probe delay times: 100 fs, 200 fs, and 100 ps. These refined scattering curves exhibit the comparison between experimental scattering data (black) with error bars, simulated total fitted scattering (pink, red, and light blue, respectively), and isolated solute scattering contributions (blue, green, and yellow, respectively) for each delay time. The high quality fitting of these scattering signals at various time delays demonstrates that the applied refinement procedure accurately captures the underlying structural dynamics. The solute terms substantially account for the oscillatory features in the experimental signals in the mid- to high-q range.

Analysis of the refined structural parameters at different delay times reveals a consistent shortening of the Au–Au distance immediately after photoexcitation. The observed shortening of the Au–Au distance is particularly evident at early delays (100 fs), highlighting an ultrafast initial structural response. This coherent contraction and oscillation of the Au–Au bond corresponds to a vibrational wavepacket traversing the excited-state potential energy surface. The extracted Au–Au distance change of -0.113 Å for 100 fs time delay, as concluded from fitting, indicate a rapid bond contraction that relaxes with time. The extracted Au–Au distance change at 200 fs time delay is around -0.131 Å which is comparatively larger than 100 fs. At 100 ps time delay, the Au–Au distance change is around -0.093 Å which is comparatively smaller than 100 fs and 200 fs, suggesting that the structure has relaxed toward a geometry associated with the long-lived triplet-state.

The residual deviations between experimental and fitted scattering curves in the low-q range indicate additional scattering contributions beyond the modeled intramolecular rearrangements. These deviations strongly indicate the contributions from solvent reorganization effects, particularly acetonitrile solvent molecules rearranging around the excited solute complex. For particular analysis of these solvent effect, the advanced ab-initio non-equilibrium molecular dynamics (MD) simulations are required. However,

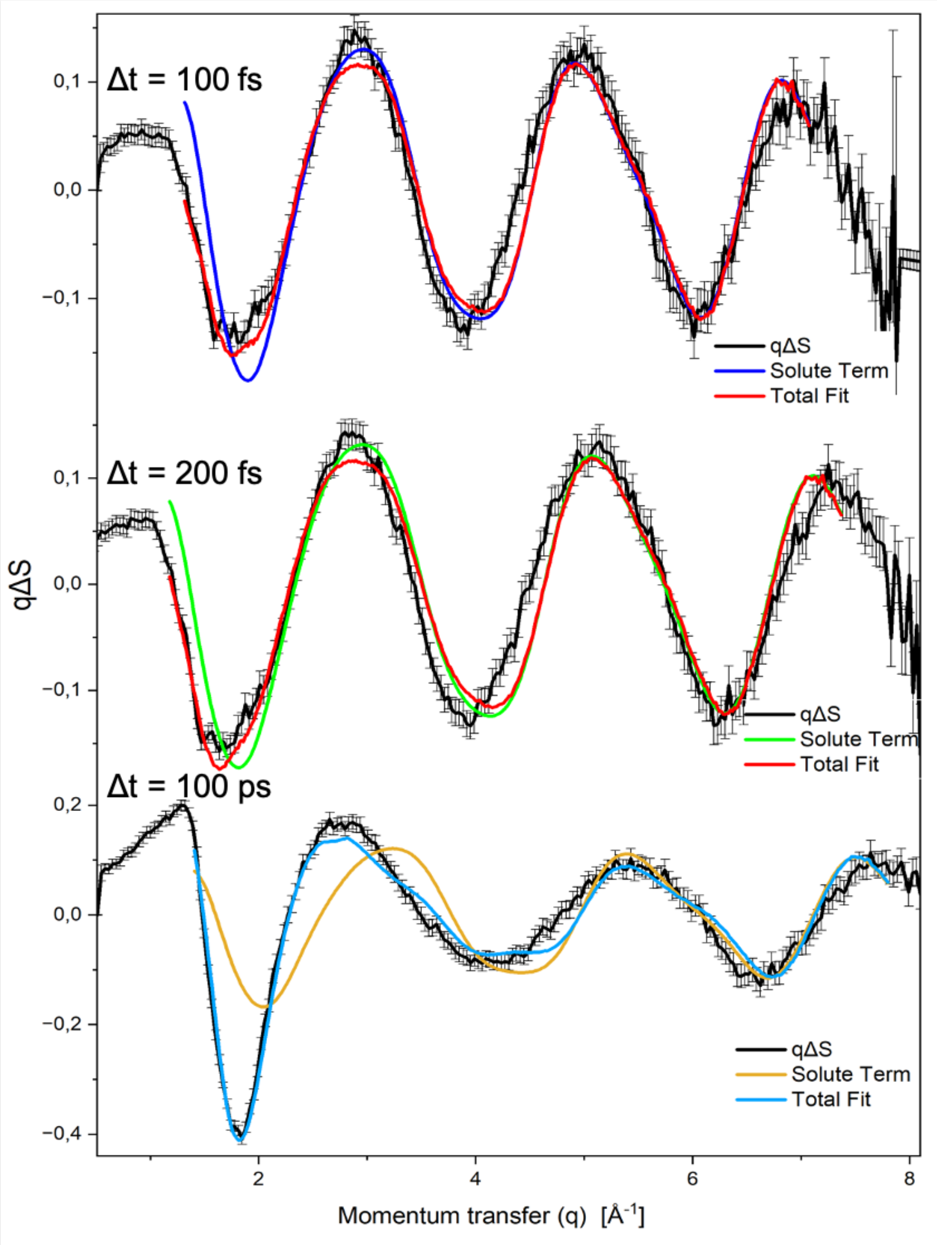

Figure 7.2: Integrated difference scattering signals $q\,\Delta S$ as a function of momentum transfer q at different pump-probe delay time, collected at FXE beamline for $[Au_2(dcpm)_2](PF_6)_2$ in acetonitrile solvent. More details are described in the main text.

already preliminary classical MD simulations allow to approximate the expected signals as briefly described in Section 7.1. The structural fitting above was performed in the high q range (above 1.7 $Å^{-1}$), where the cage term does not contribute much due to the relevant length scales.

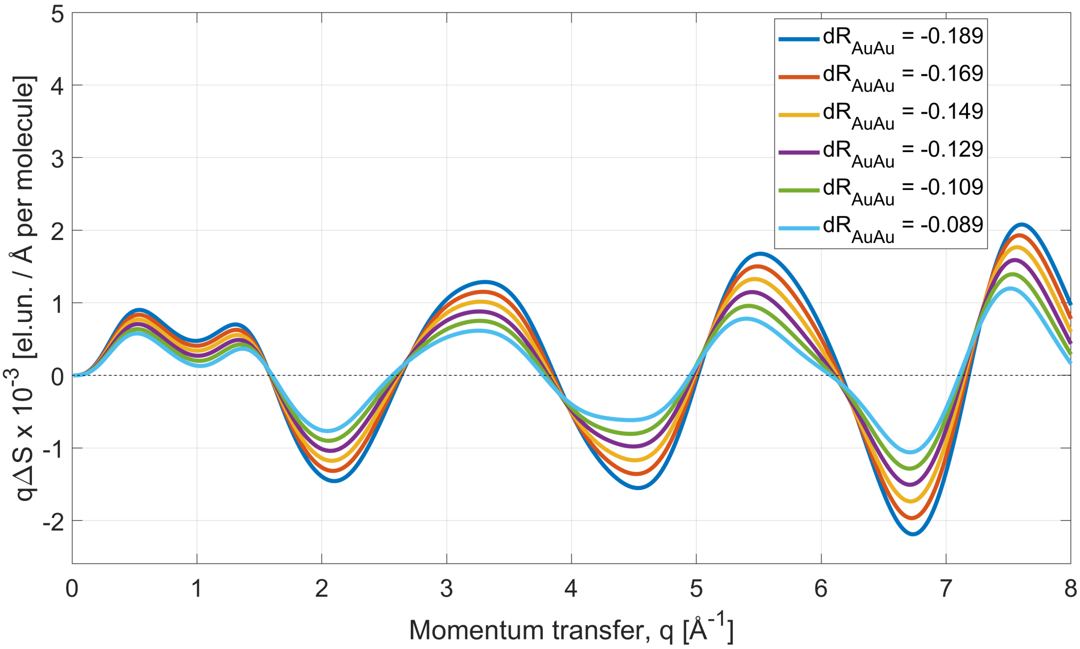

Figure 7.3: Simulated difference scattering signals for the $[Au_2(dcpm)_2](PF_6)_2$ complex at varying Au–Au distances in the excited state.

To further illustrate the structural optimization approach described above, the effect of different Au–Au bond distances (dR_{AuAu}) on the calculated difference scattering signals in the excited state of the $[Au_2(dcpm)_2](PF_6)_2$ complex are illustrated in Figure 7.3. By systematically scanning a range of Au–Au bond distances from -0.089Å to -0.189 Å, distinct changes in the oscillatory features of the simulated qΔS(q) patterns are observed. These variations demonstrate the high sensitivity of scattering signals to subtle changes in metal–metal distances, particularly in the mid- to high-q regime ($2<q<8$ $Å^{-1}$), where the scattering signal strongly reflects intramolecular structural rearrangements. This behavior highlights that time-resolved WAXS is not only capable of detecting the presence of bond contractions but also provides a quantitative means of resolving metal–metal bond dynamics in solution with sub-Å precision.

Potential Energy Surface and Excited State Dynamics

Based on the structural and experimental refinement, the schematic potential energy diagram is proposed as shown in in Figure 7.4 that illustrates a hypothetical interpretation of the excited-state dynamics of the $[Au_2(dcpm)_2](PF_6)_2$ complex in acetonitrile solvent. Initially, the molecule resides in the ground state, characterized by a relatively large Au–Au distance. Upon optical excitation (denoted as blue vertical arrow in the figure 7.4), the whole molecule gets excited to the first singlet excited state labeled as S_1 or $^1[5d\sigma^*6p\sigma]$, which exhibits a significantly shorter equilibrium Au–Au distance compared to the ground state. Due to the sudden shift in equilibrium geometry, the excited molecule undergoes coherent vibrational motions along the excited singlet-state potential energy surface, resulting in the observable structural wavepacket dynamics.

As per the structural experimental results, the excited-state wavepacket undergoes coherent oscillations with a period of approximately 350 fs (Figure 7.1). These structural oscillations reflect a rapid contraction and subsequent relaxation of the Au–Au bond distance, corresponding to approximately one and a half oscillations along the excited singlet-state potential energy surface. During this ultrafast evolution, the wavepacket experiences rapid damping, characterized by a decay constant of roughly 240 fs. This rapid damping could be either due to vibrational cooling or, relaxation through an ultrafast intersystem crossing from the initially populated singlet excited state to a nearby lower-energy triplet state, labeled as T_1 or $^3[5d\sigma^*6p\sigma]$. This T_1 is expected to be the long-lived luminescent state with slightly longer Au-Au distance compared to the singlet as also supported by long delay results and by ORCA simulations.

The predicted intersystem crossing is consistent with the dynamical behavior observed in analogous binuclear complexes, particularly [Pt]-based systems, where similar ultrafast singlet–triplet transitions have been reported. This is further supported by the experimentally refined Au–Au distance at long delay times, which shows a longer distance relative to the initial distance, as well as by the DFT results obtained from ORCA simulations. Together, these detailed experimental observations and structural refinements strongly support the proposed excited-state pathway, which provides quantitative insights into the shortening of the Au–Au distance compared to the initial ground state and the ultrafast structural relaxation processes in solution-phase bimetallic $[Au_2(dcpm)_2](PF_6)_2$ complex.

Molecular dynamics simulation on $[Au_2(dcpm)_2](PF_6)_2$

The preliminary molecular dynamics (MD) simulations were performed in the classical way to investigate the role of solvent–solute interactions ('cage' term) in shaping the scattering response of the $[Au_2(dcpm)_2](PF_6)_2$ complex in acetonitrile solution. The simulations were carried out on the Maxwell cluster using the GROMACS package. A cubic simulation box of $10 \times 10 \times 10$ nm^3, corresponding to equilibrium density, was filled with 11,530 acetonitrile (MeCN) solvent molecules and two PF_6^- counter ion molecules to ensure charge neutrality. Both the ground-state (GS) and excited-state (ES) structures of the dimer were included as rigid solutes, strongly constrained to their DFT-

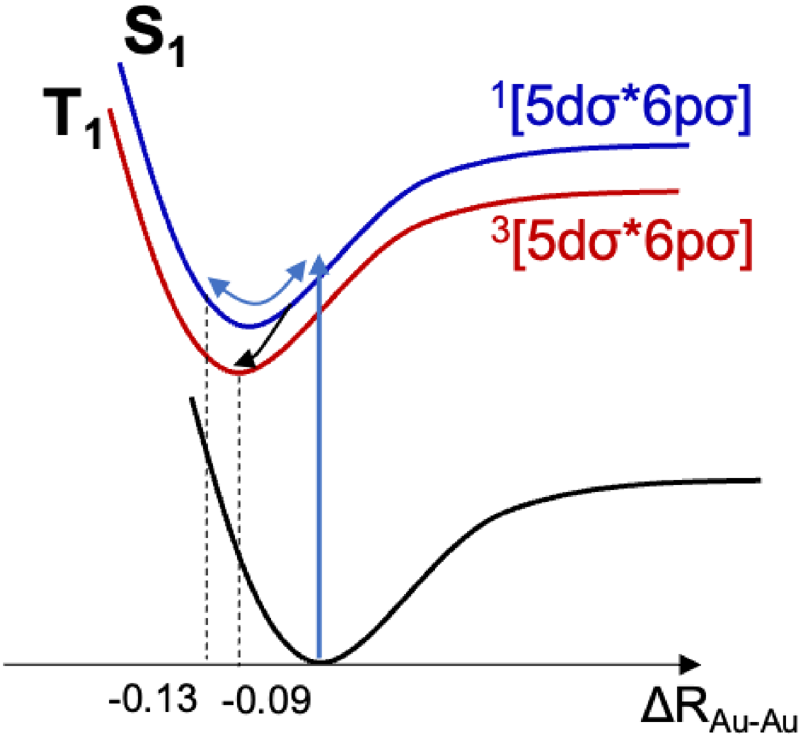

Figure 7.4: Potential energy surface diagram for $[Au_2(dcpm)_2](PF_6)_2$ in acetonitrile solvent. After the excitation with photon, the electron goes to the excited singlet state and then it moves to the excited triplet state and finally relaxes to the ground state.

optimized geometries, while solvent molecules were fully flexible. As the generalized Amber force field (GAFF2) lacks parameters for gold, a practical approximation was implemented by substituting gold with iodine, which preserved the steric representation and approximate scattering characteristics of the heavy atom by keeping the solute highly constrained during the trajectory. The system was initially equilibrated at constant temperature of 293.15 K for 2 ns with periodic boundary conditions in all three dimensions. After that the simulation trajectory was run for 20 ns and then used for sampling the pair-wise atomic radial distribution functions (RDFs). The same simulation procedure was applied for both the ground (S0) and the excited (T1) states.

The trajectories obtained from the MD runs were analyzed to extract solvent structural information, including RDFs between selected solute atom types and all relevant solvent atom types. In total, 12 distinct RDFs were evaluated (four solute atom types: Au, P, C, H; and three solvent atom types in MeCN: C, N, H), resulting in 24 RDFs when considering both ground- and excited-state trajectories. These RDFs provide atomistic insight into how the solvation structure reorganizes upon electronic excitation. For simplicity of interpretation, the RDFs discussed here are presented as combined functions, where the contributions from all solvent atoms were averaged for each solute atom type. This approach highlights the principal solvation characteristics around different parts of the complex while retaining the essential structural information. The following combined RDFs were therefore employed for subsequent analysis:

- $g_{\mathrm{Au-MeCN}}(r)$: distances from each Au atom in $[Au_2(dcpm)_2]^{2+}$ to MeCN (treated as one site—either center-of-mass or pooled solvent atoms, depending on your implementation).

- $g_{\mathrm{P-MeCN}}(r)$: distances from each phosphorous (phosphine) atom to MeCN.

- $g_{\mathrm{C-MeCN}}(r)$: distances from ligand carbon atoms (dcpm framework) to MeCN.

- $g_{\mathrm{H-MeCN}}(r)$: distances from ligand hydrogens to MeCN.

From these RDFs, the solvent-induced cage contribution in scattering (dS_{cage}) was computed following established methods described in [160]. The dS_{cage} term accounts for changes in the solvation environment between the GS and ES states and is critical for separating solvation shell responses from the intrinsic solute scattering signal dS_{solute}. The calculated dS_{cage} reflects how different regions of the complex modulate the solvent reorganization upon photoexcitation, thereby providing a detailed picture of the solvation dynamics surrounding the dimer complex.

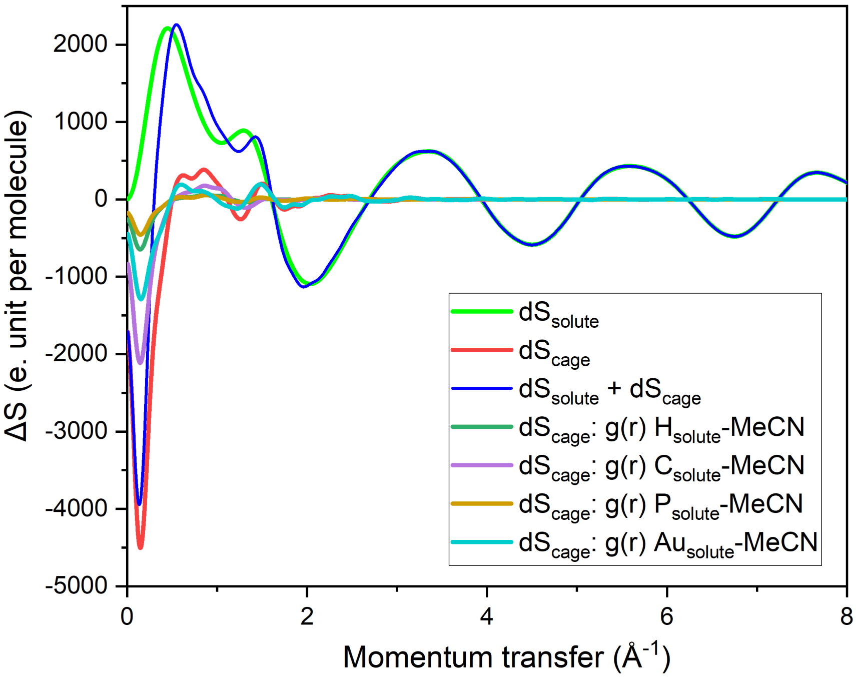

Figure 7.5: Simulated difference scattering signals (ΔS) for the $[Au_2(dcpm)_2](PF_6)_2$ in acetonitrile solvent, obtained from molecular dynamics simulations.

Figure 7.5 presents the simulated difference scattering signals, where the total signal is separated into contributions from the solute (dS_{solute}), the solvent cage (dS_{cage}), and their combination. The atom-specific solute–solvent correlations reveals distinct behaviors. The Au–MeCN term contributes significantly due to the large atomic number of Au (hence, large scattering factor), while the P–MeCN correlation is weaker overall. The H–MeCN mainly affects very low q range. The C–MeCN contribution dominates over Au–MeCN at low q values because of the large number of carbon atoms in the ligand contacting the solvent shell, despite their lower scattering power.

Their sum gives dS_{cage}, which dominates the total difference signal and even surpasses the solute contribution at low momentum transfer ($q < 1.4$ Å^{-1}). However, this does not affect the structural refinements performed in this work, since the fitting of experimental data was performed only for $q > 1.4$ Å^{-1}, where the solute contribution becomes more prominent and cage contributions are less dominant. The solvation signal contributes into the range we did not utilize for the analysis. Extending the analysis to incorporate this sensitivity will be a critical step in future work, as solvent reorganization has the potential to significantly influence and modulate the photophysical response of bimetallic complexes.

Atomic Contributions to the Difference Scattering

Further simulations were performed for three model systems: a pure Au_2 dimer, an Au_2P_4 core, and the full $[Au_2(dcpm)_2]^{2+}$ complex to disentangle the structural contributions to the scattering signal. The simulated difference scattering curves are shown in Figure 7.6 , where the signals are scaled by momentum transfer ($q\Delta S$) to emphasize oscillatory features. In all three models, the Au-Au distance change is identical with a value of approximately 0.3 Å which is taken from the DFT-optimized GS and ES structures.

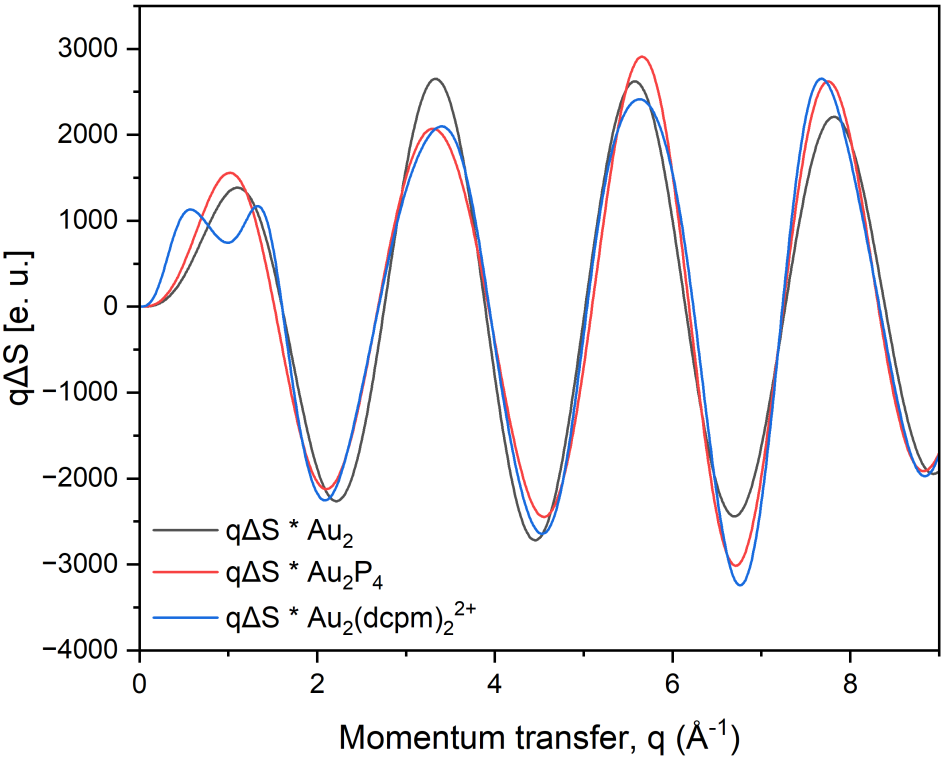

Figure 7.6: Simulated difference scattering signals ($q\Delta S$) for Au_2 (black), Au_2P_4 (red), and $[Au_2(dcpm)_2]^{2+}$ (blue).

The overall shape and oscillation pattern of the difference signal are nearly identical across all three models, despite the increasing structural complexity from Au_2 to $[Au_2(dcpm)_2]^{2+}$. The presence of phosphorous atoms and the full dcpm ligands mainly introduce small modulations in amplitude but do not alter the essential oscillatory features. This clearly confirms that the dominant contribution to the scattering signal in the measured q-range arises from the Au–Au distance contraction, which strongly modulates the high-Z scattering component of the complex. Hence, these findings justify the focus of the present investigation on the structural dynamics around the

Au–Au distance.

To gain the metal-specific sensitivity in time-resolved X-ray scattering, the simulated difference scattering signals were compared for three structurally analogous dimeric complexes, $[Au_2(dcpm)_2](PF_6)_2$, $[Ag_2(dcpm)_2](PF_6)_2$, and $[Cu_2(dcpm)_2](PF_6)_2$. The plotted signals in figure 7.7 represent $q\Delta S(q)$, calculated under identical structural perturbations (e.g., a similar contraction in the metal–metal bond), allowing a direct comparison of scattering intensity and oscillatory behavior across the three metals.

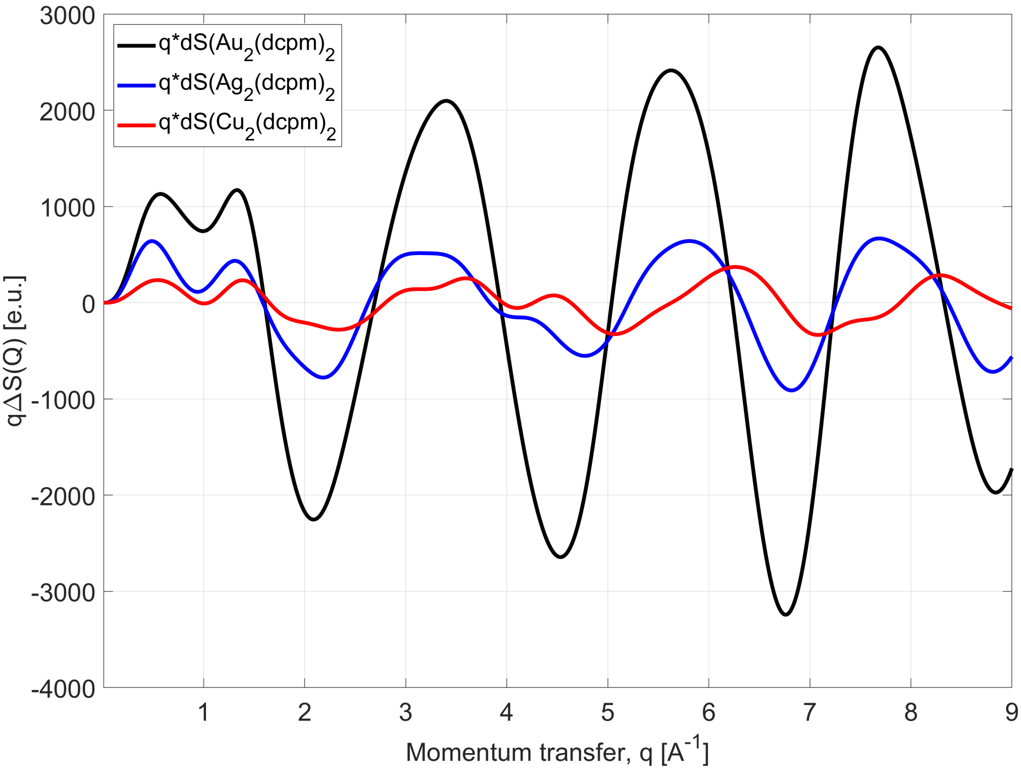

Figure 7.7: Simulated difference scattering signals ($q\Delta S$) for $[Au_2(dcpm)_2](PF_6)_2$ (black), $[Ag_2(dcpm)_2](PF_6)_2$ (blue), and $[Cu_2(dcpm)_2](PF_6)_2$ (red).

The results shows that the magnitude of the difference signal strongly depends on the atomic number of the metal atoms involved. Among the three, $[Au_2(dcpm)_2](PF_6)_2$ (black) shows the strongest signal and sharpest oscillations, followed by $[Ag_2(dcpm)_2](PF_6)_2$ (blue), and then $[Cu_2(dcpm)_2](PF_6)_2$ (red), which displays the weakest signal. This trend originates from the fundamental dependence of elastic X-ray scattering intensity on the atomic form factor, which scales approximately with the square of the atomic number ($\sim Z^2$) in the relevant momentum-transfer regime. Consequently, gold with larger nuclear charge (Z = 79) exhibits substantially higher scattering power compared to silver (Z = 47) and copper (Z = 29). As a result, an identical geometric perturbation produces a markedly weaker absolute scattering response in the lighter dimers, thereby reducing the overall sensitivity of the difference signal to a given structural change.

This simulation-based comparison explains the experimental observation that the time-resolved difference scattering signals acquired at ID09 were significantly weaker for the Ag_2 and Cu_2 analogues relative to the Au_2 system. Despite having identical ligand environments and potentially similar structural dynamics, the intrinsic scattering contrast of the lighter metals limits the observable signal. This underscores the importance of heavy elements in facilitating detectable time-resolved scattering signals, particularly when probing subtle intramolecular bond contractions or low-amplitude structural changes.

7.2 Excited state Aurophilicity in $[Au_2(pnnp)_2]Cl_2$

In Section 6.3.4, the initial analysis of extracted difference scattering signals were presented as a function of individual time delay. For further investigation of the structural dynamics, solute-specific scattering signals were analyzed and extracted by integrating the magnitude of the difference signal, $\sum |q\,\Delta S|$ over the q-range of 2.5–7.5 Å^{-1}. The left side of Figure 7.8 represents these temporal evolution of the solute-specific scattering signal. This specific q-range is highly sensitive to the intramolecular structural changes, particularly those involving the Au–Au bond distances and ligand environment. This magnitude of signal strength representation also reveals a rapid onset immediately after photoexcitation, with a sharp rise occurring around time zero and reaching a maximum intensity near 150 fs. This strong and prompt increase suggest a potential formation of an ultrafast structural response after optical excitation, indicating the initial contraction of the Au–Au distance or related geometry changes within the photoexcited solute.

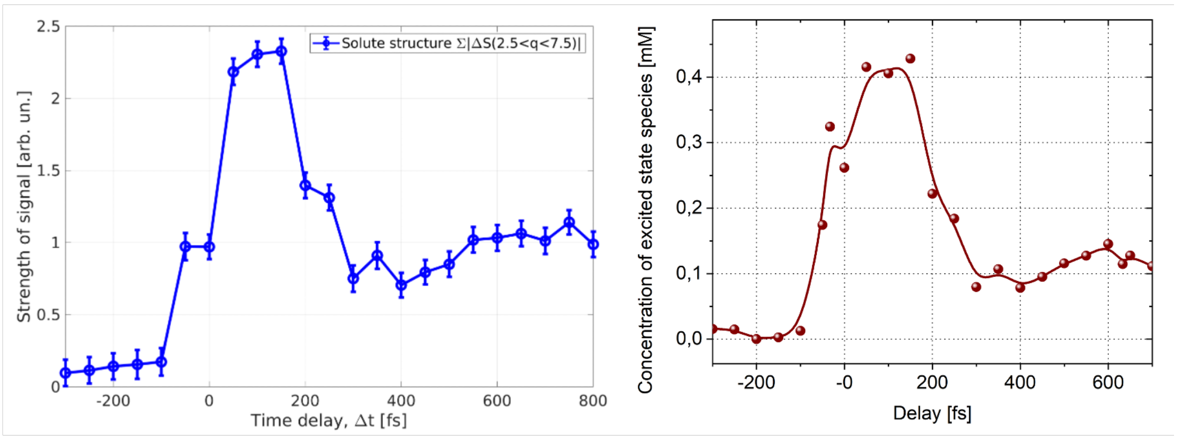

Figure 7.8: Left: Contribution of solute term integrating the q-range between 2.5 to 7.5 Å^{-1} for $[Au_2(pnnp)_2]Cl_2$ in acetonitrile. Right: Concentration of excited state species for $[Au_2(pnnp)_2]Cl_2$ in acetonitrile.

Interestingly, after reaching its peak with maximum signal, the structural signal exhibits a pronounced decay, dropping substantially by $\sim$ 300 fs. This decay most likely reflects the relaxation of the initially excited population back toward the ground-state potential energy surface, rather than a transition to a lower-lying triplet state. The rapid decay of the signal thus corresponds to the dissipation of excess vibrational energy and the recovery of the ground-state geometry following photoexcitation. Beyond this period, the residual weak signal observed between 400 and 800 fs is best interpreted as the slow relaxation of the remaining excited population back to the ground state. This interpretation is also supported by the concentration kinetics, which follow a similar temporal profile to the overall scattering signal, indicating that the observed structural evolution predominantly arises from ground-state recovery dynamics. Further confirmation of these events can be extracted by other analysis methods.

Further analysis of the $[Au_2(pnnp)_2]Cl_2$ provides the dynamics of the concentration of the excited-state species, illustrated in right side of Figure 7.8. The concentration of the excited-state species reaches a maximum shortly after photoexcitation and subsequently decays rapidly. Within the first 300 fs, the excited-state population decreases by approximately 75%, indicating an ultrafast relaxation process. The observed decrease in the difference scattering signal amplitude during this period primarily reflects the depopulation of the excited state. The structural refinement indicates an Au–Au bond contraction of about –0.52 Å associated with the initially populated excited state, the subsequent decay in signal amplitude is best interpreted as a population effect. The temporal correspondence between the population dynamics and structural signatures were considered for proposing the hypothetical relaxation pathway and supports the interpretation discussed in the following section.

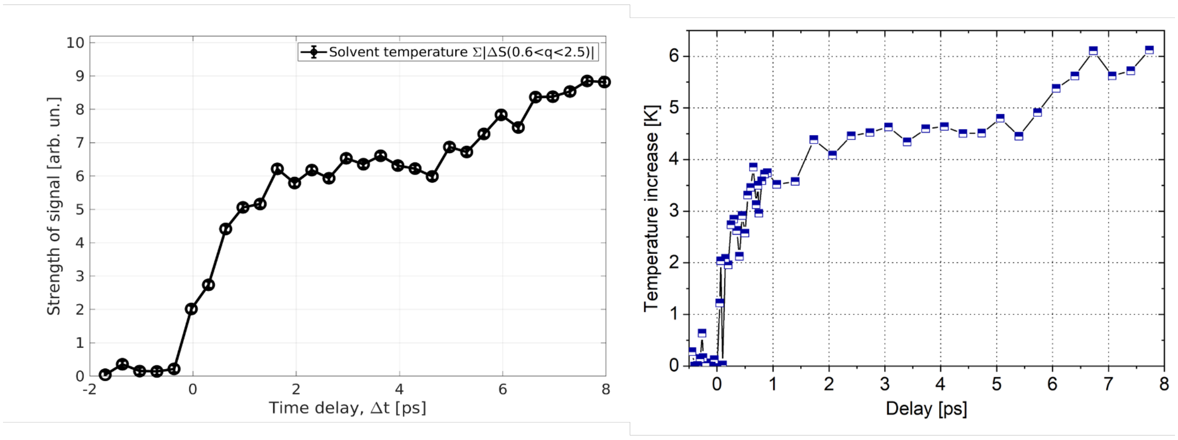

Figure 7.9: Left: Evolution of solvent temperature integrating the q-range between 0.6 to 2.5 Å^{-1} of $[Au_2(pnnp)_2]Cl_2$ in acetonitrile solvent. Right: Absolute temperature rise with increasing time delay during the WAXS experiment of $[Au_2(pnnp)_2]Cl_2$ in acetonitrile.

As mentioned earlier in Section 6.3.4, the signal evolved in the low-q range is predominantly sensitive to long-range correlations and rearrangement in the first solvation shells, while the medium range approximately from 0.5 to 2.5 Å^{-1} is sensitive to the bulk solvent observables such as solvent temperature and density [81]. The left side of Figure 7.9 represents the integrated absolute difference scattering signal over the q-range of 0.6–2.5 Å^{-1}, indicating the solvent heating effects due to vibrational energy dissipation and non-radiative relaxation pathways. The gradual increase in signal strength over several picoseconds reflects the thermalization of the solvent molecules as energy is transferred after the initial excitation and relaxation of the solute to the surrounding solvent shell. Unlike the solute-specific signal, this increase is continuous and monotonic, which is expected for intrinsically slower bulk thermalization process. The clear separation in timescales between the fast solute structural response and the slower solvent thermalization highlights the complementary nature of WAXS in probing both coherent intramolecular dynamics and diffusive solute–solvent energy exchange.

The right side of Figure 7.9 indicates the absolute extracted solvent temperature rise as a function of pump–probe delay time. A sharp increase in temperature is observed immediately after time zero, reaching approximately 4 K within the first 2 ps, which likely reflects immediate deposition of energy to solvent due to excitation and relaxation through a manifold of higher-lying singlet and ligand-centered states by 4.6 eV photons (above the main LMCT resonance) and rapid vibrational energy transfer from the excited $[Au_2(pnnp)_2]Cl_2$ complex to the surrounding acetonitrile solvent. This temperature stabilizes up to ∼5 ps. Beyond 5 ps, the temperature continues to increase more gradually, reaching around 6 K by ∼7 ps, indicating the continued thermalization and solvent reorganization. This trend supports the fast initial solute–solvent coupling followed by slower solvent equilibration.

Structural Refinement from Difference Scattering Data

To quantitatively analyze the time-resolved difference scattering signals of the $[Au_2(pnnp)_2]Cl_2$ complex in acetonitrile, structural refinement was performed using the extracted data, collected under high-energy X-ray conditions (17 keV). As the structural refinement of $[Au_2(dcpm)_2](PF_6)_2$ complex, the difference scattering signal $q\,\Delta S$ was further analyzed at various pump–probe delay times. This approach enabled extraction of the transient excited-state geometries and revealed time-dependent structural evolution in response to photoexcitation.

Figure 7.10 illustrates the structural refinement of the excited-state dynamics of the $[Au_2(pnnp)_2]Cl_2$ complex in acetonitrile solvent at two representative time delays: $\Delta t =$ 100 and 300 fs. At each time delay, experimental difference scattering signals, $q\,\Delta S(q,t)$ (shaded areas around curves represent experimental error-bars) are compared against simulated curves (denoted as total fit in black). Individual contributions from the solute structure (red), solvent heating (green), solvent density (pink), and baseline offsets or zero line (cyan) are explicitly indicated, providing a comprehensive decomposition of the observed structural response. The solvent density contribution at these initial delays is not expected from a purely classical thermodynamics considerations since thermal expansion of the bulk solvent proceeds on much longer ns timescales. However, the ultrafast effects in the nearest solvation shell such as excluded volume may be presented and appear similar to the global change in density [161].

At $\Delta t = 100$ fs delay, the solute term dominates the experimental total differential signal, particularly in the intermediate *q*-range ($\sim$ 3.1–6.5 $Å^{-1}$). This highlights an intramolecular structural response associated predominantly with Au–Au bond contraction and local ligand rearrangements. A closer refinement provides the change of the Au-Au distance of -0.52 Å at 100 fs delay. The solvent-related contribution (green curve), though smaller in magnitude, may arise from a combination of relaxation processes involving ligand-centered (LC) states and possible multiphoton excitation of the solvent, both of which can contribute to the observed transient heating response at these early timescales.

At 300 fs delay, the amplitude of the solute-related oscillations decreases significantly, consistent with vibrational cooling or structural relaxation to the ground state. In contrast, the solvent heat term increases in relative significance, confirming the energy transfer or redistribution from the excited-state solute to the surrounding solvent moleculesince the excess of energy is released as heat upon reaching the GS. Further structural refinement of scattering signals $[Au_2(pnnp)_2]Cl_2$ complex provides the change of the Au-Au distance of -0.54 Å at 300 fs delay. The solvent density term remains relatively small at this delay, but its presence underscores the subtle but important influence of solvent reorganization along with the relaxation of solute molecule.

A further structural refinement at longer time delay of 100 ps (in figure 7.11), indicates the change of the Au-Au distance of -0.58 Å. The experimental data (blue circles) exhibit well-defined maxima and minima characteristic of intramolecular rearrangements within the Au_2 core. Fitting the data with a model (red line) demonstrates excellent agreement when the solute difference term (black curve) is combined with the solvent heating (cyan) and density (magenta) responses. These structural refinements and their respective contributions at individual delay times indicate ultrafast and coherent solute dynamics, rapidly transitioning into solvent-mediated thermal relaxation processes within a few hundred femtoseconds.

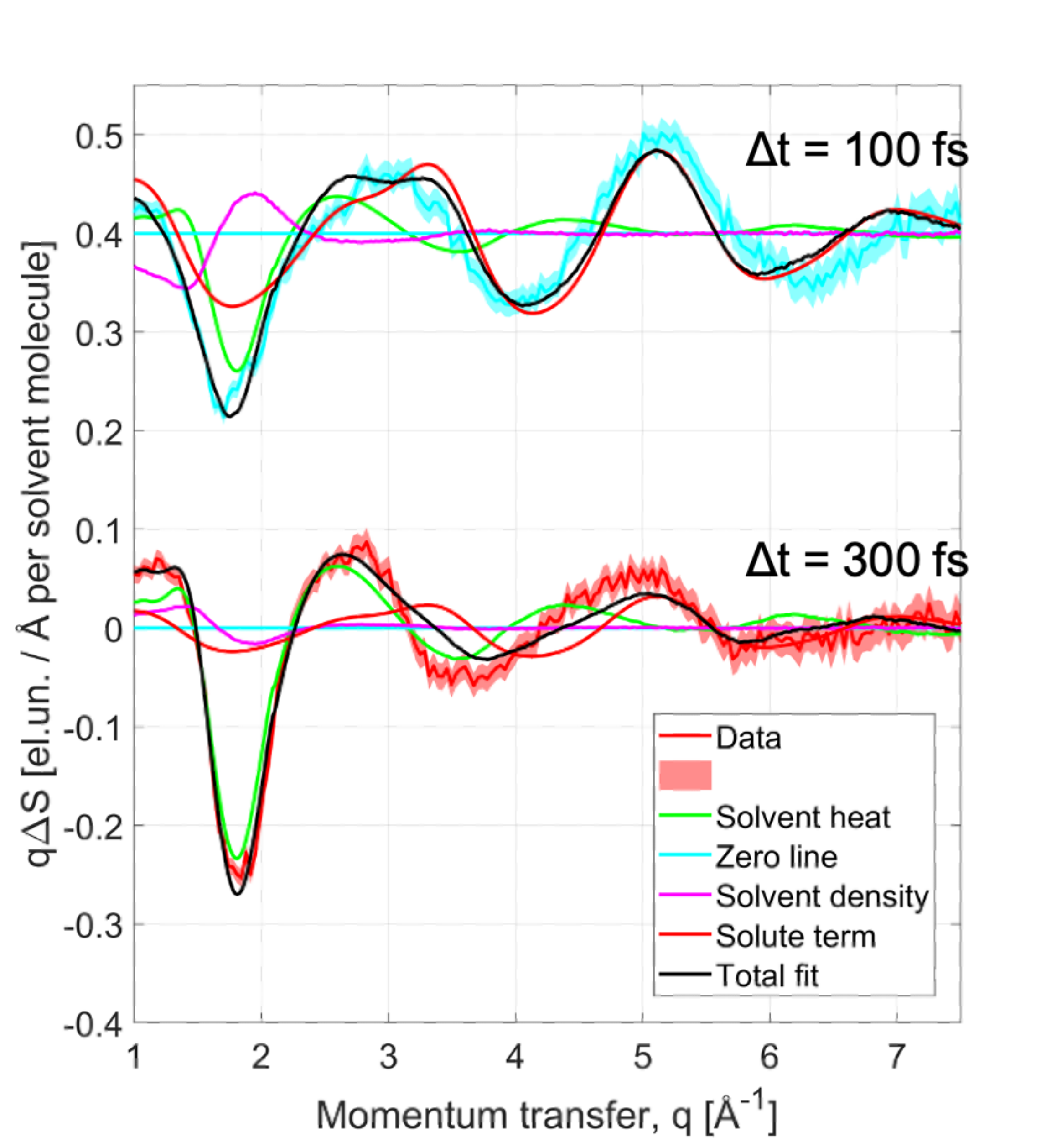

Figure 7.10: Integrated difference scattering signals $q\,\Delta S$ as a function of momentum transfer q at different pump-probe delay time, collected at FXE beamline for $[Au_2(pnnp)_2]Cl_2$ in acetonitrile solvent. More details are described in the main text.

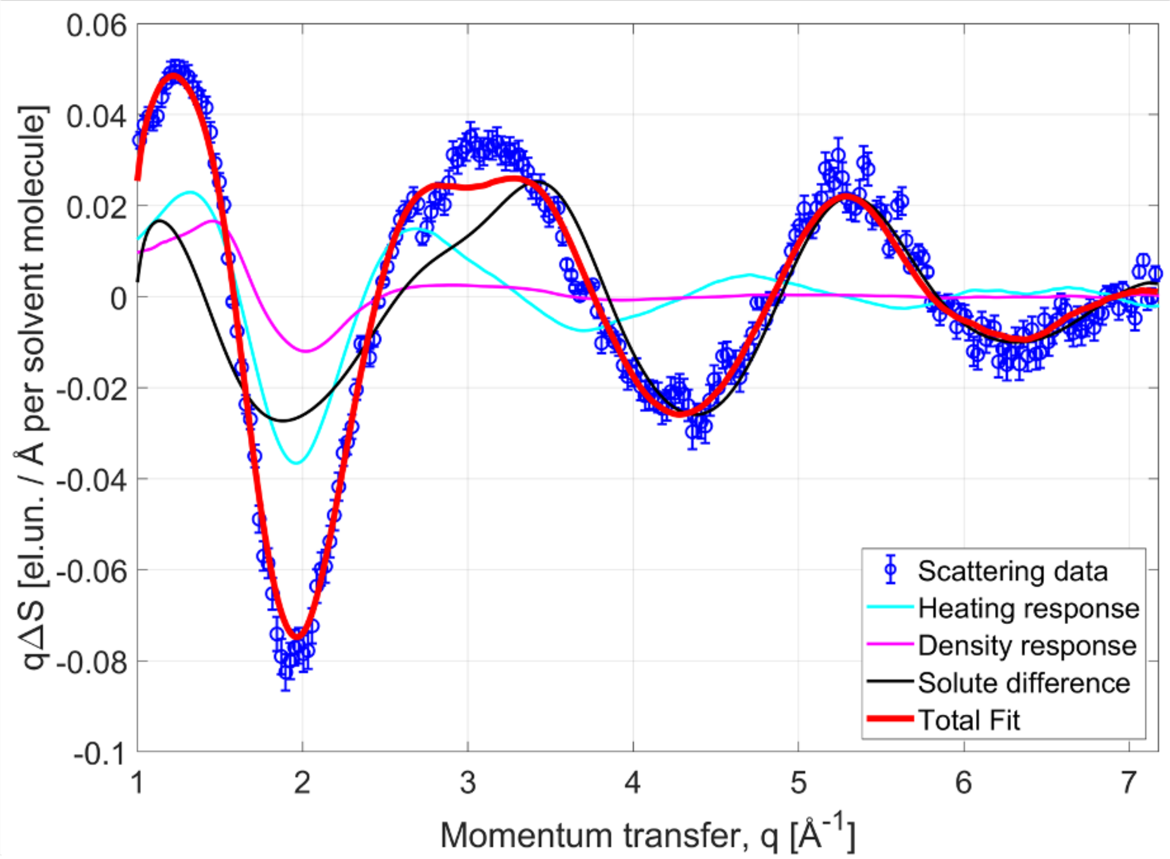

Figure 7.11: Time-resolved X-ray scattering signal and structural refinement of the $[Au_2(pnnp)_2]Cl_2$ complex in acetonitrile solvent at 100 ps, measured at ID09 (ESRF).

Potential Energy Surface and Excited State Dynamics

Considering all the contributions from different terms, the simplified potential energy diagram in Figure 7.12 can be proposed for $[Au_2(pnnp)_2]Cl_2$ complex in acetonitrile. After the initial optical excitation with 266 nm (represented by the blue vertical arrow), the system is promoted from the ground state to a manifold of overlapping excited states in the Franck–Condon region, comprising both ligand-initiated charge-transfer state (^{1}ILCT) and higher-lying singlet ligand-to-metal–metal charge-transfer (^{1}LMMCT, as S2,S3,S4....) states, consistent with the broad overlap observed in the UV–Vis absorption spectrum. The subsequent formation of the lowest-lying singlet LMMCT state occurs within the instrument (experimental time) resolution (ca. 60 fs FWHM), and this state is characterized by a significantly contracted Au–Au equilibrium bond distance. The early-time (ca. 100 fs) differential scattering response reflects the onset of ultrafast structural reorganization on the LMMCT potential energy surface. The total excited-state population decreases by approximately 75% within 300 fs, indicating an ultrafast relaxation pathway toward the ground state.

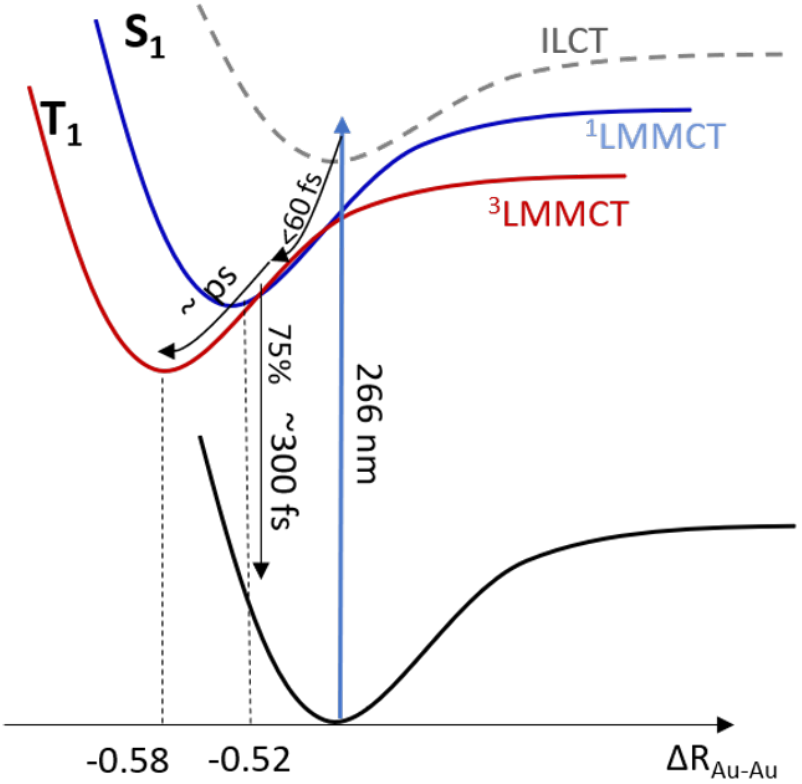

Figure 7.12: Potential energy surface diagram for $[Au_2(pnnp)_2]Cl_2$ in acetonitrile solvent. After photoexcitation, the ground state electron goes to the excited singlet state and then it moves to the excited triplet state and finally relaxes to the ground state.

The decrease of structural high-q oscillation amplitude at longer delays (300 fs) in the difference scattering signals reflects a reduction in the overall excited-state population. At this stage, the system remains on the singlet LMMCT potential energy surface, where rapid relaxation processes lead to partial depopulation of the initially excited species. The formation of the lower-energy triplet LMMCT state (^{3}LMMCT) is expected to occur on a much longer timescale, on the order of 100 ps, as supported by the ESRF data and consistent with the phosphorescent emission lifetimes. This triplet state represents the long-lived luminescent intermediate characterized by a slightly elongated Au–Au distance compared to the singlet state. Additionally, the observed ~8 ps rise in solvent temperature may indicate the timescale of energy dissipation associated with the $S_1 \rightarrow T_1$ relaxation process.

Similar to the $[Au_2(dcpm)_2](PF_6)_2$ complex, the cage term contribution can be determined by using the MD simulations. Here as well, we expect that the solvation will mostly contribute the difference signals in the q-range below 1 $Å^{-1}$ not used for structural refinement similar to how it is shown in case of $[Au_2(dcpm)_2](PF_6)_2$ complex and further calculations are planned as the future extension of these work.

Chapter 8

Conclusions

This doctoral thesis is focused on investigation of the structural dynamics, and photophysical behavior of metallophilic interactions, with a significant attention to aurophilic interactions in dinuclear gold(I) complexes. These attractive interactions between closed-shell d^{10} metal centers have emerged as a key design element for functional materials, influencing luminescence, bio-imaging, reactivity, and supramolecular assembly. By combining advanced synthetic chemistry, steady-state characterization with X-ray spectroscopy, and state-of-the-art time-resolved X-ray scattering, this study has delivered insights into the structural evolution of gold(I) dimers upon photoexcitation and the effect of ligand architecture on the structural dynamics. This study bridges the gap between static structural knowledge and ultrafast excited-state phenomena, contributing significantly to the understanding of aurophilicity in solution.

A series of structurally diverse bimetallic complexes were synthesized to systematically investigate metallophilic interactions under well-defined chemical environments. High-yield synthetic protocols were developed and optimized for $[Au_2(pnnp)_2]Cl_2$, $[Au_2(pnnp)Cl_2]$ and $[Cu_2(dcpm)_2](PF_6)_2$ complexes, employing inert atmosphere and low-temperature conditions to ensure chemical stability in solution in the presence of phosphine-based ligands. In contrast, the synthesis of $[Au_2(dcpm)_2](PF_6)_2$, and $[Ag_2(dcpm)_2](PF_6)_2$ was successfully carried out under ambient conditions, with accurate reaction stoichiometry control and purification methods. All complexes were thoroughly characterized using NMR spectroscopy and UV–Vis absorption spectroscopy.

Time-resolved WAXS experiment on the $[Au_2(dcpm)_2](PF_6)_2$ complex revealed rapid and significant structural dynamics in the excited state, characterized by a pronounced shortening of the Au–Au distance within 100 fs after excitation. The structural refinement of the solution phase scattering data indicated a contraction from a ground-state Au–Au distance of ~ 2.893 Å to ~ 2.780 Å upon excitation with 266 nm optical laser within 100 fs delay, implying ~ 0.113 Å contraction between the two Au-Au centers in the $[Au_2(dcpm)_2](PF_6)_2$ complex which is comparatively larger than the literature value extracted from the crystallographic measurements.

For $[Au_2(pnnp)_2]Cl_2$ complex, the time-resolved WAXS experiment revealed more dramatic structural change due to aurophilic interaction. Having larger and flexible phosphine ligands attached to the Au centers suggest more degree of structural flexibility in solution phase and also in the excited state. Consequently, this allows more significant metallophilic contraction, but with faster relaxation kinetics, indicating weaker stabilization of the T_1 triplet excited-state structure, thus greatly reducing the efficiency of photoluminescence. The structural refinement of the scattering data of $[Au_2(pnnp)_2]Cl_2$ complex in acetonitrile indicated a contraction of ~ 0.52 Å at 100 fs delay in the S_1 singlet state, whereas the distance change can reach up to ~ 0.58 Å at 100 ps delay likely in the triplet state.

The reliable structural refinement of the excited state was only possible from WAXS due to the extended q-range available in the data, although the fitting was performed starting from a medium q-range. This allowed to exclude the change in solvation shell structure from the model since being in the longer length scales it contributed to smaller q as confirmed by preliminary classical MD simulations.

In conclusion, the results presented here explain the extend and evolution of ultrafast Au-Au bond formation in the excited state, as well as the associated relaxation pathways, which are found to be highly dependent on the ligand architecture and the initial Au–Au separation in the ground state.

These observations confirm that ligand design offers an effective strategy to modulate the magnitude and timescale of metallophilic interaction dynamics, thereby offering a tunable framework for the development of photoresponsive or optoelectronic materials. Moreover, the integration of structural refinement with spectroscopic kinetics establishes a generalizable methodological platform for probing excited-state structural evolution in a wide range of transition-metal complexes exhibiting photoinduced reorganization phenomena.

8.1 Future plan

The findings presented here open several avenues for future research. An extended investigation of aurophilic interaction should explore with fs EXAFS in solution unifying the structural refinement approach for GS an ES with the same gold complexes. The extended fs HERFD-XAS study on gold L_3 edge will also provide the insight into the actual local electronic states (singlet vs triplet) and charge transfer processes of these gold dimer complexes.

On the other hand, another approach of the study can follow with higher oxidation states of gold atoms, like Au(I)–Au(III) and Au(III)–Au(III). The recent theoretical investigations indicate that the strength of such aurophilic interactions is comparatively weaker than to the classical Au(I)$\cdots$Au(I) interactions discussed thoroughly in this thesis. These are nevertheless non-negligible and may still play a structurally and electronically significant role [162, 163]. A large variety of these type of interactions and their extend are explained in [2] and need further attention of the experimental scientist.

Another part of these research could follow the extended heterometallic systems, exploring different d^{10} metals such as Au–Cu, Ag-Cu or Au–Ag pairs. Expanding the effect of different solvents and solvent dynamics could reveal new regimes of metallophilicity. Such advancements hold promise for developing responsive luminescent devices, photocatalysts, and plasmonic systems exploiting metallophilic interactions as a functional design principle.

Appendix A

FEFF input file

Listing A.1: The following feff.inp file was used for the analysis of the EXAFS experimental data for the $Au_2(dcpm)_2(PF_6)_2$ complex.

```
 * This feff6 file was generated by Demeter 0.9.26
 * Demeter written by and copyright (c) Bruce Ravel, 2006-2018

 * --*--*--*--*--*--*--*--*--*--*--*--*--*--*--*--*--*--*--*--*--*--*--*--*--
 *  total mu*x=1:  2.996 microns,  unit edge step:  5.116 microns
 *  specific gravity:  18.047
 * --*--*--*--*--*--*--*--*--*--*--*--*--*--*--*--*--*--*--*--*--*--*--*--*--
 *  normalization correction:    0.00042 ang^2
 * --*--*--*--*--*--*--*--*--*--*--*--*--*--*--*--*--*--*--*--*--*--*--*--*--

 TITLE  Au2DCPM2

 HOLE      4   1.0   * FYI: (Au L3 edge @ 11919 eV, 2nd number is S0^2)
 *         mphase,mpath,mfeff,mchi
 CONTROL   1      1     1     1
 PRINT     1      0     0     0

 RMAX      6.0
  * POLARIZATION  0.0   0.0   0.0

 POTENTIALS
  * ipot   Z      tag
     0     79     Au
     1     79     Au
     2      6      C
     3     15      P
     4      1      H


 ATOMS                  * this list contains 148 atoms
  *   x          y          z     ipot tag          distance
0.315383621     3.230982375     0.077246292     2       C
-0.237431587    2.321816223     -1.418575446    3       P
0.038339066     0.009282429     -1.327282543    0       Au
0.238796132     -2.309887018    -1.404283786    3       P
-0.043555246    -3.175956059    0.190707248     2       C
-0.691257346    -2.2134648      1.610873583     3       P
-0.161572352    0.053065125     1.547442245     1       Au
```

```
0.597061815     2.257835136     1.609438372     3       P
-0.422759227    4.008285749     0.289042125     4       H
1.250912432     3.742365453     -0.162882959    4       H
-0.706708934    -4.026514923    0.01414972      4       H
0.917617785     -3.586619466    0.505758336     4       H
-4.670842671    -1.911202534    0.50637177      2       C
-3.160230668    -1.740029616    0.497959849     2       C
-2.496514421    -2.503815921    1.642249453     2       C
-3.088881948    -2.073310145    2.983684384     2       C
-4.604164989    -2.229145667    2.989251038     2       C
-5.255627979    -1.474933642    1.840277218     2       C
-4.919840059    -2.962839914    0.321752697     4       H
-2.920298902    -0.678248954    0.616339329     4       H
-2.650802257    -3.580569978    1.501776967     4       H
-2.827861329    -1.022654848    3.164936903     4       H
-4.852693142    -3.294292063    2.909339189     4       H
-5.085367793    -0.398912541    1.970445044     4       H
-5.104799423    -1.331488939    -0.313475504    4       H
-2.751735347    -2.046230357    -0.467554417    4       H
-2.657543283    -2.655929049    3.800624989     4       H
-4.999927965    -1.883720014    3.948393308     4       H
-6.338206915    -1.628972123    1.851457761     4       H
2.099967734     -3.312382623    4.475107667     2       C
1.532323074     -2.732124384    3.187269922     2       C
0.033855156     -3.016638795    3.085022479     2       C
-0.259353054    -4.511092448    3.183129447     2       C
0.321658621     -5.085067817    4.469567173     2       C
1.812328763     -4.802620362    4.584356477     2       C
1.652864215     -2.790821224    5.329849914     4       H
2.056247154     -3.182627494    2.336788194     4       H
-0.457057963    -2.502810397    3.921451148     4       H
0.186433603     -5.026030904    2.324643467     4       H
-0.199574312    -4.63962797     5.32546905      4       H
2.341554424     -5.330361431    3.781357861     4       H
3.176754972     -3.125669483    4.516833462     4       H
1.715012434     -1.65436626     3.137909061     4       H
-1.336026501    -4.694744644    3.14244395      4       H
0.132129537     -6.16141756     4.508337        4       H
2.199454756     -5.194524029    5.529125132     4       H
4.529551246     1.167077375     0.906541745     2       C
-2.389563699    -2.901772496    -4.587335771    2       C
1.108254788     5.169889272     -4.157032096    2       C
3.022191783     1.287440988     0.751063606     2       C
-1.277163158    -2.255820669    -3.772856716    2       C
0.403210526     4.606164508     -2.929445685    2       C
2.416301534     2.204427181     1.812689301     2       C
-0.965569132    -3.101140311    -2.539602567    2       C
0.635539237     3.101391362     -2.82192782     2       C
2.79191503      1.728420547     3.215146125     2       C
-0.607790972    -4.53960619     -2.906907544    2       C
2.125012984     2.762974291     -2.807478629    2       C
4.301328401     1.587145869     3.363648543     2       C
-1.728403707    -5.167037483    -3.727044203    2       C
2.816315125     3.333740627     -4.038020759    2       C
4.891013254     0.675216651     2.298840521     2       C
-2.045606693    -4.336202724    -4.961681354    2       C
2.592051775     4.834570547     -4.152283809    2       C
4.992401462     2.145212794     0.729495743     4       H
-3.313700603    -2.892064935    -3.99638832     4       H
```

```
0.643683085     4.751938173     -5.058190511    4       H
2.570855833     0.293745876     0.855413982     4       H
-0.383071173    -2.154010553    -4.394958223    4       H
0.793583977     5.098891206     -2.031770418    4       H
2.784810951     3.22640735      1.662050696     4       H
-1.879553183    -3.132696757    -1.931654232    4       H
0.193426481     2.609253043     -3.697611418    4       H
2.316195676     0.756782311     3.400347379     4       H
0.31702868      -4.552190456    -3.492656813    4       H
2.591519355     3.187379792     -1.910810818    4       H
4.763390753     2.578787631     3.286988881     4       H
-2.626248419    -5.245958427    -3.102318848    4       H
2.420963651     2.8373813       -4.932320061    4       H
4.496342576     -0.339885606    2.433890984     4       H
-1.175243933    -4.33586053     -5.629489558    4       H
3.071685032     5.335719685     -3.302449311    4       H
4.919658809     0.487422108     0.143559182     4       H
-2.580502136    -2.306637888    -5.484688503    4       H
0.960654861     6.252701766     -4.197793776    4       H
2.773198963     1.638771258     -0.252612073    4       H
-1.565670921    -1.246039396    -3.465763531    4       H
-0.66574771     4.8285369       -2.976740999    4       H
2.411697609     2.41876689      3.971425525     4       H
-0.422346199    -5.133004852    -2.006920613    4       H
2.260690896     1.678061785     -2.757217126    4       H
4.531308336     1.208238938     4.363418081     4       H
-1.448240059    -6.185106619    -4.011536059    4       H
3.88538729      3.107714514     -3.995109234    4       H
5.976756703     0.612276535     2.412872374     4       H
-2.87059916     -4.789141093    -5.518817042    4       H
3.069725689     5.220095554     -5.057384434    4       H
-2.132732591    4.08750555      4.146503123     2       C
3.716098112     -2.67294941     -3.657021743    2       C
-4.028402087    2.447324874     -3.096527896    2       C
-1.596426096    3.336681089     2.935382104     2       C
2.271359071     -2.347573506    -3.30085086     2       C
-2.524071716    2.24876796      -2.968140024    2       C
-0.071432075    3.268215095     2.977682082     2       C
1.947720464     -2.776047745    -1.870309038    2       C
-2.018282451    2.70381778      -1.599104196    2       C
0.547470319     4.660848157     3.070907779     2       C
2.932979038     -2.135646053    -0.891070313    2       C
-2.797110539    2.016235846     -0.479555295    2       C
-0.002965049    5.40928398      4.278978158     2       C
4.371363981     -2.477028722    -1.249229814    2       C
-4.297136967    2.218618495     -0.619336747    2       C
-1.522489839    5.477377253     4.249740528     2       C
4.69336987      -2.050281243    -2.672455321    2       C
-4.785197934    1.746021599     -1.979320432    2       C
-1.898779912    3.517038559     5.053308082     4       H
3.846099901     -3.761805556    -3.656956131    4       H
-4.251555195    3.520582975     -3.06600053     4       H
-1.916269031    3.860433698     2.027229724     4       H
2.104412966     -1.266795001    -3.393758622    4       H
-2.285594422    1.184694687     -3.095722408    4       H
0.210039365     2.69507146      3.870395971     4       H
2.01239689      -3.868411116    -1.790945057    4       H
-2.126954087    3.79118576      -1.507452755    4       H
0.315810914     5.224800243     2.160101629     4       H
```

```
2.802140778     -1.048405395    -0.93384836     4       H
-2.576156344    0.944192026     -0.523502393    4       H
0.319923741     4.895651706     5.192456009     4       H
4.524250814     -3.557839182    -1.146242122    4       H
-4.535526197    3.281426142     -0.493293817    4       H
-1.839762922    6.073907657     3.385514553     4       H
4.62881505      -0.957084462    -2.741649037    4       H
-4.628877017    0.662920617     -2.060309845    4       H
-3.2226247      4.151328798     4.08371467      4       H
3.923532635     -2.329101886    -4.674148322    4       H
-4.358801848    2.082537554     -4.073056909    4       H
-2.017016634    2.327331254     2.891584126     4       H
1.600704724     -2.834864382    -4.010310341    4       H
-2.010290097    2.788682336     -3.766700005    4       H
1.636235826     4.595264948     3.136986886     4       H
2.723915006     -2.437300886    0.13790682      4       H
-2.461117888    2.365151736     0.498309189     4       H
0.425315216     6.414938082     4.311919904     4       H
5.046093583     -1.990720521    -0.539007467    4       H
-4.8096275      1.679573524     0.182996292     4       H
-1.895342678    5.988954317     5.141511275     4       H
5.719759342     -2.325188457    -2.930914907    4       H
-5.859955066    1.920344126     -2.081086063    4       H

END
```

Appendix B

ORCA input file

Listing B.1: XYZ coordinates of the optimized $Au_2(dcpm)_2(PF_6)_2$ ground-state structure at 2.882 Å

```
Coordinates from ORCA-job Au2DCPM2_GS_PBE0mecn E -3595.732222037687
  C           0.31691331999191      3.22681557819052      0.07886530101059
  P          -0.23370843536491      2.32676621694615     -1.42347521062326
  Au          0.04714851767057      0.01440967460535     -1.36371272317417
  P           0.24230271946851     -2.30485818803035     -1.41038729747041
  C          -0.04069537848836     -3.15858505550014      0.19184977731462
  P          -0.69866152376837     -2.20706864296449      1.61556051837748
  Au         -0.17748175110745      0.06144870129481      1.58441595226744
  P           0.59218423391459      2.26192848722434      1.61792261774443
  H          -0.41923510766313      4.00732101317971      0.28616726358791
  H           1.25518515763535      3.73504977381304     -0.15740020249067
  H          -0.69710297177882     -4.01476661354013      0.01647480690525
  H           0.92240087545182     -3.56270758400450      0.50937999846560
  C          -4.67457140221820     -1.93109126312717      0.49091709593338
  C          -3.16542922905680     -1.74702058750491      0.49083279251968
  C          -2.50184531457096     -2.50963001288153      1.63590695578225
  C          -3.10414443527263     -2.08847939098850      2.97577796497363
  C          -4.61811710385028     -2.25649991462456      2.97338030584363
  C          -5.26989887899912     -1.50425275411789      1.82325145549341
  H          -4.91353657143587     -2.98419315337051      0.30147115984189
  H          -2.93520512696858     -0.68367032103038      0.61362249695731
  H          -2.64746888187185     -3.58696611753594      1.49051676018048
  H          -2.85238455201673     -1.03633220237358      3.16141757375341
  H          -4.85776289267761     -3.32336913653161      2.88940977057640
  H          -5.10942680708814     -0.42722392221224      1.95761752556121
  H          -5.10930693555139     -1.35224679438536     -0.32910633329732
  H          -2.74941122081994     -2.04683478664746     -0.47346509138961
  H          -2.67198418547509     -2.67018521882987      3.79296430127634
  H          -5.02150971960930     -1.91692202115304      3.93143823132556
  H          -6.35117771892133     -1.66744553895015      1.82828397512000
  C           2.09064020600686     -3.32075649679922      4.47630974409291
  C           1.52256908633136     -2.73187529707736      3.19259369718775
  C           0.02523924911174     -3.02103630374902      3.08492699127241
  C          -0.26301581430024     -4.51710101064609      3.17157359141367
  C           0.31786901880062     -5.09858358105620      4.45470815268438
  C           1.80753987240280     -4.81266309532071      4.57350051431496
  H           1.64123857158957     -2.80733794170175      5.33475931459739
  H           2.04977265116295     -3.17300099438587      2.33923422695318
```

```
H        -0.46941518657347     -2.51544558564926      3.92418898817517
H         0.18565041744498     -5.02478101584550      2.31028883858519
H        -0.20563463235563     -4.66072137744780      5.31312352128918
H         2.33933519275212     -5.33251100103949      3.76704827519468
H         3.16680668125613     -3.13101626123953      4.52051481134274
H         1.70125266148872     -1.65305958988246      3.15301976858433
H        -1.33901182352814     -4.70401665627365      3.12799569298040
H         0.13138308398152     -6.17571924449352      4.48550126549740
H         2.19474185150229     -5.21077315190837      5.51563839441808
C         4.51313201754281      1.14066599310969      0.90302546136310
C        -2.38643717378578     -2.92547777556269     -4.58787199301410
C         1.09797991889477      5.21211221800494     -4.13023652682428
C         3.00534523479438      1.26601737816928      0.75642497835724
C        -1.27419130367914     -2.27203786753990     -3.77911127956790
C         0.39518808840202      4.63136048818182     -2.90935295372329
C         2.41167048491432      2.19622498355825      1.81344340119530
C        -0.96231903228253     -3.10633243971756     -2.53848600580870
C         0.63343596887512      3.12643260494327     -2.81909424090925
C         2.79191316777206      1.72875354137118      3.21743024175929
C        -0.60446291815769     -4.54786133550421     -2.89325881447591
C         2.12400898099664      2.79197450794632     -2.81028296214360
C         4.30149132307077      1.58118902992241      3.35853687234008
C        -1.72502503781746     -5.18286544189151     -3.70752618170524
C         2.81337708171748      3.38180689542540     -4.03291161056853
C         4.88098323670122      0.65863781969649      2.29719375333514
C        -2.04235055593741     -4.36313042313243     -4.94947921262877
C         2.58315075068460      4.88304438436075     -4.12836982418050
H         4.97893429157246      2.11528805148884      0.71478876614878
H        -3.31054796684881     -2.91071630907897     -3.99698088701621
H         0.63578932715269      4.80237377879704     -5.03637084315716
H         2.55036580847965      0.27545405592354      0.87426421154988
H        -0.38011001694521     -2.17514394050462     -4.40205122534936
H         0.78340671293627      5.11604461476208     -2.00641229876716
H         2.78726635175548      3.21404357765286      1.65262069407230
H        -1.87622244688297     -3.13245656787416     -1.93024110236477
H         0.19166858220592      2.64316748390653     -3.69990044765115
H         2.31226968076996      0.76094224415427      3.41224051170640
H         0.32013883929880     -4.56522896095500     -3.47926830402821
H         2.59010204774829      3.20349722761996     -1.90734801281166
H         4.76772877916670      2.57005337832761      3.27199185751525
H        -2.62280512698917     -5.25654190648698     -3.08205339712062
H         2.42026175851354      2.89548895044462     -4.93369552551146
H         4.48290514297069     -0.35370823500857      2.44243389343922
H        -1.17197324456534     -4.36859323153302     -5.61724119128642
H         3.05995921391153      5.37558052302213     -3.27193009570249
H         4.89546062887628      0.45288361482764      0.14345864438312
H        -2.57760353099119     -2.33835562026473     -5.49043706050420
H         0.94568978939798      6.29466408923658     -4.15870241606083
H         2.75030990004808      1.60790074191831     -0.24914279501618
H        -1.56327244086284     -1.25967036542329     -3.48100450812646
H        -0.67479554604213      4.84926535142267     -2.95425953348807
H         2.41908886635488      2.42655623006629      3.97058763043039
H        -0.41827217637637     -5.13342884397505     -1.98828952793010
H         2.26212785751770      1.70671279537962     -2.77590908069018
H         4.53542896404347      1.20846778118492      4.35970530496151
H        -1.44460985554953     -6.20335031815199     -3.98298648641767
H         3.88332761308103      3.15951165097934     -3.99263202897910
H         5.96712173973057      0.59206128688753      2.40523154932285
H        -2.86730159519348     -4.82101914943755     -5.50261902478930
```

```
  H          3.05998775971565      5.28174408376593     -5.02818679339735
  C         -2.11700937439760      4.13969572792382      4.14039067506950
  C          3.71981480268143     -2.69517421396802     -3.65736999671883
  C         -4.03186285941135      2.43742872384227     -3.08401508449300
  C         -1.58832489874965      3.37248097561924      2.93623681639595
  C          2.27636438270338     -2.36184247170094     -3.30342496767523
  C         -2.52582382242025      2.24808849075766     -2.96253297451394
  C         -0.06374748094460      3.29226746777445      2.97721852605051
  C          1.95042674158148     -2.78023396737626     -1.87033072633474
  C         -2.01655286872366      2.70303024105919     -1.59480499441404
  C          0.56653430322039      4.68051641792802      3.05608765100824
  C          2.93776669653194     -2.13708459905459     -0.89488986222368
  C         -2.78679740023131      2.01013846749395     -0.47252689166514
  C          0.02384033383313      5.44496723620423      4.25763145249358
  C          4.37457369568245     -2.48792890478304     -1.25052156006375
  C         -4.28874548852827      2.20207612714758     -0.60627413383264
  C         -1.49512867728036      5.52536415562746      4.22956220832187
  C          4.69919478156397     -2.07081798103324     -2.67598309530907
  C         -4.77899708606109      1.72851903538054     -1.96512301321807
  H         -1.88677395456300      3.57607818565702      5.05241756025372
  H          3.84537149670310     -3.78452679444296     -3.65093354649710
  H         -4.26189990523570      3.50912665659000     -3.04992976217778
  H         -1.90530471258791      3.88902404113687      2.02291680627397
  H          2.11404035538184     -1.28088766923277     -3.40245686974838
  H         -2.28135029986215      1.18571081586202     -3.09348440109435
  H          0.21433952095730      2.72562431786855      3.87515502889282
  H          2.01165044485815     -3.87222819855210     -1.78383681345068
  H         -2.12953163257294      3.78971543214511     -1.50069953538488
  H          0.33835365462642      5.23782578930011      2.14033445948275
  H          2.81188910590797     -1.04951106928217     -0.94496440578454
  H         -2.55813447799911      0.93973049383802     -0.51714750166067
  H          0.34362702732491      4.93753881789811      5.17565735626172
  H          4.52158630833373     -3.56896822034894     -1.14156030463628
  H         -4.53413204618957      3.26294570543680     -0.47739802861504
  H         -1.80852599100566      6.11628194244847      3.36008533495594
  H          4.63915148574063     -0.97779871871699     -2.75143076834779
  H         -4.61506092127559      0.64677483006050     -2.04887029458020
  H         -3.20641346766471      4.21192191750675      4.07819187615448
  H          3.92889831035617     -2.35803637485261     -4.67640050218297
  H         -4.36421025096805      2.07277135894956     -4.05992933339983
  H         -2.01688530164086      2.36605534436456      2.90337685251964
  H          1.60373700732179     -2.85034420611778     -4.01021642600611
  H         -2.01843777074565      2.79299338477755     -3.76186962188128
  H          1.65484401264613      4.60670558002985      3.12128409364765
  H          2.72727616550282     -2.43058557967071      0.13618345739850
  H         -2.44986549481750      2.36159326254092      0.50421564121320
  H          0.46046513034907      6.44731149419107      4.28046320115946
  H          5.05173270932088     -2.00150583058905     -0.54273982321079
  H         -4.79421154016439      1.65804122676677      0.19716859263671
  H         -1.86265129131572      6.04844458616303      5.11685580814342
  H          5.72456230064222     -2.35150755746424     -2.93225746172902
  H         -5.85540756575346      1.89519996204660     -2.06206730859763
```

Listing B.2: XYZ coordinates of the ground-state structure of $Ag_2(dcpm)_2(PF_6)_2$

```
Coordinates from ORCA-job Ag2DCPM2_GS_PBE0mecn E -3618.189579350740
  C          0.28610033272045      3.32697011498417      0.08985556253575
  P         -0.28816325634719      2.37832349981962     -1.37637734478460
  Ag         0.08601724548853      0.00804960101069     -1.34619473590512
```

```
P           0.30239962959759     -2.38159656979084     -1.37580780755990
C          -0.09906633356463     -3.24926691610803      0.19801964260096
P          -0.78751717474677     -2.24200582488087      1.57233404441123
Ag         -0.22557470635738      0.08913822746615      1.56823383543937
P           0.62496699559460      2.33425072182758      1.59894723237313
H          -0.46790322905715      4.08134840148079      0.32622803943536
H           1.19929442426324      3.86484049492027     -0.17670673914956
H          -0.78466082438684     -4.07327004602549     -0.01554341540102
H           0.82417284809114     -3.69662038828231      0.57132724052074
C          -4.70674305195361     -2.13517407449831      0.21030903792725
C          -3.19410734160781     -1.97633136794338      0.23938730459985
C          -2.59692384435633     -2.52306779919317      1.53299290489314
C          -3.25462252330811     -1.87348505615940      2.75028056172979
C          -4.76977083063227     -2.02320087866990      2.70970104133681
C          -5.35310488946668     -1.47424817223073      1.41709383243759
H          -4.95600599955056     -3.20299154085015      0.20268231695830
H          -2.93900002299890     -0.91469326296370      0.15294814426882
H          -2.75740643979826     -3.60752977146664      1.56818932120914
H          -2.99504277258585     -0.80626267340397      2.76456981819362
H          -5.02644357731977     -3.08550255065365      2.80009469643568
H          -5.17791787729667     -0.39243617949876      1.37163332566999
H          -5.09892589666332     -1.71067872094326     -0.71815845386410
H          -2.75791435712311     -2.47573228727525     -0.62670288736858
H          -2.86515087385908     -2.30820615864641      3.67382010888803
H          -5.20733744234098     -1.51673847378221      3.57453510126724
H          -6.43660755903023     -1.62109716583081      1.39686232167647
C           1.81393885237892     -3.34125525049416      4.61464986960666
C           1.32296674781499     -2.77101604980047      3.29140328486561
C          -0.16761805639347     -3.04910538370255      3.09879295744984
C          -0.47564585221131     -4.53969180283690      3.20049643339583
C           0.02884012006426     -5.10287452656365      4.52389021314320
C           1.51266271819065     -4.82891234610981      4.71924710881194
H           1.32083390426012     -2.81072563568327      5.43806685806846
H           1.89429369704194     -3.23028507375692      2.47677114095392
H          -0.70513615730434     -2.52432512968753      3.89894436772536
H           0.01166336625148     -5.06929132351677      2.37392896400637
H          -0.53539133268614     -4.64345791100297      5.34447139762422
H           2.08244395723349     -5.36564889131159      3.95062081429628
H           2.88746540553793     -3.15901815636831      4.71704446089453
H           1.51225752221482     -1.69377484969286      3.24418956929243
H          -1.54992755841055     -4.71593048280775      3.10444216002555
H          -0.17067529974348     -6.17744309285009      4.56475220499317
H           1.84431201419806     -5.21581307887242      5.68696396732568
C           4.45728976549726      1.16701382172169      0.54693339283778
C          -2.09221575783312     -2.98440559129071     -4.73910254943285
C           0.75567855440042      5.31829015579819     -4.16857839546109
C           2.95091026493545      1.36764980404677      0.50589399053646
C          -1.06374941335542     -2.32506236627012     -3.83002782321036
C           0.15278303634632      4.71360693737168     -2.90629115435441
C           2.45392339393751      2.22328824382153      1.66757068768754
C          -0.79390515365452     -3.19916529551815     -2.60697717273474
C           0.45311698424726      3.21964102615124     -2.82706531938585
C           2.90958834812541      1.64113526839171      3.00407982268934
C          -0.35939169902890     -4.60993397794508     -2.99573689955118
C           1.95392974150812      2.94709124759332     -2.91375060014129
C           4.41864499382182      1.43655910137373      3.03500572541365
C          -1.39704271263565     -5.25074289963047     -3.90956268996458
C           2.54278819566057      3.55720814735305     -4.17815399389969
C           4.89215070675916      0.57240541020076      1.87647910145840
```

```
 C          -1.66356327621581     -4.38992276133797     -5.13579282378954
 C           2.24982244932277      5.04781985818699     -4.26076971244324
 H           4.95441635816507      2.13245953324789      0.39569997955979
 H          -3.05365659182770     -3.03268311254299     -4.21318613985563
 H           0.25456170837478      4.88819133936799     -5.04415697563417
 H           2.45776630735282      0.38952905038542      0.56685379493510
 H          -0.13702483020286     -2.16436086967303     -4.38950444475110
 H           0.57510284559063      5.21567498891230     -2.02833669363264
 H           2.84844231563649      3.24067152590485      1.55802715079922
 H          -1.74237339416927     -3.28930528068400     -2.06324528445079
 H          -0.02297550528995      2.71814717588386     -3.67963853699604
 H           2.41114820604862      0.67528134389582      3.16219278957251
 H           0.60168400704095     -4.57127328915438     -3.51820070741869
 H           2.45802824082198      3.38368677435675     -2.04341274902276
 H           4.91341185337115      2.41390804784838      2.98350245858509
 H          -2.33136532968587     -5.38511945194667     -3.35127107880725
 H           2.11353434892922      3.05263727049542     -5.05209698008443
 H           4.46495983112091     -0.43342861780063      1.97716795621841
 H          -0.74930785784796     -4.32963453964011     -5.73907232982309
 H           2.76067701191788      5.56107299276324     -3.43670319060794
 H           4.75939872692359      0.52047164319903     -0.28196216476690
 H          -2.24749943604468     -2.36605377052732     -5.62767308525742
 H           0.55934052628709      6.39404097574702     -4.18829287067306
 H           2.65866215966695      1.80594522547906     -0.45066665882814
 H          -1.41600321485732     -1.33853276756926     -3.51083619612623
 H          -0.92552689705236      4.88923670790520     -2.88818935579572
 H           2.60780875639732      2.29126187852841      3.82843385434431
 H          -0.21178274916020     -5.22429647744668     -2.10275211811381
 H           2.14245762746957      1.86895609553911     -2.88591803285690
 H           4.70376242480105      0.98758962580060      3.99056807887228
 H          -1.05829262655694     -6.24716622860435     -4.20704497155787
 H           3.62099885759852      3.37624552928835     -4.20454504414281
 H           5.97944433558839      0.45946176930350      1.90603082519971
 H          -2.42788879486954     -4.85488710347817     -5.76486770136358
 H           2.65266016480635      5.46202218171261     -5.18935904539187
 C          -1.79834634446348      4.24910771770013      4.37865816570762
 C           3.92567921203512     -2.69633289638105     -3.38649750579767
 C          -4.18523224222531      2.25052927968570     -2.79213068144753
 C          -1.40037156815022      3.49735268078127      3.11575114087198
 C           2.46790712432724     -2.35894227729781     -3.10243038395849
 C          -2.67307038212295      2.08083726863075     -2.73295664517137
 C           0.11878094976109      3.37503951730541      3.01872782632026
 C           2.03716881585581     -2.86797231776207     -1.72751088324171
 C          -2.09161536268097      2.69361170600060     -1.45971188485526
 C           0.78946851808770      4.74520978295994      3.06489188027914
 C           2.96617421157274     -2.31408784074668     -0.64876823530105
 C          -2.78425161340902      2.13297561985718     -0.22035414814985
 C           0.37741964673463      5.49949608804938      4.32366088079495
 C           4.42110377978241     -2.65834847494855     -0.93309565150288
 C          -4.29317851251585      2.30977330598120     -0.29263985305065
 C          -1.13525635017106      5.61744366441523      4.43695995080885
 C           4.84679113748177     -2.15738466457938     -2.30389447818617
 C          -4.86079079039650      1.68046651766105     -1.55470407381776
 H          -1.49865760543182      3.66068186166952      5.25413198743052
 H           4.03392475373462     -3.78590991812999     -3.44725749282473
 H          -4.42312365058564      3.31774288430380     -2.87545373534733
 H          -1.78267010839131      4.04607848185962      2.24714105551214
 H           2.33223235988275     -1.26951825437019     -3.13297646301952
 H          -2.42837499456824      1.00997029441911     -2.75435838013603
```

```
  H           0.45576053731715      2.78907127864681      3.88391067083101
  H           2.07739939425857     -3.96393295172831     -1.71244473536063
  H          -2.22956384224732      3.78130057993542     -1.48103039908238
  H           0.49454176717938      5.32420607866540      2.18209224450527
  H           2.85590875111349     -1.22482213655719     -0.62474324569418
  H          -2.55141278388764      1.06439661286057     -0.14107925333090
  H           0.76512875392240      4.96558343727985      5.19957389719678
  H           4.55103252961023     -3.74595349844062     -0.88366927538023
  H          -4.53102794684606      3.38016971617345     -0.27999057812965
  H          -1.51160234874107      6.23415083904867      3.61141983013402
  H           4.80934865110355     -1.06090069455750     -2.31229821963342
  H          -4.69797660541066      0.59624313223019     -1.52071326611984
  H          -2.88667388952420      4.34858126263603      4.41917618868644
  H           4.20615520847723     -2.29527035617391     -4.36446450588407
  H          -4.56862322545880      1.76863483781609     -3.69584744801417
  H          -1.86030243244257      2.50427741349571      3.09798306869636
  H           1.83614845392633     -2.77808134644628     -3.88722566741005
  H          -2.21492008093766      2.52854730674855     -3.61798232567415
  H           1.87684523428335      4.64298874330171      3.03156211471765
  H           2.68674053283817     -2.68155853635024      0.34079730787641
  H          -2.39989647423253      2.60584585503668      0.68468538987196
  H           0.84055916166287      6.49026440880344      4.32535642680707
  H           5.05399036908267     -2.22645506168495     -0.15254640736205
  H          -4.75345539210761      1.87215835098357      0.59766675499226
  H          -1.40635776230959      6.13037026252417      5.36406865754340
  H           5.88277175173033     -2.44130328803322     -2.50899511881217
  H          -5.94188130452827      1.83722513285238     -1.60537193952458
```

Listing B.3: XYZ coordinates of the ground-state structure of $Cu_2(dcpm)_2(PF_6)_2$

```
Coordinates from ORCA-job Cu2DCPM2_GS_PBE0mecn E -6604.792776022844
  C           0.28218423630081      3.19812600867618      0.10777027844979
  P          -0.26281193790086      2.19541259011560     -1.33126195692560
  Cu          0.14710433211067     -0.00107267746664     -1.22919581215372
  P           0.31944134894668     -2.22608187958691     -1.40601687938297
  C          -0.09537579064622     -3.13406482490678      0.14175472670642
  P          -0.74543594798301     -2.08549719260851      1.50520196873503
  Cu         -0.23764721918864      0.09666333399342      1.44272419340738
  P           0.55982667793154      2.18984776305129      1.62010442060753
  H          -0.46118103265345      3.97316361512249      0.30762355562331
  H           1.21547512702987      3.70580527903126     -0.14745981052960
  H          -0.79280555075912     -3.94703157301208     -0.07188858420553
  H           0.82148664262213     -3.59658766477391      0.51191959187253
  C          -4.73830765352958     -2.30583176548197      0.33103575468658
  C          -3.22623029816694     -2.15532238817175      0.23531371806199
  C          -2.55502105777791     -2.37765483798368      1.58674211875692
  C          -3.15719314135358     -1.45994390598340      2.65203735064891
  C          -4.66655805256096     -1.63444313937226      2.74333338417553
  C          -5.32972029527278     -1.39636723815100      1.39600278375850
  H          -4.97726498703600     -3.34858645242526      0.57208654717811
  H          -2.97885414321023     -1.15340663434669     -0.13482958199422
  H          -2.70736598519788     -3.42195820546424      1.88372953048945
  H          -2.92785274657677     -0.41876569230191      2.38836741056933
  H          -4.89090549336449     -2.65174086231896      3.08596069147219
  H          -5.17810361166148     -0.35146323275725      1.10199549946009
  H          -5.18524481374257     -2.09533713878862     -0.64491523538506
  H          -2.84257516275471     -2.87005989106579     -0.49416644314510
  H          -2.69895512602288     -1.64843449746008      3.62628404880460
  H          -5.06876089279369     -0.95001549411653      3.49560800037395
```

```
H        -6.40980244761790     -1.55156521842731      1.46941920776844
C         1.98469910309656     -3.01802878651612      4.49067375071075
C         1.42689186151963     -2.50131597576453      3.17242968809170
C        -0.05747680730131     -2.83613357824402      3.03519196994673
C        -0.29920124866844     -4.33534117878855      3.17958204416495
C         0.26626775518262     -4.84694796396147      4.49944176424990
C         1.74361768464824     -4.51289907484956      4.64198651469710
H         1.50015014709920     -2.48494715758234      5.31760172149390
H         1.98474435934634     -2.96123429601514      2.34895171744495
H        -0.59217175978381     -2.31505839682717      3.83993911685004
H         0.18836660576642     -4.86289374679889      2.35174954510081
H        -0.29009781120934     -4.38987858339325      5.32671771876820
H         2.30952940188446     -5.04761596798974      3.86906879993734
H         3.05352922302093     -2.79319983823862      4.55099302504160
H         1.57517686354604     -1.42080096236025      3.08677596563808
H        -1.36601018328595     -4.56380507042160      3.11926023658531
H         0.10998465253496     -5.92710333028237      4.57147011360117
H         2.11968327075970     -4.86195240620569      5.60790949336435
C         4.42223649336840      0.97500878590064      0.76132278030322
C        -2.15533007550204     -2.57410340662701     -4.74568011982390
C         0.86781990978674      5.04613238157950     -4.18520884745857
C         2.91593096666912      1.15859790283919      0.67335341892526
C        -1.04690357311747     -2.02045236503742     -3.86069983440338
C         0.23803388864732      4.48590975328321     -2.91573461705767
C         2.38910979931038      2.09579990662160      1.75689979375939
C        -0.83235155294004     -2.93146739936248     -2.65357017503713
C         0.49803115647912      2.98736118423131     -2.79983775867340
C         2.81217010908043      1.61074858585625      3.14159671412887
C        -0.51291484276765     -4.36166402850179     -3.07735164442619
C         1.99181993698461      2.67217514605357     -2.86575800873181
C         4.31914556273166      1.40360034014963      3.22420634969076
C        -1.62013073804019     -4.90628433882857     -3.97149058359860
C         2.61100724050224      3.24033333656990     -4.13507099434220
C         4.82401470092163      0.46768014498487      2.13659286829471
C        -1.86015314754683     -4.00471830803930     -5.17430403314726
C         2.35558874395108      4.73581168826931     -4.25408865413349
H         4.91553415223322      1.93425774907416      0.56394413227322
H        -3.10121728300322     -2.54794316899673     -4.19053501246748
H         0.36521371452095      4.60843716610954     -5.05622554536370
H         2.42421159055017      0.18576705405054      0.80102130565730
H        -0.12576831669902     -1.93993602800147     -4.44530123956568
H         0.66733854883459      4.99602253794769     -2.04574333214506
H         2.78466303312514      3.10441595360799      1.58714404125785
H        -1.78369731426182     -2.95104879864756     -2.10858535490686
H         0.01624253980849      2.47896691136018     -3.64495515159715
H         2.30279081427637      0.66380720202618      3.35942833060774
H         0.43518439207866     -4.37920636475587     -3.62546892450794
H         2.49799013706025      3.10952456280415     -1.99664554352284
H         4.81902327556074      2.37467231209738      3.12428431999868
H        -2.54427421745759     -4.98252396540746     -3.38574491091563
H         2.17946774062214      2.72756416544056     -5.00321853976314
H         4.39534881543954     -0.53103177141753      2.28942481729330
H        -0.96801718407944     -4.01098198685009     -5.81283337373486
H         2.86970698449777      5.25462467752125     -3.43550364731430
H         4.75342470494765      0.28277161160173     -0.01811501771439
H        -2.28437278644530     -1.93180647401154     -5.62153295214565
H         0.69992692818690      6.12590111402916     -4.23261647721803
H         2.63654221373551      1.52009557082116     -0.31955380925939
H        -1.29396367861453     -1.00973692209279     -3.52370303635373
```

```
H        -0.83525476777498     4.69171193186391    -2.90904878959008
H         2.49807052888755     2.32204757299057     3.90869804452213
H        -0.38565775713018    -5.00404599567694    -2.20107826985712
H         2.14550788962523     1.58923457276922    -2.81303556700932
H         4.57732416417476     1.01612647877452     4.21387668173539
H        -1.36683053870218    -5.91902912985578    -4.29783188288261
H         3.68482990240441     3.03295847435099    -4.14544228340392
H         5.91032131913644     0.36043409241625     2.20302431728304
H        -2.68321880092427    -4.39556854893531    -5.77942326175095
H         2.77961501692886     5.11890796873579    -5.18666104738820
C        -1.93729823114299     4.07184977983875     4.36546843402754
C         3.88210015811513    -2.53884973861770    -3.51514855578733
C        -4.13296989666282     1.93284669824384    -2.79823705330453
C        -1.51167011365030     3.33559702749869     3.10230208441635
C         2.43837197197110    -2.19256273194936    -3.17660317909054
C        -2.62244618126315     1.77393656821800    -2.69471098850363
C         0.00860542968953     3.21374669058721     3.03736073707780
C         2.02258682716257    -2.77165930450903    -1.82443675307540
C        -2.06744739675005     2.48836465485456    -1.46354091652498
C         0.67510315884042     4.58467599740750     3.11198841394365
C         2.99505643993208    -2.32232063866729    -0.73634744284135
C        -2.77700189422750     2.00886217262377    -0.20033538269360
C         0.23733389032119     5.32639633485548     4.36936837771833
C         4.43340496216172    -2.67895865435335    -1.08070890797156
C        -4.28439039067688     2.17630189926757    -0.31236956783730
C        -1.27755573446965     5.44020994683834     4.45400412347563
C         4.83824268164923    -2.08954702908669    -2.42214236998380
C        -4.83024886828334     1.45449628770481    -1.53404155111751
H        -1.65562705561571     3.47335615109821     5.24020433303702
H         3.96753183919767    -3.62421138767128    -3.64724540977826
H        -4.37258174200417     2.98956971877435    -2.96678812174952
H        -1.87262997257978     3.89685734367729     2.23272134080469
H         2.32216114176541    -1.10094104989369    -3.14191895912920
H        -2.37587742697690     0.70705613239521    -2.61730645410227
H         0.32523387679486     2.62074860225123     3.90545914315544
H         2.01904639275976    -3.86691003991994    -1.87970949473213
H        -2.21981835169599     3.56958058519639    -1.56721204097020
H         0.39607660046804     5.17094410985134     2.22875817911847
H         2.91075386832737    -1.23624478719161    -0.62680190277100
H        -2.53556381652691     0.95016122868065    -0.03896975109446
H         0.60931107200538     4.78506131814564     5.24764274317426
H         4.53789318147925    -3.76998060520074    -1.11487280366788
H        -4.52214818592843     3.24453639110941    -0.38432045772788
H        -1.63829358394624     6.06617192945071     3.62842817151386
H         4.81969047897731    -0.99449420224022    -2.35326609938849
H        -4.66672192917222     0.37592295737016    -1.41840249675092
H        -3.02639689519602     4.17012339767317     4.38465059027036
H         4.14906125703364    -2.08174425062485    -4.47220393591293
H        -4.49766904664158     1.38197524937219    -3.66989473786434
H        -1.97227705163398     2.34369526981639     3.06065851429062
H         1.78114781211830    -2.55677227904061    -3.96766393272422
H        -2.14534342986975     2.14408941261359    -3.60531772184883
H         1.76338181396694     4.48639831979651     3.09778356465712
H         2.73120434656939    -2.75850779504564     0.22923245245845
H        -2.40971676155888     2.54775308444177     0.67328146296885
H         0.69792240783474     6.31822169949867     4.38990049743987
H         5.09499842713878    -2.32080397309835    -0.28649035544051
H        -4.76202648729099     1.80921446779604     0.60037759499917
H        -1.56835275907726     5.94168396133078     5.38145564028107
```

```
H           5.86401992295520     -2.37510624627892     -2.67163269168215
H          -5.91052529178124      1.60471992064532     -1.61464910085267
```

Appendix C

List of hazardous substances according to GHS

The following table summarizes the hazardous substances used during the synthesis and characterization of metal complexes in this work. Hazard classifications are based on the Globally Harmonized System (GHS) and corresponding Safety Data Sheets (SDS). The major hazard statements (H-codes) and signal words are listed for each substance.

Substance	GHS	Signal Word	Major H-Statements
Acetonitrile (MeCN)	GHS02, GHS07	Danger	H225, H302, H332
Chloroform	GHS06, GHS08	Danger	H302, H331, H351
Diethyl ether	GHS02	Danger	H225, H336
Diethyl phosphite	GHS07	Warning	H315, H319 (check SDS)
Sodium metal	GHS01, GHS09	Danger	H260, H290
Pyridine-N-oxide	GHS07	Warning	H315, H319
Dimethyl sulfate	GHS06, GHS08	Danger	H300, H330, H341
Lithium aluminium hydride ($LiAlH_4$)	GHS01, GHS03, GHS05	Danger	H260, H271, H290
Paraformaldehyde	GHS06, GHS07, GHS08	Danger	H301, H311, H317, H351
Ethanol	GHS02	Warning	H225, H319

Substance	**GHS Pictogram(s)**	**Signal Word**	**Major H-Statements**
Tetrachloroauric(III) acid hydrate	GHS05, GHS07	Danger	H290, H314
`[Au(tht)Cl]`	GHS07	Warning	H315, H319 (check SDS)
Dichloromethane (DCM)	GHS06, GHS08	Danger	H302, H315, H319, H332, H351
K[$AuCl_4$]	GHS05, GHS07	Danger	H290, H315, H319 (check SDS)
Methanol	GHS02, GHS06	Danger	H225, H301, H311, H331, H370
Thiodiglycol	GHS07	Warning	H315, H319, H335 (check SDS)
Bis(dicyclohexylphosphino)methane	GHS07	Warning	H315, H319 (check SDS)
NH_4PF_6	GHS07	Warning	H302, H315 (check SDS)
Silver hexafluorophosphate ($AgPF_6$)	GHS07	Warning	H302, H319 (check SDS)
Hydrofluoric acid (HF)	GHS05, GHS06	Danger	H300 + H310 + H330, H314, H290

Acknowledgment

The past four years of my PhD journey have been an incredible learning experience, filled with invaluable knowledge, challenges, and personal growth. This journey would not have been possible without the unwavering support, guidance, and encouragement of many wonderful people from all around the world.

First and foremost, I would like to express my deepest gratitude to Dr. Chris Milne and Dr. Dmitry Khakhulin for offering me the opportunity to pursue my PhD within the FXE group at European XFEL. Their mentorship, guidance, and continuous support over the years have played a crucial role in shaping my research career. The opportunities I had—ranging from networking and conducting experiments to attending conferences and publishing my work—were all made possible through their encouragement and support. A special thanks to Dmitry, who has dedicated countless hours to discussions on improving my skills, analyzing data, and even guiding me in shaping my future aspirations. Our timeless conversations on various topics have been invaluable to my academic and personal growth.

I am also sincerely grateful to Prof. Dr. Dorota Koziej, my academic supervisor from the University of Hamburg, for her insightful advice and guidance in aligning my project.

My heartfelt thanks go to my colleagues at FXE, whose support and encouragement have enriched my time at European XFEL. I would like to extend my appreciation to Dr. Peter Zalden, Dr. Frederico Alves Lima, Dr. Mykola Biednov, Dr. Yifeng Jiang, Dr. Hao Wang, Dr. Han Xu, Dr. Yohei Uemura, Dr. Hazem Yousef, Martin Knoll, and Paul Frankenberger for their collaboration, support, and for fostering a positive and stimulating research environment. Additionally, I am grateful to the European XFEL staff members and fellow PhD students for their assistance on various occasions. A special thanks to Dr. Vasilii Bazhenov for his support with chemical synthesis in the chemistry lab, as well as for managing the storage and ordering of required chemicals over an extended period.

I would also like to extend my gratitude to IMPRS-UFAST graduate school at CFEL, DESY, under which my PhD was conducted. A special thanks to Dr. Neda Lotfiomran for her continuous support throughout my PhD journey. I am also thankful to Dr. Aleksandr Kalinko and Dr. Maria Naumova for their guidance and assistance

during my beamtime at P64 and data analysis. Additionally, I am grateful to Prof. Dr. Evamarie Hey-Hawkins and her PostDoc. Peter Wonneberger from Universität Leipzig for their support for successful synthesis of my complexes. I would like to thank Prof. Dr. Axel Jacobi von Wangelin from the University of Hamburg for his support and for providing me with the opportunity to work in his laboratory. Much of my hands-on experience and scientific expertise has been gained through beamtime participation at European XFEL, as well as during experimental beamtime at PETRA and ESRF. These experiences have significantly shaped my research skills and scientific understanding.

Beyond scientific activities, the friendships and memories I have shared with colleagues and friends have made my time in Hamburg even more meaningful. A special mention goes to my FXE office mates—Martin, Paul, Hao, and Han—for their humor, laughter, and everyday chit-chat, which brought joy and relief during the intense PhD years. I would also like to thank my fellow PhD colleagues at European XFEL for their companionship, especially during the thesis-writing phase; our regular monthly meetings provided much-needed motivation and a welcome escape from the stresses of writing. I am also deeply appreciative of the support I received during my various business trips, which allowed me to engage in scientific exchanges and explore new places.

Most importantly, I would like to express my heartfelt gratitude to my parents, whose unconditional love and support have enabled me to fulfill my dream of earning a PhD. A special thanks to my brother, who has supported me in every possible way throughout this journey. I am also deeply grateful to my friends in Hamburg and my extended family for their constant encouragement and belief in me.

Finally, my deepest and most heartfelt appreciation goes to my husband and my 4-year-old daughter. Completing a PhD while raising a child has been an immense challenge, but your unwavering love, patience, and support made it possible. Without you both, this journey would have been infinitely harder, and I am forever grateful to have you in my life.

To everyone who has been a part of this journey—thank you. And to you, the reader, thank you for taking the time to read my thesis.

Bibliography

[1] Wilhelm Conrad Röntgen. On a new kind of rays. *Science*, 3(59):227–231, 1896.

[2] Hubert Schmidbaur and Annette Schier. Aurophilic interactions as a subject of current research: an up-date. *Chemical Society Reviews*, 41(1):370–412, 2012.

[3] Saravanan Raju, Harkesh B Singh, and Ray J Butcher. Metallophilic interactions: observations of the shortest metallophilicinteractions between closed shell (d 10 d 10, d 10 d 8, d 8 d 8) metal ions [m m′ m= hg (ii) and pd (ii) and m′= cu (i), ag (i), au (i), and pd (ii)]. *Dalton Transactions*, 49(26):9099–9117, 2020.

[4] Jing Qian, Zhucheng Yang, Jingkuan Lyu, Qiaofeng Yao, and Jianping Xie. Molecular interactions in atomically precise metal nanoclusters. *Precision Chemistry*, 2(10):495–517, 2024.

[5] Guillermo Romo-Islas and Raquel Gavara. Recent progress on supramolecular luminescent assemblies based on aurophilic interactions in solution. *Inorganics*, 9(5):32, 2021.

[6] Lin X Chen, Wighard JH Jager, Guy Jennings, David J Gosztola, Anneli Munkholm, and Jan P Hessler. Capturing a photoexcited molecular structure through time-domain x-ray absorption fine structure. *Science*, 292(5515):262–264, 2001.

[7] Ahmed H Zewail. Femtochemistry: Atomic-scale dynamics of the chemical bond. *The Journal of Physical Chemistry A*, 104(24):5660–5694, 2000.

[8] Xu Liu, Xiao Cai, and Yan Zhu. Catalysis synergism by atomically precise bimetallic nanoclusters doped with heteroatoms. *Accounts of Chemical Research*, 56(12):1528–1538, 2023.

[9] Yanyan Qin, Pengfei She, and Wai-Yeung Wong. Recent advances in dynamically photo-responsive metal complexes for optoelectronic applications. *The Innovation Materials*, 2(4):100099–1, 2024.

[10] Grace C Thaggard, Johanna Haimerl, Kyoung Chul Park, Jaewoong Lim, Roland A Fischer, Buddhima KP Maldeni Kankanamalage, Brandon J Yarbrough, Gina R Wilson, and Natalia B Shustova. Metal–photoswitch friendship: from photochromic complexes to functional materials. *Journal of the American Chemical Society*, 144(51):23249–23263, 2022.

[11] Huayun Shi, Rafael C Marchi, and Peter J Sadler. Advances in the design of photoactivatable metallodrugs: Excited state metallomics. *Angewandte Chemie International Edition*, 64(9):e202423335, 2025.

[12] Xiaohui Wang, Xiaoyong Wang, Suxing Jin, Nafees Muhammad, and Zijian Guo. Stimuli-responsive therapeutic metallodrugs. *Chemical reviews*, 119(2):1138–1192, 2018.

[13] Peter William Atkins, Julio De Paula, and James Keeler. *Atkins' physical chemistry*. Oxford university press, 2023.

[14] JS Griffith and LE Orgel. Ligand-field theory. *Quarterly Reviews, Chemical Society*, 11(4):381–393, 1957.

[15] James Franck and EG Dymond. Elementary processes of photochemical reactions. *Transactions of the Faraday Society*, 21(February):536–542, 1926.

[16] Melvin Lax. The franck-condon principle and its application to crystals. *The Journal of chemical physics*, 20(11):1752–1760, 1952.

[17] Joseph R Lakowicz. *Principles of fluorescence spectroscopy*. Springer, 2006.

[18] Hubert Schmidbaur and Annette Schier. A briefing on aurophilicity. *Chemical Society Reviews*, 37(9):1931–1951, 2008.

[19] Qingshu Zheng, Stefan Borsley, Gary S Nichol, Fernanda Duarte, and Scott L Cockroft. The energetic significance of metallophilic interactions. *Angewandte Chemie*, 131(36):12747–12753, 2019.

[20] Pekka Pyykkö. Strong closed-shell interactions in inorganic chemistry. *Chemical reviews*, 97(3):597–636, 1997.

[21] Pekka Pyykkö, Jian Li, and Nino Runeberg. Predicted ligand dependence of the au (i)... au (i) attraction in (xauph3) 2. *Chemical physics letters*, 218(1-2):133–138, 1994.

[22] Oliver Schuster, Uwe Monkowius, Hubert Schmidbaur, R Shyama Ray, Sven Krüger, and Notker Rösch. Unexpected structural preference for aggregates

with metallophilic ag—au contacts in (trimethylphosphine) silver (i) and-gold (i) phenylethynyl complexes. an experimental and theoretical study. *Organometallics*, 25(4):1004–1011, 2006.

[23] Alba Vellé, Luis Rodríguez-Santiago, Mariona Sodupe, and Pablo J Sanz Miguel. Enhanced metallophilicity in metal–carbene systems: Stronger character of aurophilic interactions in solution. *Chemistry–A European Journal*, 26(5):997–1002, 2020.

[24] Marco Baron, Cristina Tubaro, Andrea Biffis, Marino Basato, Claudia Graiff, Albert Poater, Luigi Cavallo, Nicola Armaroli, and Gianluca Accorsi. Blue-emitting dinuclear n-heterocyclic dicarbene gold (i) complex featuring a nearly unit quantum yield. *Inorganic Chemistry*, 51(3):1778–1784, 2012.

[25] Claudia Bizzarri, Eduard Spuling, Daniel M Knoll, Daniel Volz, and Stefan Bräse. Sustainable metal complexes for organic light-emitting diodes (oleds). *Coordination Chemistry Reviews*, 373:49–82, 2018.

[26] Qingyun Wan, Jun Yang, Wai-Pong To, and Chi-Ming Che. Strong metal–metal pauli repulsion leads to repulsive metallophilicity in closed-shell d8 and d10 organometallic complexes. *Proceedings of the National Academy of Sciences*, 118(1):e2019265118, 2021.

[27] Kirsty M Anderson, Andrés E Goeta, and Jonathan W Steed. Au au interactions: Z ‘> 1 behavior and structural analysis. *Inorganic chemistry*, 46(16):6444–6451, 2007.

[28] Michael J Katz, Ken Sakai, and Daniel B Leznoff. The use of aurophilic and other metal–metal interactions as crystal engineering design elements to increase structural dimensionality. *Chemical Society Reviews*, 37(9):1884–1895, 2008.

[29] John E Bercaw, Alec C Durrell, Harry B Gray, Jennifer C Green, Nilay Hazari, Jay A Labinger, and Jay R Winkler. Electronic structures of pdii dimers. *Inorganic chemistry*, 49(4):1801–1810, 2010.

[30] Chi-Ming Che, Man-Chung Tse, Michael CW Chan, Kung-Kai Cheung, David Lee Phillips, and King-Hung Leung. Spectroscopic evidence for argentophilicity in structurally characterized luminescent binuclear silver (i) complexes. *Journal of the American Chemical Society*, 122(11):2464–2468, 2000.

[31] María Jose Mayoral, Christina Rest, Vladimir Stepanenko, Jennifer Schellheimer, Rodrigo Q Albuquerque, and Gustavo Fernandez. Cooperative supramolecular

polymerization driven by metallophilic pd··· pd interactions. *Journal of the American Chemical Society*, 135(6):2148–2151, 2013.

[32] Pekka Pyykkö, Nino Runeberg, and Fernando Mendizabal. Theory of the d10–d10 closed-shell attraction: 1. dimers near equilibrium. *Chemistry–A European Journal*, 3(9):1451–1457, 1997.

[33] Holger L Hermann, Gernot Boche, and Peter Schwerdtfeger. Metallophilic interactions in closed-shell copper (i) compounds—a theoretical study. *Chemistry–A European Journal*, 7(24):5333–5342, 2001.

[34] Balazs Pinter, Lies Broeckaert, Jan Turek, Aleš Ržička, and Frank De Proft. Dimers of n-heterocyclic carbene copper, silver, and gold halides: probing metallophilic interactions through electron density based concepts. *Chemistry–A European Journal*, 20(3):734–744, 2014.

[35] Peter Schwerdtfeger, Alice E Bruce, and Mitchell RM Bruce. Theoretical studies on the photochemistry of the cis-to-trans conversion in dinuclear gold halide bis (diphenylphosphino) ethylene complexes. *Journal of the American Chemical Society*, 120(26):6587–6597, 1998.

[36] Vivian Wing-Wah Yam, Vonika Ka-Man Au, and Sammual Yu-Lut Leung. Light-emitting self-assembled materials based on d8 and d10 transition metal complexes. *Chemical reviews*, 115(15):7589–7728, 2015.

[37] Sei Otsuka. Chemistry of platinum and palladium compounds of bulky phosphines. *Journal of Organometallic Chemistry*, 200(1):191–205, 1980.

[38] Héctor De La Riva, Aranzazu Pintado-Alba, Mark Nieuwenhuyzen, Christopher Hardacre, and M Cristina Lagunas. First exafs studies on aurophilic interactions in solution. *Chemical Communications*, (39):4970–4972, 2005.

[39] Yuning Hong, Jacky WY Lam, and Ben Zhong Tang. Aggregation-induced emission. *Chemical Society Reviews*, 40(11):5361–5388, 2011.

[40] Morten Christensen, Kristoffer Haldrup, Klaus Bechgaard, Robert Feidenhans'l, Qingyu Kong, Marco Cammarata, Manuela Lo Russo, Michael Wulff, Niels Harrit, and Martin Meedom Nielsen. Time-resolved x-ray scattering of an electronically excited state in solution. structure of the 3a2u state of tetrakis-μ-pyrophosphitodiplatinate (ii). *Journal of the American Chemical Society*, 131(2):502–508, 2009.

[41] Kristoffer Haldrup, Gianluca Levi, Elisa Biasin, Peter Vester, Mads Goldschmidt Laursen, Frederik Beyer, Kasper Skov Kjær, Tim Brandt Van Driel, Tobias Harlang, Asmus O Dohn, et al. Ultrafast x-ray scattering measurements of coherent structural dynamics on the ground-state potential energy surface of a diplatinum molecule. *Physical review letters*, 122(6):063001, 2019.

[42] Kristoffer Haldrup, Tobias Harlang, Morten Christensen, Asmus Dohn, Tim Brandt van Driel, Kasper Skov Kjær, Niels Harrit, Johan Vibenholt, Laurent Guerin, Michael Wulff, et al. Bond shortening (1.4 å) in the singlet and triplet excited states of [ir2 (dimen) 4] 2+ in solution determined by time-resolved x-ray scattering. *Inorganic chemistry*, 50(19):9329–9336, 2011.

[43] Franz Scherbaum, Andreas Grohmann, Brigitte Huber, Carl Krüger, and Hubert Schmidbaur. "aurophilicity" as a consequence of relativistic effects: the hexakis (triphenylphosphaneaurio) methane dication [(ph3pau) 6c] 2. *Angewandte Chemie International Edition in English*, 27(11):1544–1546, 1988.

[44] Hubert Schmidbaur. Ludwig mond lecture. high-carat gold compounds. *Chemical Society Reviews*, 24(6):391–400, 1995.

[45] Salam Al-Baker, William E Hill, and Charles A McAuliffe. Novel ring compounds of bidentate phosphines with gold (i). two-, three-, and four-co-ordination. *Journal of the Chemical Society, Dalton Transactions*, (12):2655–2659, 1985.

[46] Hubert Schmidbaur, Anette Wohlleben, Fritz Wagner, Olli Orama, and Gottfried Huttner. Gold-komplexe von diphosphinomethanen, i. synthese und kristallstruktur zweikerniger gold (i)-verbindungen. *Chemische Berichte*, 110(5):1748–1754, 1977.

[47] Wen-Fu Fu, Kwok-Chu Chan, Vincent M Miskowski, and Chi-Ming Che. The intrinsic 3 [dσ* pσ] emission of binuclear gold (i) complexes with two bridging diphosphane ligands lies in the near uv; emissions in the visible region are due to exciplexes. *Angewandte Chemie International Edition*, 38(18):2783–2785, 1999.

[48] Wen-Fu Fu, Kwok-Chu Chan, Kung-Kai Cheung, and Chi-Ming Che. Substrate-binding reactions of the 3 [dσ* pσ] excited state of binuclear gold (i) complexes with bridging bis (dicyclohexylphosphino) methane ligands: Emission and time-resolved absorption spectroscopic studies. *Chemistry–A European Journal*, 7(21):4656–4664, 2001.

[49] Hong-Xing Zhang and Chi-Ming Che. Aurophilic attraction and luminescence of binuclear gold (i) complexes with bridging phosphine ligands: Ab initio study. *Chemistry–A European Journal*, 7(22):4887–4893, 2001.

[50] Chensheng Ma, Chris Tsz-Leung Chan, Wai-Pong To, Wai-Ming Kwok, and Chi-Ming Che. Deciphering photoluminescence dynamics and reactivity of the luminescent metal–metal-bonded excited state of a binuclear gold (i) phosphine complex containing open coordination sites. *Chemistry–A European Journal*, 21(40):13888–13893, 2015.

[51] Hubert Schmidbaur and Helgard G Raubenheimer. Excimer and exciplex formation in gold (i) complexes preconditioned by aurophilic interactions. *Angewandte Chemie International Edition*, 59(35):14748–14771, 2020.

[52] Marcel JP Schmitt, Sebastian V Kruppa, Simon P Walg, Werner R Thiel, Wim Klopper, and Christoph Riehn. Electronic spectroscopy of homo-and heterometallic binuclear coinage metal phosphine complexes in isolation. *Physical Chemistry Chemical Physics*, 25(31):20880–20891, 2023.

[53] Martin B Smith, Sophie H Dale, Simon J Coles, Thomas Gelbrich, Michael B Hursthouse, and Mark E Light. Isomeric dinuclear gold (i) complexes with highly functionalised ditertiary phosphines: Self-assembly of dimers, rings and 1-d polymeric chains. *CrystEngComm*, 8(2):140–149, 2006.

[54] Alexander A Penney, Vladimir V Sizov, Elena V Grachova, Dmitry V Krupenya, Vladislav V Gurzhiy, Galina L Starova, and Sergey P Tunik. Aurophilicity in action: Fine-tuning the gold (i)–gold (i) distance in the excited state to modulate the emission in a series of dinuclear homoleptic gold (i)–nhc complexes. *Inorganic Chemistry*, 55(10):4720–4732, 2016.

[55] Elvira I Musina, Vera V Khrizanforova, Igor D Strelnik, Murad I Valitov, Yulia S Spiridonova, Dmitry B Krivolapov, Igor A Litvinov, Marsil K Kadirov, Peter Lönnecke, Evamarie Hey-Hawkins, et al. New functional cyclic aminomethylphosphine ligands for the construction of catalysts for electrochemical hydrogen transformations. *Chemistry–A European Journal*, 20(11):3169–3182, 2014.

[56] Julia Elistratova, Igor Strelnik, Konstantin Brylev, Michael A Shestopalov, Tatiana Gerasimova, Vasily Babaev, Kirill Kholin, Alexey Dobrynin, Elvira Musina, Sergey Katsyuba, et al. Novel water soluble cationic au (i) complexes with cyclic pnnp ligand as building blocks for heterometallic supramolecular assemblies with anionic hexarhenium cluster units. *Journal of Luminescence*, 196:485–491, 2018.

[57] Nataliya A Shamsutdinova, Igor D Strelnik, Elvira I Musina, Tatyana P Gerasimova, Sergey A Katsyuba, Vasily M Babaev, Dmitry B Krivolapov, Igor A Litvinov, Asiya R Mustafina, Andrey A Karasik, et al. “host–guest” binding of a luminescent dinuclear au (i) complex based on cyclic diphosphine with organic

substrates as a reason for luminescence tuneability. *New Journal of Chemistry*, 40(11):9853–9861, 2016.

[58] Irina R Dayanova, Adelina I Fayezova, Igor D Strelnik, Igor A Litvinov, Daut R Islamov, Ilya E Kolesnikov, Tatiana P Gerasimova, Elvira I Musina, and Andrey A Karasik. Aurophilic interactions of dimeric bisphosphine gold (i) complexes preorganized by the structure of the 1, 5-diaza-3, 7-diphosphacyclooctanes. *Inorganics*, 10(12):224, 2022.

[59] Alexander Frank Wells. *Structural inorganic chemistry.* OUP Oxford, 2012.

[60] Hubert Schmidbaur and Annette Schier. Argentophilic interactions. *Angewandte Chemie International Edition*, 54(3):746–784, 2015.

[61] Sebastian Volker Kruppa, Florian Bäppler, Willem Klopper, Simon P Walg, Werner Richard Thiel, Rolf Diller, and Christoph Riehn. Ultrafast excited-state relaxation of a binuclear ag (i) phosphine complex in gas phase and solution. *Physical Chemistry Chemical Physics*, 19(34):22785–22800, 2017.

[62] Prem K Mehrotra and Roald Hoffmann. Copper (i)-copper (i) interactions. bonding relationships in d10-d10 systems. *Inorganic Chemistry*, 17(8):2187–2189, 1978.

[63] F Albert Cotton, Carlos A Murillo, and Richard A Walton. *Multiple bonds between metal atoms.* Springer Science & Business Media, 2006.

[64] Vivian Wing-Wah Yam and Kenneth Kam-Wing Lo. Luminescent polynuclear d 10 metal complexes. *Chemical Society Reviews*, 28(5):323–334, 1999.

[65] Peter Schwerdtfeger and Graham A Bowmaker. Relativistic effects in gold chemistry. v. group 11 dipole polarizabilities and weak bonding in monocarbonyl compounds. *The Journal of chemical physics*, 100(6):4487–4497, 1994.

[66] NV Satyachand Harisomayajula, Serhii Makovetskyi, and Yi-Chou Tsai. Cuprophilic interactions in and between molecular entities. *Chemistry–A European Journal*, 25(38):8936–8954, 2019.

[67] Pekka Pyykko. Relativistic effects in structural chemistry. *Chemical Reviews*, 88(3):563–594, 1988.

[68] David Lee Phillips, Chi-Ming Che, King Hung Leung, Zhong Mao, and Man-Chung Tse. A comparative study on metal–metal interaction in binuclear two-and three-coordinated d10-metal complexes: Spectroscopic investigation of m (i)–m (i) interaction in the 1 [dσ* pσ] excited state of [m2 (dcpm) 2] 2+(dcpm= bis

(dicyclohexylphosphino) methane)(m= au, ag, cu) and [m2 (dmpm) 3] 2+(dmpm= bis (dimethylphosphino) methane)(m= au, ag, cu) complexes. *Coordination chemistry reviews*, 249(13-14):1476–1490, 2005.

[69] Daniel B Leznoff, Bao-Yu Xue, Raymond J Batchelor, Frederick WB Einstein, and Brian O Patrick. Gold- gold interactions as crystal engineering design elements in heterobimetallic coordination polymers. *Inorganic Chemistry*, 40(23):6026–6034, 2001.

[70] RR Ramazanov, AI Kononov, AM Nesterenko, JR Shakirova, IO Koshevoy, EV Grachova, and SP Tunik. Luminescence switching of a gold–copper supramolecular complex: A physical insight. *The Journal of Physical Chemistry C*, 120(44):25541–25547, 2016.

[71] Ryosuke Kobayashi, Takashi Yumura, Hiroaki Imoto, and Kensuke Naka. Homo- and hetero-metallophilicity-driven synthesis of highly emissive and stimuli-responsive au (i)–cu (i) double salts. *Chemical Communications*, 57(44):5382–5385, 2021.

[72] Lucas de Azevedo Santos, Timon Wagner, Klaas Visscher, Jörn Nitsch, F Matthias Bickelhaupt, and Célia Fonseca Guerra. The nature of metallophilic interactions in closed-shell d 8–d 8 metal complexes. *Physical Chemistry Chemical Physics*, 26(31):20928–20936, 2024.

[73] MN Rosenbluth. High energy elastic scattering of electrons on protons. *Physical Review*, 79(4):615, 1950.

[74] Herman Feshbach. Elastic scattering of electrons. *Physical Review*, 84(6):1206, 1951.

[75] P Eisenberger and PM Platzman. Compton scattering of x rays from bound electrons. *Physical Review A*, 2(2):415, 1970.

[76] Malcolm Cooper, Peter Mijnarends, Nobuhiro Shiotani, Nobuhiko Sakai, and Arun Bansil. *X-ray Compton scattering*, volume 5. OUP Oxford, 2004.

[77] Hyotcherl Ihee, Michael Wulff, Jeongho Kim, and Shin-ichi Adachi. Ultrafast x-ray scattering: structural dynamics from diatomic to protein molecules. *International Reviews in Physical Chemistry*, 29(3):453–520, 2010.

[78] Bertram Eugene Warren. *X-ray Diffraction*. Courier Corporation, 1990.

[79] Jens Als-Nielsen and Des McMorrow. *Elements of modern X-ray physics*. John Wiley & Sons, 2011.

[80] Qingyu Kong, Joonghan Kim, Maciej Lorenc, Tae Kyu Kim, Hyotcherl Ihee, and Michael Wulff. Photodissociation reaction of 1, 2-diiodoethane in solution: A theoretical and x-ray diffraction study. *The Journal of Physical Chemistry A*, 109(45):10451–10458, 2005.

[81] Kasper Skov Kjær, Tim B Van Driel, Jan Kehres, Kristoffer Haldrup, Dmitry Khakhulin, Klaus Bechgaard, Marco Cammarata, Michael Wulff, Thomas Just Sørensen, and Martin M Nielsen. Introducing a standard method for experimental determination of the solvent response in laser pump, x-ray probe time-resolved wide-angle x-ray scattering experiments on systems in solution. *Physical Chemistry Chemical Physics*, 15(36):15003–15016, 2013.

[82] Hyotcherl Ihee, Maciej Lorenc, Tae Kyu Kim, Qin Y Kong, Marco Cammarata, Jae Hyuk Lee, Savo Bratos, and Michael Wulff. Ultrafast x-ray diffraction of transient molecular structures in solution. *Science*, 309(5738):1223–1227, 2005.

[83] Matthew Newville. Fundamentals of x-ray absorption fine structure. *Consortium for Advanced Radiation Sources, University of Chicago (USA)[http://xafs. org]*, 2004.

[84] Hans Joachim Eichler and Jürgen Eichler. *Laser: Bauformen, Strahlführung, Anwendungen.* Springer-Verlag, 2015.

[85] Diek C Koningsberger and Roelof Prins. X-ray absorption: principles, applications, techniques of exafs, sexafs and xanes. 1987.

[86] James E Penner-Hahn et al. X-ray absorption spectroscopy. *Comprehensive Coordination Chemistry II*, 2:159–186, 2003.

[87] John J Rehr and Robert C Albers. Theoretical approaches to x-ray absorption fine structure. *Reviews of modern physics*, 72(3):621, 2000.

[88] Edward A Stern. Theory of the extended x-ray-absorption fine structure. *Physical Review B*, 10(8):3027, 1974.

[89] SI Zabinsky, JJ Rehr, A Ankudinov, RC Albers, and MJ Eller. Multiple-scattering calculations of x-ray-absorption spectra. *Physical Review B*, 52(4):2995, 1995.

[90] JJ Rehr, RC Albers, CR Natoli, and EA Stern. New high-energy approximation for x-ray-absorption near-edge structure. *Physical Review B*, 34(6):4350, 1986.

[91] Grant Bunker. *Introduction to XAFS: a practical guide to X-ray absorption fine structure spectroscopy.* Cambridge University Press, 2010.

[92] Dale E Sayers, Edward A Stern, and Farrel W Lytle. New technique for investigating noncrystalline structures: Fourier analysis of the extended x-ray—absorption fine structure. *Physical review letters*, 27(18):1204, 1971.

[93] John J Rehr, Joshua J Kas, Micah P Prange, Adam P Sorini, Yoshinari Takimoto, and Fernando Vila. Ab initio theory and calculations of x-ray spectra. *Comptes Rendus Physique*, 10(6):548–559, 2009.

[94] G Ganyushin, A Hansen, R Izsak, DG Liakos, C Kollmar, S Kossmann, DA Pantazis, T Petrenko, C Reimann, C Riplinger, et al. Orca an ab initio, dft and semiempirical scf-mo package.

[95] Frank Neese, Frank Wennmohs, Ute Becker, and Christoph Riplinger. The orca quantum chemistry program package. *The Journal of chemical physics*, 152(22), 2020.

[96] Brianna Stewart, Derrick J Hylton, and Natarajan Ravi. A systematic approach for understanding slater–gaussian functions in computational chemistry. *Journal of Chemical Education*, 90(5):609–612, 2013.

[97] G t Te Velde, Friedrich Matthias Bickelhaupt, Evert Jan Baerends, C Fonseca Guerra, Stan JA van Gisbergen, Jaap G Snijders, and Tom Ziegler. Chemistry with adf. *Journal of Computational chemistry*, 22(9):931–967, 2001.

[98] M Benfatto, A Congiu-Castellano, A Daniele, and S Della Longa. Mxan: a new software procedure to perform geometrical fitting of experimental xanes spectra. *Synchrotron Radiation*, 8(2):267–269, 2001.

[99] Marco Giorgetti, Stefano Della Longa, and Maurizio Benfatto. Exafs and xanes simulations of fe/co hexacyanoferrate spectra by gnxas and mxan. In *Journal of Physics: Conference Series*, volume 190, page 012145. IOP Publishing, 2009.

[100] Sandro Scandolo, Paolo Giannozzi, Carlo Cavazzoni, Stefano de Gironcoli, Alfredo Pasquarello, and Stefano Baroni. First-principles codes for computational crystallography in the quantum-espresso package. *Zeitschrift für Kristallographie-Crystalline Materials*, 220(5-6):574–579, 2005.

[101] Paolo Giannozzi, Stefano Baroni, Nicola Bonini, Matteo Calandra, Roberto Car, Carlo Cavazzoni, Davide Ceresoli, Guido L Chiarotti, Matteo Cococcioni, Ismaila Dabo, et al. Quantum espresso: a modular and open-source software project for quantumsimulations of materials. *Journal of physics: Condensed matter*, 21(39):395502, 2009.

[102] John J Rehr, Joshua J Kas, Fernando D Vila, Micah P Prange, and Kevin Jorissen. Parameter-free calculations of x-ray spectra with feff9. *Physical Chemistry Chemical Physics*, 12(21):5503–5513, 2010.

[103] Y Chen, FJ Garcia De Abajo, A Chassé, RX Ynzunza, AP Kaduwela, MA Van Hove, and CS Fadley. Convergence and reliability of the rehr-albers formalism in multiple-scattering calculations of photoelectron diffraction. *Physical Review B*, 58(19):13121, 1998.

[104] Bruce Ravel. A practical introduction to multiple scattering theory. *Journal of Alloys and compounds*, 401(1-2):118–126, 2005.

[105] Kevin Jorissen, Fernando D Vila, and John J Rehr. A high performance scientific cloud computing environment for materials simulations. *Computer Physics Communications*, 183(9):1911–1919, 2012.

[106] B Ravel and M Newville. Athena and artemis: interactive graphical data analysis using ifeffit. *Physica Scripta*, 2005(T115):1007, 2005.

[107] Bruce Ravel and Matthew Newville. Athena and artemis. 2024.

[108] Joshua J Kas, FD Vila, and JJ Rehr. The feff code. *International Tables for Crystallography*, 1, 2020.

[109] Walter Kohn and Lu Jeu Sham. Self-consistent equations including exchange and correlation effects. *Physical review*, 140(4A):A1133, 1965.

[110] Frank Neese. The orca program system. *Wiley Interdisciplinary Reviews: Computational Molecular Science*, 2(1):73–78, 2012.

[111] Frank Neese. Software update: The orca program system—version 5.0. *Wiley Interdisciplinary Reviews: Computational Molecular Science*, 12(5):e1606, 2022.

[112] Vincenzo Barone and Maurizio Cossi. Quantum calculation of molecular energies and energy gradients in solution by a conductor solvent model. *The Journal of Physical Chemistry A*, 102(11):1995–2001, 1998.

[113] James Clerk Maxwell. Viii. a dynamical theory of the electromagnetic field. *Philosophical transactions of the Royal Society of London*, (155):459–512, 1865.

[114] Hendrik Antoon Lorentz. Attempt of a theory of electrical and optical phenomena in moving bodies; versuch einer theorie der electrischen und optischen erscheinungen in bewegten körpern. *Versuch einer Theorie der Electrischen und Optischen Erscheinungen in Bewegten Körpern. EJ Brill*, 1895.

[115] Albert Einstein et al. Zur elektrodynamik bewegter körper. *Annalen der physik*, 17(10):891–921, 1905.

[116] Donald H Bilderback, Pascal Elleaume, and Edgar Weckert. Review of third and next generation synchrotron light sources. *Journal of Physics B: Atomic, molecular and optical physics*, 38(9):S773, 2005.

[117] K Balewski, W Brefeld, W Decking, H Franz, R Röhlsberger, and Edgar Weckert. Petra iii: A low emittance synchrotron radiation source. *Technical Design Report, DESY*, 35:2004, 2004.

[118] Brian WJ McNeil and Neil R Thompson. X-ray free-electron lasers. *Nature photonics*, 4(12):814–821, 2010.

[119] Philip Willmott. *An introduction to synchrotron radiation: techniques and applications.* John Wiley & Sons, 2019.

[120] Wolfgang A Caliebe, Vadim Murzin, Aleksandr Kalinko, and Marcel Görlitz. High-flux xafs-beamline p64 at petra iii. In *AIP conference proceedings*, volume 2054. AIP Publishing, 2019.

[121] Andreas Schoeps, Pavel Vagin, and Markus Tischer. Properties of the insertion devices for petra iii and its extension. In *AIP Conference Proceedings*, volume 1741. AIP Publishing, 2016.

[122] Oliver Müller. *Hard X-ray synchrotron beamline instrumentation for millisecond quick extended X-ray absorption spectroscopy/by Dipl.-Phys. Oliver Müller.* PhD thesis, Bergische Universität Wuppertal, 2016.

[123] Deutsches Elektronen-Synchrotron DESY. Beamline layout — p64 advanced xafs, 2025. Accessed: 2025-09-03.

[124] Timm Weitkamp, Paul Tafforeau, Elodie Boller, Peter Cloetens, Jean-Paul Valade, Pascal Bernard, Françoise Peyrin, Wolfgang Ludwig, Lukas Helfen, and José Baruchel. Status and evolution of the esrf beamline id19. In *AIP Conference Proceedings*, volume 1221, pages 33–38. American Institute of Physics, 2010.

[125] Michael Wulff, Friedrich Schotte, Graham Naylor, Dominique Bourgeois, Keith Moffat, and Gerard Mourou. Time-resolved structures of macromolecules at the esrf: Single-pulse laue diffraction, stroboscopic data collection and femtosecond flash photolysis. *Nuclear Instruments and Methods in Physics Research Section A: Accelerators, Spectrometers, Detectors and Associated Equipment*, 398(1):69–84, 1997.

[126] European Synchrotron Radiation Facility. Beamline id09: High time resolution, 2025. Accessed: 2025-08-22.

[127] Arthur L Schawlow and Charles H Townes. Infrared and optical masers. *Physical review*, 112(6):1940, 1958.

[128] John MJ Madey. Stimulated emission of bremsstrahlung in a periodic magnetic field. *Journal of Applied Physics*, 42(5):1906–1913, 1971.

[129] David AG Deacon, LR Elias, John MJ Madey, GJ Ramian, HA Schwettman, and Ti I Smith. First operation of a free-electron laser. *Physical Review Letters*, 38(16):892, 1977.

[130] AM Kondratenko and EL Saldin. Generating of coherent radiation by a relativistic electron beam in an ondulator. *Part. Accel.*, 10:207–216, 1980.

[131] Iulia Georgescu. The first decade of xfels. *Nature Reviews Physics*, 2(7):345–345, 2020.

[132] Thomas Tschentscher, Christian Bressler, Jan Grünert, Anders Madsen, Adrian P Mancuso, Michael Meyer, Andreas Scherz, Harald Sinn, and Ulf Zastrau. Photon beam transport and scientific instruments at the european xfel. *Applied Sciences*, 7(6):592, 2017.

[133] Hans Weise, Winfried Decking, et al. Commissioning and first lasing of the european xfel. *Proc. FEL'17*, pages 9–13, 2017.

[134] European XFEL. Overview. `https://www.xfel.eu/facility/overview/index_eng.html`, 2025. Accessed: 2025-08-22.

[135] Gianluca Geloni, E Saldin, L Samoylova, E Schneidmiller, H Sinn, Th Tschentscher, and M Yurkov. Coherence properties of the european xfel. *New Journal of Physics*, 12(3):035021, 2010.

[136] Dmitry Khakhulin, Florian Otte, Mykola Biednov, Christina Boemer, Tae-Kyu Choi, Michael Diez, Andreas Galler, Yifeng Jiang, Katharina Kubicek, Frederico Alves Lima, et al. Ultrafast x-ray photochemistry at european xfel: capabilities of the femtosecond x-ray experiments (fxe) instrument. *Applied Sciences*, 10(3):995, 2020.

[137] Andreas Galler, Wojciech Gawelda, Mykola Biednov, Christina Bomer, Alexander Britz, Sandor Brockhauser, T-K Choi, Michael Diez, Paul Frankenberger, Marcus French, et al. Scientific instrument femtosecond x-ray experiments (fxe):

instrumentation and baseline experimental capabilities. *Synchrotron Radiation*, 26(5):1432–1447, 2019.

[138] European X-Ray Free-Electron Laser Facility. Fxe instrument design, 2025. Accessed: 2025-08-22.

[139] Guido Palmer, Martin Kellert, Jinxiong Wang, Moritz Emons, Ulrike Wegner, Daniel Kane, Florent Pallas, Tomasz Jezynski, Sandhya Venkatesan, Dimitrios Rompotis, et al. Pump–probe laser system at the fxe and spb/sfx instruments of the european x-ray free-electron laser facility. *Synchrotron Radiation*, 26(2):328–332, 2019.

[140] FW Lytle, DE Sayers, and EA Stern. Extended x-ray-absorption fine-structure technique. ii. experimental practice and selected results. *Physical Review B*, 11(12):4825, 1975.

[141] Wojciech Gawelda. *Time-resolved x-ray absorption spectroscopy of transition metal complexes*. PhD thesis, EPFL, 2006.

[142] Pavan M. V. Raja and Andrew R. Barron. A practical introduction to x-ray absorption spectroscopy, 2022. Accessed: 2025-08-22.

[143] Sigray, Inc. Quantumleap series: Lab-based x-ray absorption spectroscopy systems, 2025. Accessed: 2025-08-22.

[144] Mathew Hart, C Angelsen, S Burge, J Coughlan, R Halsall, A Koch, M Kuster, T Nicholls, M Prydderch, P Seller, et al. Development of the lpd, a high dynamic range pixel detector for the european xfel. In *2012 IEEE nuclear science symposium and medical imaging conference record (NSS/MIC)*, pages 534–537. IEEE, 2012.

[145] Rayonix, LLC. Mx170-hs high speed detector, 2025. Accessed: 2025-09-27.

[146] Pierre Van Vaerenbergh, Joachim Léonardon, Michael Sztucki, Peter Boesecke, Jacques Gorini, Laurent Claustre, Franc Sever, John Morse, and Theyencheri Narayanan. An upgrade beamline for combined wide, small and ultra small-angle x-ray scattering at the esrf. In *AIP Conference Proceedings*, volume 1741, page 030034. AIP Publishing LLC, 2016.

[147] R. Paschotta. Avalanche photodiodes. RP Photonics Encyclopedia, 2019. Available online at `https://www.rp-photonics.com/avalanche_photodiodes.html`.

[148] Shunji Kishimoto. Avalanche photodiodes as fast x-ray detectors. *Synchrotron Radiation*, 5(3):275–279, 1998.

[149] FA Lima, F Otte, M Vakili, F Ardana-Lamas, M Biednov, F Dall'Antonia, P Frankenberger, W Gawelda, L Gelisio, H Han, et al. Experimental capabilities for liquid jet samples at sub-mhz rates at the fxe instrument at european xfel. *Synchrotron Radiation*, 30(6):1168–1182, 2023.

[150] Nicholas Dimakis and Grant Bunker. Apex: cross-platform analysis program for exafs. *Synchrotron Radiation*, 6(3):274–275, 1999.

[151] Matthew Newville. Ifeffit: interactive xafs analysis and feff fitting. *Synchrotron Radiation*, 8(2):322–324, 2001.

[152] M Newville. Program "autobk" version 2.61. *University of Washington*, 1995.

[153] M Newville, B Ravel, D Haskel, JJ Rehr, EA Stern, and Y(1995 Yacoby. Analysis of multiple-scattering xafs data using theoretical standards. *Physica B: Condensed Matter*, 208:154–156, 1995.

[154] DC Koningsberger, BL Mojet, GE Van Dorssen, and DE Ramaker. Xafs spectroscopy; fundamental principles and data analysis. *Topics in catalysis*, 10:143–155, 2000.

[155] European Synchrotron Radiation Facility (ESRF). Levantin / txs repository, 2025. Accessed: 2025-09-03.

[156] Tae Kyu Kim, Jae Hyuk Lee, Michael Wulff, Qingyu Kong, and Hyotcherl Ihee. Spatiotemporal kinetics in solution studied by time-resolved x-ray liquidography (solution scattering). *ChemPhysChem*, 10(12):1958–1980, 2009.

[157] Extra-FOAM Project. Extra-foam documentation, 2025. Accessed: 2025-08-22.

[158] pyFAI project. pyfai: Fast azimuthal integration using python, 2025. Accessed: 2025-08-22.

[159] pyFAI project. pyfai integrator api — azimuthal, 2025. Accessed: 2025-08-22.

[160] Asmus O Dohn, Elisa Biasin, Kristoffer Haldrup, Martin M Nielsen, Niels E Henriksen, and Klaus B Møller. On the calculation of x-ray scattering signals from pairwise radial distribution functions. *Journal of Physics B: Atomic, Molecular and Optical Physics*, 48(24):244010, 2015.

[161] AO Dohn, V Markmann, A Nimmrich, K Haldrup, KB Møller, and MM Nielsen. Eliminating finite-size effects on the calculation of x-ray scattering from molecular dynamics simulations. *The Journal of Chemical Physics*, 159(12), 2023.

[162] Fernando Mendizabal and Pekka Pyykkö. Aurophilic attraction in binuclear complexes with au (i) and au (iii). a theoretical study. *Physical Chemistry Chemical Physics*, 6(5):900–905, 2004.

[163] Linda H Doerrer. Steric and electronic effects in metallophilic double salts. *Dalton Transactions*, 39(15):3543–3553, 2010.

Declaration on Oath

I hereby declare and affirm that this doctoral dissertation is my own work and that I have not used any aids and sources other than those indicated. If electronic resources based on generative artificial intelligence (gAI) were used in the course of writing this dissertation, I confirm that my own work was the main and valueadding contribution and that complete documentation of all resources used is available in accordance with good scientific practice. I am responsible for any erroneous or distorted content, incorrect references, violations of data protection and copyright law or plagiarism that may have been generated by the gAI.

Ort, den | City, date	Unterschrift | Signature